Plants Under Pressure: A Joint Experimental-Theoretical Investigation of the Plant Response to Local Stimuli

Jordan Mark Hembrow

Submitted by Jordan Mark Hembrow to the University of Exeter as a thesis for the degree of Doctor of Philosophy in Physics, March 31, 2023.

Date: ..... Signed: .....

Jordan Mark Hembrow

Abstract

1st Supervisor: Dr. David Richards 2nd Supervisor: Dr. Mike Deeks

Rising temperatures and growing populations are putting increased pressure on food sources, with pathogens moving polewards in search of more favourable conditions. Stopping crop losses due to disease would provide enough additional food to solve world hunger, with spare left over. My PhD has been centred on discovering more about how plants are able to defend themselves to new or unknown potential pathogens through the use of the model organism, *Arabidopsis thaliana*. I have helped to develop a novel method of stimulating the basal immune response in order to probe different components of this system.

PEN3, a key defence protein that is transported to the site of infection, was observed over the initial 20 minutes of an immune response and its accumulation was quantified. PEN3 transport requires the actin cytoskeleton, which remodels within 30s of artificial peg contact, therefore I developed an image analysis algorithm to segment and quantify various aspects of the cytoskeletal network. This algorithm detected significant differences in the network of loss-of-function mutants of *arp2-1* and *formin4/7/8* compared to the wild-type, yet the PEN3 distributions were functionally identical. These findings, alongside simulations of PEN3 accumulation with various delivery zone sizes led to the hypothesis of at least one upstream signalling molecule designating PEN3 secretion into the membrane.

The novel assay, network extraction tool and PEN3 simulations are discussed in detail, including their limitations and potential improvements as well as other systems they could be applied to.

Contents

List of Figures

List of Tables

Declaration

This thesis contains work published or pending publication as papers. Chapters 4 and 5 are from a paper currently under review. Material from this paper is also found in 1.6.

Acknowledgements

I wish to thank my supervisors, David and Mike; you have been incredibly supportive and helpful, from the application and interview processes, to teaching me both wet lab and MATLAB skills, to writing papers and rewriting papers and rewriting papers again, all the way to thesis submission. Your insight has been invaluable, and your support, especially through the challenging pandemic, has really enabled me to get the best out of myself and the PhD. Thank you so much!

Thank you to my partner Lucy, whose incredible work ethic has guilt tripped me into working harder and achieving more than I thought I previously could. Thank you for keeping me both fairly sane and well fed during lockdown, and for always patiently listening to me rant and ramble about experiments or simulations which were unsuccessful or problematic. My gift to you is that you do not have to read my thesis beyond this paragraph, a gratitude I hope is reciprocated when you submit in a couple years!

I cannot forget to mention my recent desk-mate Alaina, who has been a great support and welcome distraction during the paper and thesis writing process. Our (fairly frequent) tea breaks have been very beneficial to my well-being and have ensured that the gaps in between are filled with copious amounts of work and writing. Thanks for all the tea (and tea!).

Of course I could not end my acknowledgements without thanking my parents, who always ask how the PhD is going and politely try to follow along as I describe a set of incredibly niche problems I am currently stumped by. Your support has been beyond wonderful and unwavering, and for as long as I can remember you have been incredibly loving and helpful. I cannot thank you enough for enabling me get to where I am today.

Chapter 1

Introduction

There are an estimated 300,000-400,000 species of plants on Earth, with more than 7 million animal species. The existence of such a vast and wide variety of animals would not be possible without these plant species. The ability of plants to harness energy from the sun for their food production and growth, which coincidentally helped tame the surface of the Earth to make it hospitable (Alcott et al. 2019), provided us a simple, safe and nutritious form of sustenance. The importance of crops for human survival has been long-standing, as shown by the evidence of agriculture from at least 10,000 years ago (Tauger 2010), if not longer, likely as a result of a shift in the global climate into environmental stability, like we enjoy today. With such a reliance on these crops, ensuring they are able to grow sufficiently and not be toxic for consumption has also been a concern since the middle ages (Lieber 1982).

While it had been long known that a toxic fungus was responsible for causing ergotism (a disease caused by ingesting grains infected by the fungus *Claviceps purpurea*) throughout Europe, evidence of pathogenicity of micro-organisms was not found until the nineteenth century (Lieber 1982), enabling the development of the plant pathology field. By the end of the century the cause of wheat bunt—a fungus called *Tilletia tritici*—and tobacco etch virus had been discovered. In the 222 years that have passed since then, thousands of plant pathogens have been discovered and categorised, with fungal and oomycete pathogens being the most prevalent pests. Evolution of disease and the

rapid acceleration of climate change has made food security a prominent global concern.

1.1 Plants and Their Importance

Solar radiation is a free and abundant resource, accessible from most regions of the planet surface for a significant portion of the day. While humans are only just beginning to tap into it as a reliable energy source, plants have been using it for hundreds of millions of years to great effect. Reliance on the sun allows plants to be (mostly) immobile which is a great benefit as locomotion is an energy intensive task. This was made possible through the development of the chloroplast organelle, which originally came from a photosynthetic cyanobacterium. Tracheophytes developed vascular tissue, with specialised xylem and phloem established in the flowering plants, which harness the capillary effect to passively uptake water from the soil and roots to the leaf canopy. Leaf cells have small, sometimes controllable holes (stomata) to enable gaseous exchange for chloroplast reactions, and transpiration in these leaves generates a pressure gradient in the xylem, drawing up more water (Morris 2018). Through the use of solar energy, water and carbon dioxide are converted to sugar and oxygen via a complex series of biochemical reactions. These chloroplasts also have an additional role in plant innate immunity, generating reactive oxygen species (ROS) for both programmed cell death and systemic acquired resistance (Littlejohn et al. 2021; Kachroo et al. 2021).

Perhaps the most obvious role of plants, and particularly crops, in human lives is as a source of food. Approximately 88% of the worlds caloric intake is from plant consumption, as well as around 80% of our total protein intake (Muhammad and Amusa 2005). While both of these values tend to be lower in affluent countries due to increased meat consumption, the reliance on crops is even more substantial. From 1990-2007 the consumption of meat per capita increased by 25%, which coupled with the increase in population resulted in a 60% rise in meat consumption over 17 years (Henchion et al. 2014). The inefficiency of an additional step in the food chain requires a significant increase in the mass of crop needed. In Europe, around 3.1 kg of dry feed is needed for 1 kg of poultry meat, whereas the figure for pork is 6.2 kg and non-dairy cattle require 24 kg (Alcamo 1994; Ramírez et al. 2006). Another major issue with this is that the important protein sources in ani-

mal feed are soybean meal, which competes with its use in food production, and fishmeal which has limitations from marine over-exploitation (Chia et al. 2019; Masuda and Goldsmith 2009; Tacon and Metian 2008). With projections of population growth reaching over 9 billion by 2050, the demand for global food production is expected to increase by 70-85% over a 35 year period (Ray et al. 2013; Dhankher and Foyer 2018).

A more recent development in crop use is for biomass and biofuels as a result of pressure to reduce carbon emissions and our reliance on fossil fuels. Biomass currently provides approximately 14% of global energy needs (Koçar and Civaş 2013), with the most common biofuels being bioethanol and biodiesel. Both of these are first-generation biofuels which can be used to power vehicles in their purest form, but usually are added as a supplement to existing petroleum and diesel fuels. The levels of the bioethanol component are increasing, now 10% both in the UK and in Formula 1, with up to 25% for newer vehicles in Brazil (Aggarwal et al. 2022). While some of the biofuel can be made with the waste from food crops, primarily they are produced using fermentation of sugar and starch crops which would otherwise be used for food production (Koçar and Civaş 2013). This further increases land use pressure, raises food costs and can add further dependencies on food, especially for those that do not have enough (Boddiger 2007).

Plants play a huge role in maintaining the climate, and the most frequently referenced benefit is their role in being a carbon sink. While plants do absorb CO_2 and produce O_2, they may sequester carbon up to 50 times less efficiently than microalgae (Bhola et al. 2014; Iglina et al. 2022), therefore in terms of farming it would likely be more beneficial using microalgae for a given area. Another key benefit of plants is their effect on humidity, water cycle and temperature control. Evapotranspiration of water from the stomata on a leaf surface increases the relative humidity and decreases the temperature, which reduces the risk of fire and promotes cycling of water through precipitation. By drawing water out from the ground and releasing some of it into the atmosphere, the plants can increase the frequency of rain (such as in tropical forests) and stop the moisture being lost (Vorosmarty and Sahagian 2000). Plant roots provide an anchor for soil to help prevent erosion and degradation of the land as well as provide habitats for a host of animals and microorganisms alike.

1.2 Threats to Food Security

Since 2019, many countries have officially declared a climate emergency, with climate change and global warming posing a threat to current lifestyles. These changes in the climate affect soil fertility, microbial activity, plant growth and carbon sequestration which has resulted in numerous ramifications for global food security and has already had a significant impact on worldwide agricultural production (Dhankher and Foyer 2018). These issues are exacerbated by the current low diversity and high intensity farming methods which puts global food security at increasing risk. One of the most concerning changes is centred around the weather and seasonality (Evangelista et al. 2013). Climate change is likely to result in a shortened growing period which would be problematic for fruit and vegetable produce (Malhotra 2017) while also increasing both the frequency and amplitude of extreme weather events such as droughts and floods. This impact will vary between regions; those with drier climates, such as Ethiopia, will be susceptible to reduced yields as agriculture is highly reliant on the volume and seasonal occurrence of rainfall (Evangelista et al. 2013). The increased risk of flooding is bad for crop yields (Malhotra 2017) and unseasonal rains can cause fruits to rot or nuts to blacken, while weather is the second most important factor of pathogen spread and infection of new diseases (Bebber et al. 2013). Extreme weather events are likely to increase crop disease and the toll they take from pathogens, resulting in lower yields and an increased risk of famine (Long et al. 2015; Dhankher and Foyer 2018).

Increased CO_2 levels and rising temperatures go hand-in-hand but mostly have opposing effects for plant growth, although it also varies between species. Drought and heat stress often occur simultaneously and their combined effect on decreasing yield is greater than the sum of their parts (Zandalinas et al. 2018). While vegetative growth of many crop species is fairly tolerant of raised temperatures, reproductive growth is not. Even the most resistant of crops show a decline beyond 26°C while key crops such as rice were effected at lower temperatures (Boote et al. 2005). These grains had improved yields at raised CO_2 levels, however, so the effects of temperature are partially mitigated, although under these conditions some crop species show reduced nutritional value (Anderson et al. 2020). Wheat and barley tend to be less sensitive and more resistant to climate change

(Ashofteh et al. 2015), although wheat is still expected to see a 4-6% drop in yield for every degree of global warming (Asseng et al. 2015), and maize is likely to see a 10-30% drop in yield depending on the emissions scenario (Meza et al. 2008). Cassava, an important crop in drier regions, and sweet potato are tolerant to drought conditions, but still see a reduced tuber yield and starch content, as tuber crops tend to struggle with increased temperatures (Malhotra 2017). Horticultural crops with a C3 photosynthetic metabolism benefit from the increased CO_2 levels, and higher temperatures can increase the rate of fruit growth, but also run the risk of increased transpiration which can cause dehydration injuries when combined with a lower relative humidity. Agriculture at high altitudes is expected to see an increase in yield at elevated temperatures, whereas tropical regions will see a decline for even a small increase in temperature. Poorer countries, which tend to be at lower latitudes, are already close to heat thresholds and therefore any increase in temperature could be catastrophic (Malhotra 2017; Evangelista et al. 2013). Under elevated CO_2 levels, alterations to current crop management methods are needed to optimise any available yield gains (Anderson et al. 2020) while raised temperatures will need to be managed depending on the region.

Disease has plagued crops and significantly decreased yields for as long as agriculture has existed, with 10-20% of crops being lost to pathogens every year and similar numbers post harvest (Bebber et al. 2013; Bebber and Gurr 2015). Severe pathogen outbreaks can lead to entire crops being lost: the Irish potato famine in the 1840s was caused by the oomycete *Phytophthora infestans*, the 1943 great Bengal famine from the fungus *Helminthosporium oryzae*, and the African Cassava famine in the 1920s caused by the Cassava mosaic virus. Fungal and oomycete pathogens are the leading cause of crop disease, with crop losses that could feed over 8% of today's population (Fisher et al. 2012). Evolution of existing and emerging pathogens will continue to be a threat, but climate change is exacerbating the issue. Since 1960, pathogens have been shifting polewards at an average speed of 2.7 ± 0.8 km yr^{-1}, nearly identical to predictions from warming (Bebber et al. 2013). There is, however, significant variation between taxonomic groups, with some pathogens reaching 8 km yr^{-1}, resulting in crops being introduced to unusual pathogens, increasing the risk of disease and the possibility of more catastrophic events. Current agricultural practices provide little in the way of security from mutations and adaptations

of pathogens, and tends to favour the emergence of aggression pathogen variants which may overcome plants defences, fungicides, or both.

Land and water are finite resources, yet agriculture occupies around 40% of the land surface while using 70% of the total available freshwater resources (Springmann et al. 2018), therefore the solution to feeding an increasing population will rely on improved efficiency rather than just increasing land use. The impact of agriculture on the environment further extends this idea, as it is the biggest driver of biodiversity loss, through fragmentation and habitat loss, as well as being the key driver of land use and land use change (Willett et al. 2019). As a significant amount of carbon is sequestered in soil, the process of converting land for agriculture is incredibly impactful on the environment (Ostle et al. 2009), which alongside the downstream effects of deforestation such as regional drying, increased temperatures, habitat loss and soil degradation, agriculture is responsible for around a quarter of global greenhouse gas emissions (Springmann et al. 2018), resulting in food production being identified as the largest cause of environmental change on a global scale (Sandberg 2021). As the CO_2 levels in the atmosphere become more critical, alongside rising temperatures, the available land and freshwater are likely to decrease (Kundzewicz et al. 2008), further exacerbating the issue of increasing crop production. One key to the solution of mitigating anthropogenic climate change is through broad dietary shifts, reducing inefficiencies in the food chain (Robinson et al. 2019). Pulse crops provide protein and micronutrients in an environmentally sustainable way and will likely become a more significant component of peoples diets.

Between 1962 and 2012, the world population doubled and cereal crop yield tripled, while agricultural land use increased by only 30% (Pingali and Broca 2014), meaning average yields per hectare increased over 130%. Large investments in crop research and infrastructure enabled this *green revolution*, through both high yield varieties of crops as well as a reduction in the time for crop maturity to increase cropping intensity. This resulted in reduced poverty and saved significant amounts of land from being converted to agriculture (Pingali 2012). While major crops in the developed world, such as wheat, rice and maize, were the main focus of genetic research, the knowledge gained was adaptable to those in developing countries (Spielman and Pandya-Lorch 2010; Dethier and Effen-

berger 2012). From 1960-2000, a 208% rise in wheat yields was seen in developing countries, as well as 78% for potatoes, 36% for cassava, 157% for maize and 109% for rice (FAO 2004). Projections of population growth from 2015-2050 suggest a required 200 trillion more calories need to be grown over the 35 year period (Bebber and Gurr 2015), which combined with the increasing limitations due to abiotic stresses such as water crises and rising energy costs, has resulted in the call for a new green revolution (Dhankher and Foyer 2018; Pingali 2012). The use of technology has resulted in yield increases of over 11 times in horticulture crops since 1950 (Hay and Probert 2013), therefore technology will be required for more efficient deployment of limited resources and to improve agricultural gains further (Pingali 2012). The blue wavelengths from LED lighting is able to improve the nutritional value of certain crops (Kopsell et al. 2015), which may reduce the amount of crop required to be grown. Significant improvements in agricultural efficiency will be needed to avoid malnutrition, famine and starvation in the future.

Some of the conventional methods of boosting agriculture have proven problematic; however, with fertiliser use resulting in surface water pollution and ocean dead zones in some regions (Springmann et al. 2018). The use of pesticides has not been without issue either, and over the time of their deployment a range of pathogens have developed resistances, with certain compounds overcome in just two years (Lucas et al. 2015). Many of these chemicals are environmentally stable, leading to bio-accumulation and the possibility of unwanted toxicity (Fenik et al. 2011). Their continued use may result in pesticide residues being present in the air, water or in food (Mostafalou and Abdollahi 2013), whilst only around 1% of pesticides actually reach their intended target (Bernardes et al. 2015). As the side effects of pesticide use may only be seen in the long term, such as genetic disorders or reduced life span (Poletta et al. 2009), their use has to be carefully managed and monitored. This, coupled with their significant research and design cost as well as the rapid evolution of pests somewhat limits the efficacy of pesticides.

Another method of improving food security has been through genetically modified (GM) crops. This isn't always feasible, or even beneficial, and the EU has a near blanket ban on the growth of GM crops (Rasheed et al. 2022). The main trait changes that have been targeted by GM are herbicide tolerance and insect resistance (Rommens 2010), reduc-

ing the reliance on pesticides. More complex traits; however, have proven much harder to achieve, with attempts resulting in either no benefits or even unattractive side effects (Chen and Lin 2013). Even if advances are made in the field, each specific modification has to be thoroughly tested before being commercialised. The vast arrays of testing attempt to assess the ecological impacts of each GM crop before use to avoid unwanted side effects (Lu et al. 2010), which is not only a lengthy process, but is cost prohibitive on top of the already significant R&D costs. It is difficult to determine the effect of long-term cultivation of these resistant strains, but it is possible that it will accelerate the evolution and adaptation of pests and pathogens (Chen and Lin 2013), similar to the issues seen with anti-microbial resistance. This phenomenon occurred in Uganda with the UG-99 wheat stem rust infestation (Pingali 2012) which highlights the requirement of constant GM development to remain one step ahead of the pathogens and avoid additional epidemics (Conway 2012).

Outside of resistance genes, plants have a basal resistance to non-specific pathogens which allows them to fend off new threats. Specific (host) resistance may be overcome in 2-3 years for some crops (Dean et al. 2012) so reliance on it is not ideal, therefore leveraging non-host resistance could prove more beneficial. Allowing plants to defend themselves can boost yields both pre- and post-harvest, as well as reduce pathogen transmission. To probe this system, the mechanics of infection needed to be studied, and with the main threat from fungal and oomycete pathogens (Bebber and Gurr 2015), these have often been a priority. *Magnaporthe oryzae* causes rice blast, the leading cause of rice crop losses, of which 50% of the population relies upon for their primary calorie intake (Dean et al. 2012). It can also form a complex which may cause disease on a range of grasses and crops such as barley and wheat. Its destructive nature and societal importance has led it to become one of the model organisms for crop-fungal interactions. Another pathogen that infects wheat and barley, two of the most relied upon crops worldwide, is *Blumeria graminis*, which has become a model for other mildew and biotrophic pathogens (Dean et al. 2012). Alongside pathogen models, *Arabidopsis thaliana* has been used as a model plant due to its small size and rapid growth alongside its sizeable feature set for its small genome. These have been used in tandem to improve our knowledge on plant-fungal interactions and will continue to be used in the future.

A better understanding of plant basal resistance will be critical in the changing landscape due to climate change and increasing population demands. Not only are pathogens moving polewards, increasing reliance on non-host resistance, but wild species are too (Parmesan and Yohe 2003; Burrows et al. 2011; Chen et al. 2011), suggesting agriculture should consider doing the same. As yields and farming density rise alongside increased cropping frequency, the threat of disease grows. With crops becoming a more and more critical resource, the chance of catastrophe through disease increases. Around 800 million people are hungry (Gillespie and Bold 2017; Research Institute (IFPRI) 2016) and 2 billion people suffer from undernutrition resulting in 3.4 million deaths globally (Ng et al. 2014). This is expected to increase, and disease outbreaks could cause severe loss-of-life on top of these already significant numbers. The issue of food security is therefore huge, to which there is no 'silver bullet': a multi-faceted problem requires a whole host of solutions.

With the push to grow more food, even a static percentage loss means even more wasted crop. Between 25-30% of globally produced food is lost or wasted, an increase of 44% from 1961 to 2011 (Anderson et al. 2020). Even a slight reduction in losses will significantly reduce the number of those that go hungry and the deaths that result. With current projections of crop yield gains set to fall short of the food demands (Ray et al. 2013), the fight against disease becomes more critical every day and plant non-host resistance has a big role to play.

1.3 Introduction to Plant Immunity

Most phytopathogenic fungi have to penetrate plant cell walls at some point in their life cycle: they can either chose to break through the cell wall of epidermal cells, or they can determine the cell topology and infiltrate between cells with the aim of first entering through a stomata, before attempting to penetrate into mesophyll cells. As both methods require penetrating the cell wall, plant cells have devised methods to protect against this. The cell wall is a dense, strong structure, therefore a significant amount of force is required to break through it. Phytopathogens create a specialised structure known as an appressorium in order to achieve this. To aid in their penetration attempt, some pathogens will secrete cell wall degrading enzymes, weakening it before trying to break through, while

others generate vast amounts of turgor pressure—in excess of 8MPa (Howard et al. 1991)—in these appressoria. In order to apply these forces, the pathogen has to attach itself to the surface of the cell, or neighbouring cells, and in the case of powdery mildews, they generate a primary germ tube to determine the suitability of the surface for attachment and penetration (Yamaoka et al. 2006). This stage is critical to the success of the pathogen, and renders different tissues or even species nearly immune to some different pathogens (Tucker and Talbot 2001). Depending on the phytopathogen, once inside the cell it will either begin to colonise while the cell is still living, forming a biotrophic relationship, or it will kill the cell and digest its contents as a necrotroph.

1.3.1 Zig-Zag Model

The two-branched innate immune system can be partially described by the zig-zag model (Jones and Dangl 2006), named for the back-and-forth battle between plant and pathogen, outlined in Fig. 1.1. This model is based upon phenotypic disease outcomes and therefore is lacking in describing some of the molecular mechanisms, but is a solid starting point for understanding how both the plants and pathogens respond. The first branch and the initial response of plant cells is PAMP triggered immunity (PTI), which is always non-specific and can be successful in its own right (Méndez and Romero 2017). Both the chemical signature of the cell wall degrading enzymes, or their products, known as Pathogen-Associated-Molecular-Patterns (PAMPs) and the physical stimulus of an appressorium can begin to trigger this stage of the plant immune response. The PAMPs, which are often very similar for a range of different phytopathogens, are detected by transmembrane pattern recognition receptors (PRRs) (Nishimura and Dangl 2010; Meisrimler et al. 2021), which triggers reorganisation and reinforcement of the actin cytoskeleton locally (Ma et al. 2022), movement of organelles and subcellular compartments, and accumulation of the cytosol below the site of infection (Schmidt and Panstruga 2007), which is aided by the filamentous actin nests. Plant cells are large and the volume of vacuole makes the cytoplasm very confined, therefore efficient transport and delivery of key proteins requires significant rearrangements of the cytoskeleton and organelles.

Coordinating these changes requires multiple signalling pathways, which also helps

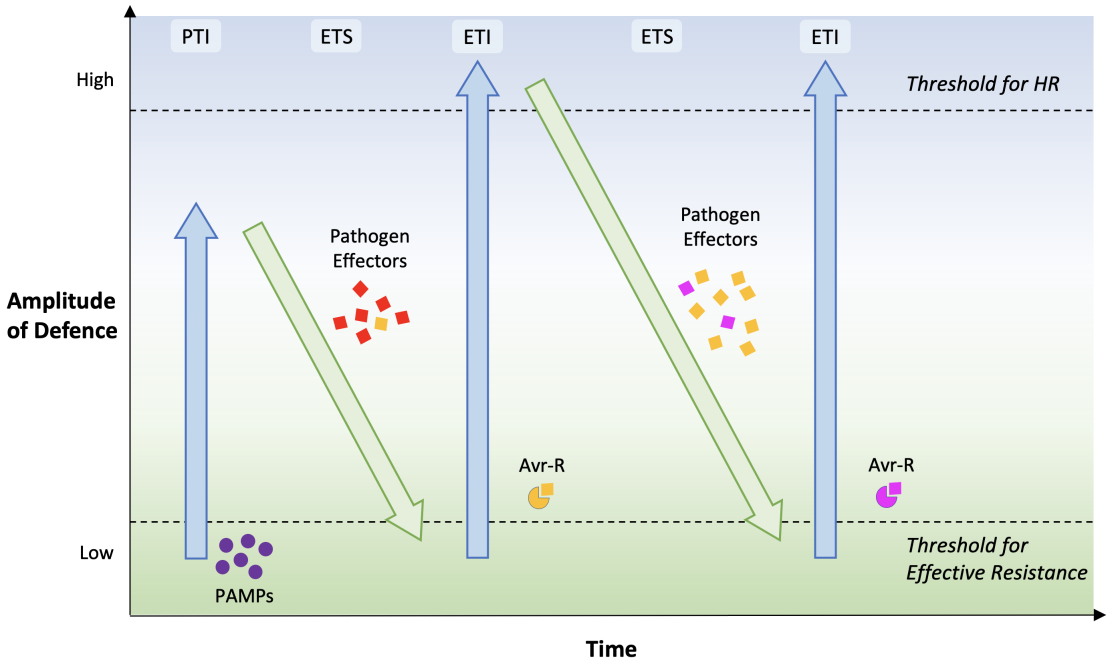

Figure 1.1: Zig-Zag Model: The primary step is recognition of pathogen associated molecular patterns (PAMPS) via pattern-recognition receptors to initiate pattern-triggered immunity (PTI). For pathogens that are successful in proceeding onwards, they produce effectors to suppress PTI and cause effector-triggered susceptibility (ETS). One of the pathogen effectors may be recognised by the NB-LRR proteins of the plant, activating effector-triggered immunity (ETI). ETI is an exaggerated version of PTI that may lead to the hypersensitive response (HR) and programmed cell death. In phase 3, one effector or suppressor is recognized directly or indirectly by an NB-LRR protein, activating effector-triggered immunity (ETI), an amplified version of PTI that often passes a threshold for induction of hypersensitive response (HR) and programmed cell death (PCD). Over time, the pathogen may develop new effectors to trigger an addition ETS phase, and the plant will have to evolve and select for a new NB-LRR protein to detect the effector in order to reach another ETI stage. The magnitude of resistance to phytopathogens is proportional to PTI – ETS + ETI. Many of the respective stages overlap and occur simultaneously in reality as the two ssytems compete for dominance. Figure adapted from Jones and Dangl 2006

to ensure that the response is justified. PTI triggers the activation of both calcium dependant protein kinases and receptor-like cytoplasmic kinases, such as the ten MAP4 kinases in *A. thaliana* (Zhang et al. 2018). One of the MAP4 kinases is the Serine/Threonin-protein kinase SIK1 responsible for efficient deployment of Reactive Oxygen Species (ROS) bursts. SIK1 stabilises the receptor-like cytoplasmic kinase BIK1 which is responsible for activating RBOHD (Respiritory Burst Oxidase homolog protein D). This produces an extracellular ROS burst as an immune response, which if compromised can reduce downstream immune responses (Wang et al. 2014; Kadota et al. 2015).

Phytopathogens are also able to detect changes in the chemical signatures of their environment and the plant cell surface. These pathogens may secrete effector proteins to either suppress the effects of PTI, by blocking signalling pathways or counteracting some

of the effects, or to manipulate non-immunity pathways to aid in colonisation (Meisrimler et al. 2021), such as enabling nutrition dispersal for the pathogen. This process increases the susceptibility of the plant and it is therefore called effector triggered susceptibility (ETS) (Jones and Dangl 2006).

Successfully overcoming PTI can trigger specific dominant resistance (R) genes, which detect the pathogen effectors. A large proportion of R genes encode a protein with nucleotide binding (NB) and leucine-rich repeat (LRR) domains (Dangl and Jones 2001) which detect these effectors and trigger a highly specific response, known as a host response. A range of responses are generated through these effectors binding to the NB-LRR proteins, of which there are 125 in the *A. thaliana* Col-0 genome, and this process is known as effector triggered immunity (ETI) (Nishimura and Dangl 2010; Jones and Dangl 2006). ETI is a extended version of PTI, of which co-activation results in a mutual potentiation of the individual effects (Ngou et al. 2021). This can lead to enhanced ROS bursts generated through PTI, or even the host cell activating its hypersensitive response (HR) leading to cell death (Dodds and Rathjen 2010). The activation of these NB-LRR proteins is highly coordinated, with signalling through the salicylic acid pathway, as well as jasmonic acid and ethylene (Glazebrook 2005). The balance between these signalling pathways is chosen to identify the nature of the pathogen, be it biotrophic or necrotrophic and to therefore ensure the response is consistent with denying the needs of the pathogen. If the cell does not enter the HR, the pathogen may secrete new effectors, through mechanisms such as gene-transfer, causing the cell to enter ETS again. The back-and-forth between ETS and ETI can continue multiple times, in a zig-zag manner. Even success here will likely induce HR and cell death which is bad for crop yield and does not always completely deter the pathogen. There are many additional layers to PTI, and the non-specificity is important in a changing landscape.

The zig-zag model was developed mainly through data from *Arabidopsis thaliana*. In the same way that the fruit fly became a model organism for genomic work, *Arabidopsis thaliana* has been used as a model organism in plant and crop biology research, due to its simplicity and its quick growth, to an even greater extent (Woodward and Bartel 2018).

1.4 The Use of Model Organisms

A. thaliana is a seed plant that has most of the typical features you would expect (*i.e.* stems, apical meristems, stomata which open/close for gas exchange between the atmosphere and the leaf, roots with hairs, vascular tissue and pollen), while being small, quick growing and thriving indoors. In the same way that crop density and yield are important to farmers, the same is true in research. Space is limited and growing large plants which take a lot of time and energy is expensive. The smaller the time taken for these plants to grow to maturity and produce offspring is important, as many genetic crossings require additional generations to be grown to ensure homozygous genes. Crops which are happy with small fluorescent bulbs or LEDs as a source of light, and can grow in media other than soil can massively improve the efficiency of research by increasing throughput and overhead. The benefit of such a flexible crop is that many environmental factors can be controlled. The use of LEDs can enable research into the effect of different and very specific wavelengths of incident light in the growth and development of the plants. This flexibility and hardiness allows them to grown in growth chambers where the length of the day, light intensity, water availability, atmospheric carbon dioxide content and humidity can all be closely controlled and monitored. Many *A. thaliana* seeds can be grown in a petri dish, allowing quick and efficient testing of drugs, growth media and nutrient content. This can also be used to check the viability of certain lines without requiring significant wait times.

A. thaliana is not only small in physical size, but it also has a comparatively small genome (Provart et al. 2016; Cheng et al. 2017), while containing genes showing equivalence to many of the features of key crops we are interested in. Despite noth being diploid species, maize (*Zea mays*) and barley (*Hordeum vulgare*) still have genomes at least ten times larger in size relative to *A. thaliana*, while common wheat (*Triticum aestivum*) is hexaploid with an incredibly complex genome. The benefits of the small *A. thaliana* genome is that these genes can easily be screened, tested and altered, often just by looking at the phenotypic outcomes and this can be translated to work in other species. This also meant that the full genome of *A. thaliana* was available much earlier than other species (Nishimura and Dangl 2010), increasing its popularity and therefore knowledge surrounding the species,

enabling hypothesis testing at a greater rate. On the other hand; however, the lack of plant mass can also be a detriment, where proteins, DNA or metabolites are to be extracted (Woodward and Bartel 2018; Weckwerth 2003). Any time gained in using a smaller organism may be lost when having to use more plants and cells for extraction, especially as any of these can be time consuming and technically challenging tasks.

One difficulty of studying a biological system is the vast array of interactions that are taking place. Science is often reductionist in approach, and therefore the system being tested is reduced to the most simple version possible, with one variable carefully adjusted while the rest are controlled. The issue with taking out various components of a biological system is that other systems may either be upregulated or downregulated to compensate (Van Regenmortel 2004) or vary due to their developmental stage (Benfey and Mitchell-Olds 2008). While this can be helpful in of itself, it makes testing hypotheses *in vivo* more difficult (Van Norman and Benfey 2009). This is where a fundamentally more simplistic system is beneficial. Anything that cannot be controlled has to be accounted for, and this reduces the power of any scientific experiment, therefore smaller, more simple organisms reduce the number of variables that have to be controlled or measured, while also being quicker to grow and test, increasing throughput. This significantly increases the power of an experiment and therefore enables more detailed testing and analysis to take place.

The use of model organisms isn't perfect; however, and any work done needs to be translated and tested in the system you are eventually concerned with. Work also needs to be done in the first place to determine which model, if any, is suitable. Many land plants require arbuscular mycorrhizal fungi for nutrient and water absorption, yet *A. thaliana* does not associate with these fungi at all (Woodward and Bartel 2018). While this allows it to thrive in aseptic conditions, some of the strigolactone chemical signals for promotion of this symbiotic relationship are missing, therefore *A. thaliana* may be unsuitable for this work. This initial overhead, which may yield nothing of value, can be a deterrent, but as complexity of research increases, this overhead becomes less significant. The simplicity of a model aids in testing a plethora of hypotheses in a short time, indicating what needs to be investigated in greater detail on the final organism, while also aiding in refining or developing new methods. Every process takes time, and more importantly has a cost -

using a model is a way of improving efficiency, aiding in reducing both of these limitations. While the findings may not be indicative of any equivalent results in the organism of interest, more often than not it provides key insight and knowledge which aids in the search (Somerville 2001; Provart et al. 2016).

The small size of *A. thaliana* is perfect for microscopy, and the quick growth time is perfect for development of new techniques, both in terms of data collection and analysis. As *A. thaliana* is frequently used as a model organism and its seeds take up a very small volume, many seed banks with various genetic lines are available throughout the world, such as the Eurasian Arabidopsis Stock Centre for European and Asian distribution or the Arabidopsis Biological Resource Centre for America. This reduces the time taken for any experiments to get up and running, as fewer transformations are required in-house, and can also reduce the cost, both in terms of training and qualifications and well as reducing the number of reagents and equipment needing to be bought and stored. This also enables testing and validation through third parties to be as consistent as possible, helping to ensure reproducability in any discoveries. This is vital in any model, as translating methods and assays to more complex systems can prove difficult. Simple reproducability in the model ensures that any issues found in the next step are not due to issues in the model system, and therefore any differences found can be confidently stated as an outcome of additional interference and complexity, as opposed to a mistake. While gene editing is much more simple and significantly cheaper than it used to be, especially since the discovery and deployment of the CRISPR/Cas9 system (Li et al. 2013), it is still non-trivial and requires validation before any large-scale experimentation can begin.

A. thaliana has already proven its worth as a model system of plants and crops (Martin et al. 2002; Singh et al. 2015; Wijk and Kessler 2017; Provart et al. 2016; Somerville 2001; Llave et al. 2002; Park et al. 2002; Reinhart et al. 2002) and therefore has been chosen for the research here. Many of the pathways of photorespiration, a mechanism to reclaim some inefficiencies of photosynthesis in hot, dry conditions, were found first in *A. thaliana* (Woodward and Bartel 2018). It was also one of the key organisms used in the discovery of the MADS-box genes, their roles and interactions in floral development (Woodward and Bartel 2018). The first plant microRNAs were discovered in *A. thaliana*

and many breakthroughs in signalling pathways, such as the blue photoreceptor required for phototropism and receptors for auxin, the plant growth hormone, also came from this organism (Woodward and Bartel 2018). The ease of testing in *A. thaliana* enables the use of reverse genetics in other systems, speeding up the process of locating genes relating to a particular function. In-depth knowledge of the genome enables genes and functions to be translated to other species so their benefits can be shared. An *A. thaliana* transcription factor, MYB12, which is responsible for producing a chemical synonymous with markers for cardiovascular health was successfully expressed in tomatoes, significantly enough to change their colour (Woodward and Bartel 2018).

Research into resistance genes in *A. thaliana* may not be transferable to other organisms depending on the species context or due to the differences between monocots and dicots, therefore it is only really applicable on a case-by-case bases. Research into the basal resistance of *A. thaliana*; however, could provide useful insight into the mechanisms plant cells and tissues employ. These systems are fairly fundamental and therefore are likely to have similarities between species, at least in part, therefore the choice of a model organism is appropriate.

1.5 Focal Immune Response

Non-host resistance is defined as an entire plant species being resistant to a pathogen (fungi, oomycetes, bacteria or viruses) but the same pathogen has the ability to infect other plant species (Bent and Mackey 2007; Fan and Doerner 2012; Bellincampi et al. 2014; Méndez and Romero 2017). A diverse range of proteins are recruited and transported to the site of infection during the non-host response, in an effort to mitigate the effects of the phytopathogen and to reinforce the cell wall and surrounding structures against the forces of the appressorium (this is true in a host response, too, albeit often far less successfully). The end goal is to produce the papilla, a cell wall apposition (CWA) localised to the site of attempted penetration which will arrest the advances of an appressorium. The CWA is a complex structure, consisting of callose, proteins, some inorganic compounds and at times, reactive oxygen species. This extracellular release of proteins, secondary metabolites and cell wall materials requires trafficking of secretory vesicles to the plasma mem-

brane before secretion via exocytosis can be performed (Yun et al. 2022). The remodelling of the actin cytoskeleton under the infection site is important for cytoplasm accumulation and aids in the transport of vesicles and organelles along the network. This process takes less than a minute for visible changes (Branco et al. 2017), and inhibiting this process significantly decreases immune competency (Li and Day 2019; Henty-Ridilla et al. 2013) therefore it has become a frequent target for pathogen effectors (Yun et al. 2022). Cytoskeletal remodelling also enables the transport of FORMIN4 to the infection site, which is found to be upregulated during penetration attempts (Sassmann et al. 2018), where they are added to the membrane in a punctate pattern. These FORMIN4 nano-domains are responsible for further development of the filamentous actin network under the infection site, and remain there as a marker to signify the infection.

Penetration defence genes are activated in PTI, such as PEN1-PEN4, which are all linked to the efficacy of the non-host response and have a range of roles (Johansson et al. 2014). PEN1 is a plant syntaxin, a membrane-integrated protein that forms part of the soluble N-ethylmaleimide sensitive factor attachment protein receptor (SNARE) complex which is instrumental in vesicle exocytosis (Takemoto et al. 2006). It is transported in vesicles to the infection site, where it is responsible for timely deposition of key CWA components such as callose into the into the apoplast. PEN1 undergoes continual shuttling between the trans-golgi network (TGN) and the plasma membrane; it is suggested to work at the TGN, mediating the fast recycling of papilla material (Rubiato et al. 2022). The loss of PEN1 function in *A. thaliana* results in almost 90% of barley powdery mildew *Blumeria graminis* f. sp. *hordei* (Bgh) successfully penetrating the cell wall (Collins et al. 2003). While PEN2 is associated with the periphery of peroxisomes (Lipka et al. 2005), this remains to be a subpool of the protein and focal accumulation around the infection site is transient. The main PEN2 population is localised to the membrane of mitochondria, of which a sub-population have been shown to be fixed in proximity to the focal response site (Fuchs et al. 2016). These mitochondria show redox imbalances and it is hypothesised that these imbalances may lead to signalling changes important to the immune response. PEN4 acts with PEN2 in the synthesis of the phytochelatin synthase peptide, which plays a key role in heavy metal tolerance (Hématy et al. 2020) and PEN4 also aids in synthesis of indole glucosinolates, with loss-of-function mutants showing reduced immune com-

petency. PEN3 encodes PDR8, an ATP binding cassette (ABC) transporter protein (Stein 2006) which is distributed evenly across the plasma membrane during normal cell operation. Its role is to transport toxins from the cell to the apoplast (Matern et al. 2019), such as indole glucosinolates, and accumulation of these toxins has been linked to the activation of the salicylic acid (SA) pathway during pathogen invasion (Stein 2006). Upon detection of an attempted invasion there is an increase of PEN1 and PEN3 recruitment, while PEN3 away from the infection site is recycled into endosomes and transported along the actin cytoskeleton, via myosin motors, before being enriched at the infection site. Like FORMIN4, these have been shown to be organised in a punctate pattern, although these endomembrane domains are distinct from those containing FORMIN4. These penetration defence proteins are recycled and transported, reaching a steady state of enrichment on the time scale of 1-4 hours (Sassmann et al. 2018) while CWA formation and maturation is closer to a 24-48 hour time scale (Shimada et al. 2006). The increased density of PEN3 at and around the appressorium is hypothesised to enable better excretion of toxins and compounds which suppress PAMPs and effectors, enabling formation of papillae and the CWA before maturation of the appressorium and without requiring a hypersensitive response. This process is less impactful on plant growth and crop yields, while being non-specific and not requiring additional genes.

In order to facilitate the endocytic recycling, lipid flippase proteins are recruited for vesicle formation. As PEN3 is constantly being recycled between the plasma membrane and the TGN/early endosomes, any inhibition of the lipid flippase, such as is seen in the ALP3 mutant in *A. thaliana*, will result in a significant bottleneck and therefore a drop in the membrane concentration of PEN3 (Underwood et al. 2017). Other immune defence proteins, such as PEN2, are also suggested to be cycled through the TGN, so any bottleneck would be devastating for penetration defence. Transport and positioning of the TGN is also therefore likely to be important in the timely delivery and enrichment of penetration defence proteins. While still not completely understood, the benefits of strengthening the non-host immune response are significant in terms of global food security and efficiency of crop production.

Activated signalling complexes are constantly being turned over during PTI and

ETI, mediated by receptor endocytosis (Li and Day 2019) in order to maintain surveillance for the immune system (He et al. 2017). The majority of the plasma membrane integrated immune system components used during PTI are controlled through clathrin-mediated endocytosis (CME), which relies on the actin cytoskeleton (Nagawa et al. 2012). This is achieved by loading a clathrin coat onto the membrane components, enabling the components to attach to actin filaments, which can then polymerise and grow (Li and Day 2019), a process known as actin flow (Kaksonen and Roux 2018). In animals, actin flow is mediated by myosin and the Arp2/3 complex, although in plants the Arp2/3 complex may not be necessary as the mutant in *A. thaliana* is non-lethal (Li et al. 2003), which would be expected if CME was inhibited.

1.6 Actin Cytoskeleton

Amongst a multitude of other functions, the cytoskeletal network, prevalent in almost all eukaryotic cells, provides physical shape and structure to cells, aids in cell growth, and plays a key role in trafficking (Liang and MacRae 1997). Formed from polymerisation of discrete protein sub-units, the cytoskeleton connects to various organelles (including the nucleus) and the plasma membrane. This modular nature of the cytoskeleton allows it to be dynamic, adapting as necessary to environmental changes relayed via a host of signalling processes (Schmidt and Hall 1998). Many of the cytoskeletal sub-units have been highly conserved during evolution and are found in most eukaryotic cells, with homologues even present in some prokaryotes (Wickstead and Gull 2011).

The cytoskeleton is typically divided into three distinct components: microtubules, intermediate filaments and actin (Fletcher and Mullins 2010; Jülicher et al. 2007). Microtubules, the thickest cytoskeletal component at about 25nm in diameter, are hollow tubes consisting of repeated α- and β-tubulin sub-units (Wade 2009). In animals and fungi, they play a number of roles including aiding in the formation of flagella or cilia (Vladar et al. 2012), providing structures for material transport, and positioning of the mitotic spindle during cell division (Nédélec et al. 1997). In plants, microtubules retain a role in cell division but also guide cell wall development through their relationship with wall-building enzyme complexes in the plasma membrane (Paredez et al. 2006).

Unlike the globular units of microtubules and actin filaments, intermediate filaments are themselves constructed from filamentous sub-units, and confer strength as well as stress resistance to the cell (Fuchs and Weber 1994). Although they are present in almost all mammalian cells, their existence in plants is still hotly debated (Nick 2020).

Finally, actin filaments, also known as microfilaments, are the narrowest components of the cytoskeleton and are constructed from globular actin sub-units (G-actin) that assemble to form a helical structure 5-7 nm in diameter (Pollard and Borisy 2003). In combination with myosin motors, actin aids in transport by providing the roads and pathways for cellular cargo (Brawley and Rock 2009). Actin microfilaments are present as both individual filaments and bundled into thicker filaments, and play a key role in plant cell growth and internal transport (Svitkina 2018).

1.6.1 Actin in Plants

Although actin is present across eukaryotes, there are important differences between kingdoms, not least in plants. The versatility of actin enables it to play a key role in many aspects of plant life, including root tip growth (Geitmann and Emons 2000) and cell division (Paez-Garcia et al. 2018). The ubiquity of the actin cytoskeleton, alongside the fact it can be constantly remodelled in response to external forces and environmental factors, means that active, directional transport is always available throughout plant cells. This transport is particularly fast in plants, with Golgi speeds reaching up to 7 $\mu m\, s^{-1}$ (Geitmann and Nebenfähr 2015). This speed is key for transport in long cells such as the hypocotyl. To enable these speeds the actin cytoskeleton typically runs mainly parallel to the long axis of the cell, sandwiched between the vacuole and the plasma membrane and perpendicular to the orientation of microtubules (Sampathkumar et al. 2011). The network consists of two distinct populations: the fine F-actin arrays that undergo rapid and stochastic remodelling with polymerisation rates in *A. thaliana* hypocotyls reaching 1.7 $\mu m\, s^{-1}$ (Thomas 2012), and the thicker bundles responsible for long-range transport.

The actin cytoskeleton in plants is regulated through a large array of genes and proteins that are coordinated by numerous signalling pathways. External influences on the cell, whether from environmental factors (such as light or temperature) or other organisms

(such as pathogens like *Blumeria graminis* that can attack the cell well through enzymes or physical forces), can stimulate these pathways, triggering adaptations in the actin network to counter the stimulus. Actin plays a key role in the response to pathogen attack, rapidly remodelling itself at the site of the plasma membrane where the pathogen makes contact (Schmidt and Panstruga 2007; Henty-Ridilla et al. 2013). F-actin aggregation at the attempted penetration site, which enables cytoplasm accumulation (Takemoto et al. 2006), can occur within approximately 20 seconds and can be triggered by small applied forces of only 4 μN (Branco et al. 2017). Depolymerisation of actin using drug treatments causes the catastrophic failure of this focused penetration defence (Kobayashi et al. 1997), as the transport of key defence proteins such as PEN2 and PEN3 is actin-dependent. Conversely, crop breeders have taken advantage of a mutation named *mlo* that enhances the actin response in barley to offer increased protection against some types of fungi (Miklis et al. 2007). Pathogens are under selective pressure to adapt their repertoire of secreted effector proteins to suppress plant defences, including the actin cytoskeleton (Leontovyčová et al. 2020). *Pseudomonas syringae* secretes the effector protein HopW1 which results in the reduction of f-actin and inhibits exocytosis, a key (actin-driven) process of plant immunity (Kang et al. 2014). The SA-pathway has been shown to be triggered by actin disruption (Matoušková et al. 2014; Kalachova et al. 2020), resulting in SA accumulation and activation of SA-responsive genes. SA binds to and alters the effects of many proteins to aid in defence from biotrophic pathogens, and activation of the SA-pathway is important for systemic-acquired resistance (SAR) which may lead to improved plant resistance to pathogens (Leontovyčová et al. 2019). Barley powdery mildew fungi can secrete effectors (ROPIP1) which target the microtubule array, another component of the cytoskeleton (Sabelleck and Panstruga 2018). Local destabilisation of the cortical network architecture would likely support fungal penetration.

1.6.2 Properties of Actin

Monomers of actin (G-actin) can be assembled into filamentous actin polymers (F-actin), initially through the nucleation of G-actin into a trimer, before additional G-actin units are sequentially added (see Fig. 1.2) (Rottner et al. 2017). One end of the filament (called the barbed or positive end) has an exposed ATP binding site that is missing from the other

end (the pointed or negative end), thus giving the structure an overall polarity (Narita et al. 2012). While polymerisation occurs at both ends, the barbed end has a significantly increased rate of assembly. G-actin monomers can also leave both ends, resulting in disassembly. G-actin monomers bound to ATP are more likely to be assembled, shortly after which the ATP is converted to ADP-P_i through nucleotide hydrolysis. After a delay, estimated to be around the order of seconds (Burnett and Carlsson 2012), the P_i is then released, leaving just ADP in the binding site (Neuhaus et al. 1983). The various ADP-ATP combinations contained within the nucleated monomers gives an indication of the age of that part of the filament, which can be detected by disassembly machinery such as Actin Depolymerising Factors (ADFs; also known as cofilins) (Henty-Ridilla et al. 2014). Filament polarity results in frequent growth at the barbed end and disassembly at the pointed end, known as treadmilling, which allows the structure to be adaptive to changes in conditions and external forces. F-actin can also bundle together, forming thicker and straighter filamentous structures that are more stable and have a longer lifetime. These cross-linking and bundling processes are initiated by proteins such as villin and fimbrin (Tang and Janmey 1996).

A range of actin binding proteins (ABPs) work in harmony with the cytoskeleton to enable a higher level of organisation (see Fig. 1.2). For example, the actin related protein (ARP) 2/3 complex is an actin nucleator (Deeks and Hussey 2005; Mathur 2005), which works alongside a range of formins, aiding in the control of the rate and timing of actin assembly and branching (Vidali et al. 2009; Deeks et al. 2010). ADF/cofilin and cyclase associated protein (CAP) bind to G-actin and help to regulate the available pool of actin monomers for assembly (McCurdy et al. 2001). Capping proteins bind to the barbed end of F-actin and prevent both assembly and disassembly, thus controlling length and growth. Conversely, severing proteins such as ADF/cofilin and villin sever filaments (Hussey et al. 2006), usually towards the pointed end where the actin is bound to ADP (Deeks et al. 2002) and so shorten the filament whilst creating a new barbed and pointed end.

Profilins are proteins that work in collaboration with plant formins to regulate several aspects of cytoskeletal development and growth. *A. thaliana* contains five isoforms of profilin, of which AtPRF3 has been found to have a disordered region that has a high

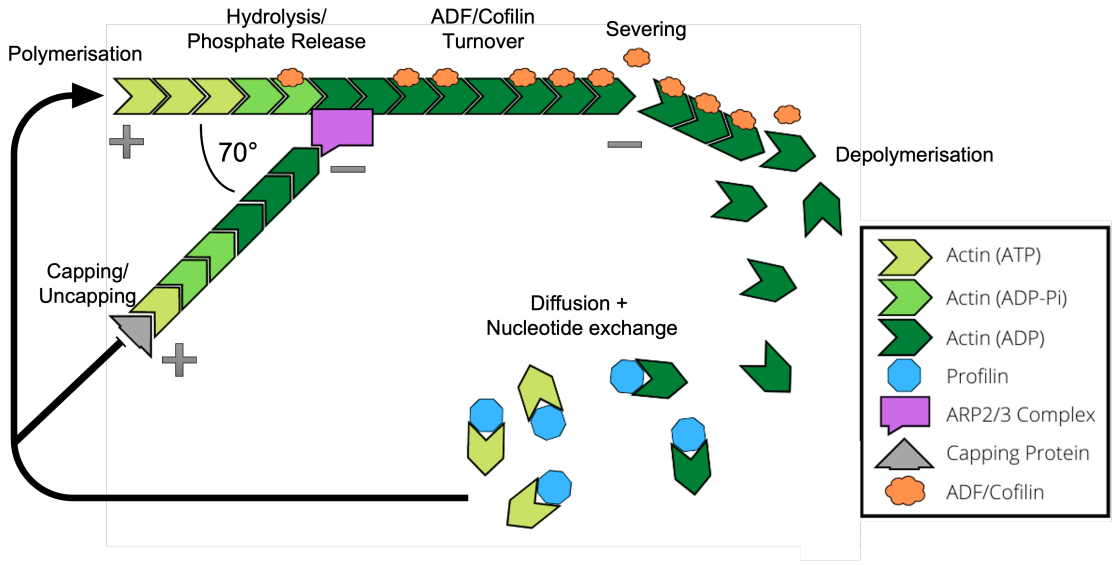

Figure 1.2: Actin network dynamics. Actin within the cell consists of both single monomers (G-actin) and branched filaments (F-actin). Filaments have an orientation, with a barbed end (+) and a pointed end (-). Polymerisation and disassembly can occur at both ends, but polymerisation typically occurs at a higher rate at the barbed end, while disassembly is more common at the pointed end. A range of proteins and signalling pathways contribute to the turnover of actin monomers, which drives the structure of the actin cytoskeleton and enables a high level of organisation and adaptation. The Arp2/3 complex is involved in filament nucleation and branching, while capping proteins bind to the barbed end to prevent both polymerisation and depolymerisation. Severing proteins such as ADF/cofilin can break the filament into two pieces, creating an additional barbed and pointed end.

affinity for the polyproline region of formin. AtPRF3 binding to formin and then subsequent quick oligermerisation has been shown to inhibit AtFH1-mediated actin nucleation. In response to PAMPs, the transcription of AtPRF3 and protein degradation are altered in order to modulate actin turnover (Sun et al. 2018). During plant immune responses this contributes to cytoskeletal remodelling and ensures the maintenance of the filamentous actin nests in proximity to the attempted penetration site (Qin et al. 2021; Sassmann et al. 2018).

The numerous types of protein working in concert to keep the cytoskeletal network organised allows it to be adaptive and efficiently restructured as required. ADF (Henty-Ridilla et al. 2014, profilin (Sun et al. 2018), formin (Sassmann et al. 2018) and the ARP2/3 complex (Qin et al. 2021) have all been implicated in the changes in structure and dynamics that place the actin cytoskeleton in a defensive poise against microbes. Each will have a subtle input into the behaviour of the actin array and decoding these contributions provides information about the key control points driving defence. Unfortunately, uncoupling the cascade of signalling molecules and cytoskeletal regulatory proteins is a complex

process, therefore there is still a lack of understanding regarding the coordination of these local actin and trafficking responses.

1.7 Previous Immunity Studies

Powdery mildews are one of the most studied pathogens in innate plant immunity and they have been shown to have reduced penetration success post-lignification of papillae in cereals. Lignification is essentially the process of creating wood, and it is achieved through the synthesis of monolignols that are polymerised to form lignin. A series of eight genes are responsible for monolignol synthesis in wheat, with 6 of these gene transcripts accumulating in near synchronisation. Gene silencing was achieved with RNAi by particle bombardment, and showed that the host immune response to wheat powdery mildew *B. graminis* f. sp. *tritici* (Bgt) was only 60% successful. For a non-host response using barley powdery mildew—Bgh—there was a 300% increase in successful penetration attempts, highlighting the importance of papillae lignification in successful immune responses (Collinge 2009).

Phosphatidic acid (PA) and ROS are elevated in PTI, and the timing of their increases roughly correlates with rearrangements in the actin cytoskeleton (Cao et al. 2022). Isoforms of the lipid PLDβ have been shown to be required for actin accumulation during PTI in response to flg22, a PAMP widely used in basal defence studies (Jelenska et al. 2017). PA generated by the PLDβ signalling pathway (Wang 2004) acts upstream of ROS signalling to inhibit capping protein activity which drives the actin cytoskeletal remodelling.

The importance of the cytoskeleton in achieving a competent immune response is highlighted by simultaneous remodelling of the actin network in response to pathogens due to signalling from both the internal plant response mechanisms and the effectors secreted by a pathogen (Li and Day 2019). The cellular response that is plant-regulated is hypothesised to support immune signalling and downstream defence signalling (Day et al. 2011), as several PAMPs (*e.g.* flg22 and chitin) have been shown to trigger PRRs which results in actin reorganisation in *A. thaliana* epidermal cells (Henty-Ridilla et al. 2013;

Henty-Ridilla et al. 2014) and guard cells (Shimono et al. 2016). The cytoskeletal reorganisation is seen as actin bundling at the interface of a mature appressoirum from avirulent *bgh*, but the changes are not seen with virulent *bgh* strains (Miklis et al. 2007), suggesting the pathogen suppresses the response in order to make the host cell more susceptible. *P. syringae* has been shown to disrupt and modify the microtubule network with its HopZ1a effector (Lee et al. 2012), in an attempt to disrupt key immune processes such as trafficking, while another of its effectors—HopW1—directly depolymerises f-actin during infection (Kang et al. 2014). This can result in fragmented regions of the network, blocking protein trafficking and endocytosis.

The cytoskeleton has been shown to exhibit two distinct populations of actin: the finer filaments which display stochastic and very dynamic behaviour, and the thicker bundles which are much more stable but still undergo near-constant remodelling. These fine filaments polymerise at extremely high rates: 1.7 $\mu m\, s^{-1}$ in *A. thaliana* hypocotyl epidermal cells (Thomas 2012) and undergo remarkable buckling and straightening behaviour, likely caused by manipulation from transiently binding microtubules (Sampathkumar et al. 2011). The cytoskeleton is coupled to the plasma membrane, which enables it to sense and transduce a variety of external signals from the cell wall and relay it to the cell.

Network analysis of the actin cytoskeleton in *A. thaliana* hypocotyl cells in relation to transport of the TGN revealed several properties which enabled efficient transport even in times of disruption (Breuer et al. 2017). Tracking of both the TGN and analysis of the position and thickness of actin cables revealed that golgi transport was essentially mostly reliant on molecular motors and the cytoskeleton, not passive diffusion or even cytoplasmic streaming. This network organisation can be used to predict movement of the TGN as well as provide information about the functional requirements. The algebraic connectivity of the network, describing how many redundant paths are available between the start and end points, was significantly higher than a random network, ensuring efficient transport even if routes are blocked or the network is undergoing distinctive changes, such as during growth or PTI. This is particularly relevant to hypocotyl cells as they are undergoing rapid elongation in search of sunlight. The cytoskeleton is also tuned towards a shorter path length, in order to increase accessibility of the network, which is key given

the slow rate of diffusion in a congested cytoplasm. The wiggling nature of the movement of the TGN has the same power law distribution as foraging animals and microbes, an optimised search strategy, displaying the efficiency of transport which enables rapid and effective PTI.

Microneedles can be used to stimulate an immune response in plant cells due to physical pressure and cell wall damage. The reorganisation can take less than two minutes to be completed, with the initial changes being visible about 22 seconds despite very small forces, down to 4 μN being applied (Branco et al. 2017). The speed of reorganisation is likely due to this process being vital for subsequent steps in the immune response, such as the transport of key defence proteins. Research has previously shown that the speed of CWA formation is related to the effectiveness of the plant basal response (Hückelhoven 2014; Voigt 2014) and gentle physical stimuli can improve immune defences (Benikhlef et al. 2013). Moving the stimulus to a different region of the cell, or an adjacent cell, after a response was noted, yielded a near identical response, therefore highlighting that a single cell can defend from multiple penetration attempts in succession. Whether the responses could occur simultaneously remains to be seen.

1.8 Thesis Overview

The next chapter will introduce a range of different quantitative techniques that are used both in this research and the broader field, as well as introducing the role of mathematical modelling and what these models hope to achieve. The third chapter will cover the experimental set up of artificially generating an immune response, discussions of the validity of these methods and our findings in the transport and distribution of PEN3 in the membrane. Chapter four covers the development and testing of the image analysis software—DRAGoN—as well as its limitations and the motivation behind it. The next chapter analyses the experimental results of using DRAGoN on acquired data of the actin cytoskeleton in *A. thaliana* and discusses the implications of the outcomes. Chapter six shifts the focus back to PEN3, using experimental data to determine its diffusion coefficient in the membrane. From here, we model PEN3 delivery and distribution in an attempt to determine why the site of enrichment is shaped and sized as it is. The seventh chapter

will discuss the implications of my research in the wider field and what should be done moving forward, and how this might aid in the goal of achieving global food security. The final chapter will summarise and conclude my findings with a brief look to the future.

Chapter 2

Quantitative Techniques and Modelling

Before the introduction of various metrics to quantify the quality of research and its impact (such as the H-index), scientific research tended to be focused on a single discipline (Morris and Tusscher 2021), especially as many of the foundations of each discipline were still in their infancy or even undiscovered. While many keep their research solely locked into one specific area in order to optimise these metrics, the value of interdisciplinary research is beginning to be realised. As biologists begin to look deeper and down at a much smaller scale, effect sizes can reduce while noise remains persistent, making changes more subtle and harder to detect. The role of quantitative methods, mathematical modelling, and especially statistical testing begin to become increasingly apparent, somewhat blurring the lines between biology, physics and mathematics, and this continuous dialogue between experiments and theoretical models will be instrumental in future progress (Morris 2018).

2.1 Quantitative Techniques

Understanding the underlying physics behind transport mechanisms is important to establish how plants respond to their environment, and an understanding of the physical forces at play is important for plant growth and development (Tomkins et al. 2021). Quantitative approaches in plant biology have led to a host of ground-breaking discoveries

(Morris and Tusscher 2021), and as there are many sources of noise in the world, robust quantitative techniques are required for responsible analysis (Autran et al. 2021).

Quantitative methods historically have aided the research into guard cell ion dynamics as well as calcium signalling (Tomkins et al. 2021), with image analysis also proving fruitful. Some calcium signalling in plants is long-range, directed along vascular tissue, and through the use of image analysis, it was shown that these signals are likely mediated by diffusion (Bellandi et al. 2022). By wounding cells, observing and quantifying the movement of amino acids, it was shown that these calcium channels are activated by the amino acids, which arrive by diffusion in the apoplast. Tracking of the calcium revealed that it is transported by bulk flow over long distances, but this calcium isn't sufficient to trigger all immune responses and therefore other mobile chemical messengers are required.

Some phytopathogens use open stomata to get deeper into the leaf tissue before attempting to penetrate cell walls. Because of this, guard cells may detect PAMPs through PRRs on their surface and close stomata as an immune response (Li and Day 2019). Using image analysis, it was possible to quantify this process in response to environmental cues and mutants (Bourdais et al. 2019), and would be useful in testing effectors which attempt to reopen stomata (Asai and Shirasu 2015). The use of automation enables high throughput of data with minimal bias, and release of the software enables transparency and repeatability of this method.

Transport of cargo is an area which image analysis can prove highly useful and this has been utilised on several occasions (Breuer and Nikoloski 2015; Breuer et al. 2017; Weichsel et al. 2010). Kymographs represent spatial positions over time, and this can be used with time-series images to determine both speed and direction of cytoskeletal cargo (Racine et al. 2007). Quantitative comparisons of the trajectories of the vesicular cargo, combined with information of the underlying microtubule network, showed that the network was main factor in the transport trajectories, rather than the actual cargo itself.

The role of the cytoskeletal network in transport makes it a highly explored area of plant cell biology, yet many questions still remain. Analysis of the coherence of an image

(*i.e.* the amount and quality of clear structures) revealed that it is a sufficiently accurate statistic to detect global alterations in cytoskeletal organisation (Weichsel et al. 2010), although does not describe the specific changes. The density of the cortical cytoskeleton in *A. thaliana* has been estimated by filtering and skeletonising images of the actin network, then counting the fraction of pixels in the skeleton compared to the ROI size (Rosero et al. 2014). This technique was sensitive enough to detect quantifiable differences between a mutant and the wildtype, as well as after a depolymerising drug treatment. As actin bundles are brighter than their unbundled counterparts, increased measurements of the skewness of the intensity distribution of actin images has been used to quantify the promotion of filament bundling.

Breuer et al. have developed an actin network extraction tool called CytoSeg (Breuer et al. 2017; Nowak et al. 2020), which leverages a Python backend with GUI implementation in ImageJ. The actin network is described by a weighted graph (*i.e.* a mathematical network of nodes connected by weighted edges) which builds upon the DeFiNe method (Breuer and Nikoloski 2015). This yields powerful and simple analysis for transport networks, including routing and distances travelled, well-suited for analysis of vesicle and organelle transport. However, one limitation of this approach is that filaments are represented by straight lines, a simplification that can miss key properties of actin networks such as filament curvature. Not knowing the full network shape (with realistic non-straight filaments) can make network analysis more difficult and can miss subtle network changes that are often seen in mutants and drug treatments.

Many of the methods required to 'beat' the diffraction limit and achieve super resolution require quantitative techniques (Huang 2010; Komis et al. 2015). Single molecule localisation microscopy methods (*e.g.* PALM, STORM) reconstruct an image based on several frames, each with a single molecule either temporarily localised (PALM), or a fixed molecule is temporarily emitting (STORM). These events are diffraction limited, but by knowing the point spread function of the imaging setup and by determining the centre of each emission, the points can be superimposed to achieve a single, super resolution image.

2.2 Statistical Testing

When analysing quantitative data, it is important to perform sufficient statistical testing in order to determine whether the null hypothesis should be accepted or rejected. Depending on the type of data variables (*e.g.* discrete or continuous), the distribution of the data, or the total number of groups being tested, a range of statistical tests are available. The first step is to explore your collected data to learn its properties, such that the correct test can be selected. Here I will detail a few of the more common tests, as well as those that were useful for my data.

2.2.1 Chi-squared Test

When observing phenomena which either occur or do not occur, the total occurrence is usually reported as a frequency in the range [0,1], a percentage, or as a total count for each outcome. As this data is discrete, comparing means or standard deviation is not appropriate. In this case, a chi-squared (χ^2) test is needed. This non-parametric test analysing discrete data across multiple (2+) groups was first introduced by Karl Pearson in 1900 (Mendenhall et al. 2003; Rayner et al. 2011). The groups are tested in a pairwise manner, with the differences between observed O and expected E observations being calculated as,

$$\chi^2 = \sum_{i=1}^{n} \frac{(O_i - E_i)^2}{E_i}. \tag{2.1}$$

With the χ^2 value, and the known degrees of freedom in the data set, the probability of the null hypothesis (the categorical variables are independent and bear no difference in outcome on the measured statistic of the population) being true can be determined. Most statistics software (*e.g.* R, SPSS) will present the p-value automatically, while historically you would need to compare your computed χ^2 statistic against a table to determine if it was sufficient to reject the null hypothesis or not. When small (< 20) or low frequency (< 5) data are used, Fisher's Exact test is recommended (Cochran 1954).

2.2.2 Repeated Tests

Perhaps the most common, and one of the most simple statistical tests is the students t-test. This is used for comparing the means of a continuous variable across different groups, to

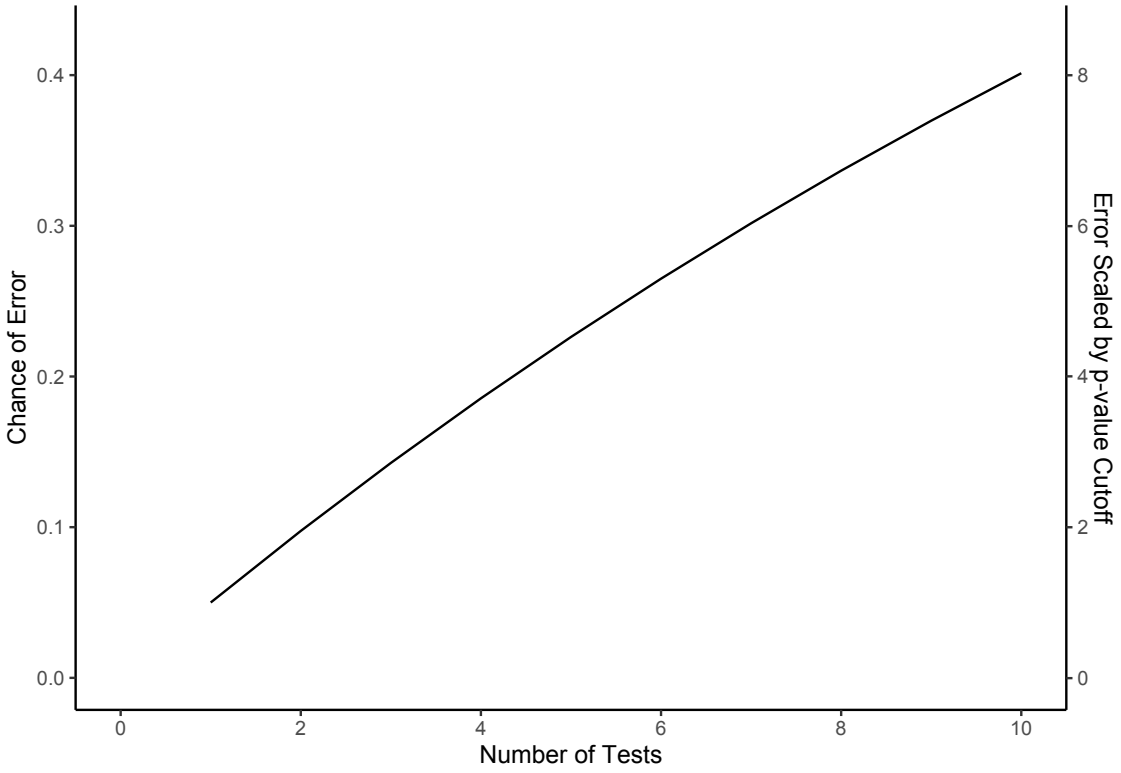

Figure 2.1: Type I Error. By repeatedly using pairwise testing between groups, the chance of a Type I error increases. The left y-axis shows the overall chance that, by using the cutoff p = 0.05, the null hypothesis may be erroneously rejected, for a given number of repeated tests. The right y-axis has this value scaled by the cutoff p = 0.05, therefore shows the correction that would need to be applied to achieve the desired cutoff for repeated testing.

determine if there is a difference. This is perfectly acceptable for two groups, but in the case of additional groups, the issue of repeated measures arises, which increases the chance of a type I error. If the null hypothesis gets rejected with a p-value of 0.05 (*i.e.* only a 5% chance that you have incorrectly rejected the null hypothesis), then the chance of being incorrect *at least once* when doing n repeated measures is given by

$$P(n) = 1 - (1 - p)^n, \tag{2.2}$$

where p is your p-value cut-off. Sometimes it is difficult to avoid repeated testing, in which case a correction factor may be applied to the p-value in order to ensure consistency. A common choice to overcome either multiple hypothesis testing, or repeated testing, is the Bonferroni correction, where the cutoff value is divided by the number of pairwise tests performed (Kim 2017). As can be seen in Eq. 2.2 and Fig. 2.1, this can be both an oversimplification and an over-correction in many cases, as it only holds in the limit of

$p \to 0$. Therefore, it is likely best to calculate the divisor for the correction using $P(n)/p$ or use a testing method which avoids or accounts for this issue.

2.2.3 ANOVA

Avoiding the issue of repeated testing can be done through the use of Analysis of Variance (ANOVA), enabling the testing of the null hypothesis,

$$H_0 : \mu_1 = \mu_2 = \ldots = \mu_n. \tag{2.3}$$

As with all parametric tests, this one has a range of assumptions, such as requiring normally distributed data. For large sample sizes, however, the central limit theorem states that sample means are more normally distributed than their component data (Le Cam 1986) therefore this issue may be ignored (albeit with a possible loss in power). Despite this, it is much better to transform the data and use the correct test, rather than leaving it as is and using the wrong one. There are plenty of common transformations to normality, such as the use of arcsin for fractional [0,1] data, or logarithmic transforms for data whose residuals scale with the mean (Stahle and Wold 1989). If this, or the assumption that variances are the same (at least within an order of magnitude) is violated, then non-parametric tests such as Kruskal-Wallis can be employed instead. An extension to the ANOVA for multiple dependant variables—Multivariate ANOVA, or MANOVA—also exists, by first combining the multiple variables into a single one, before running the ANOVA.

As the name ANOVA may suggest, this statistical model looks at the variance both within a group and between groups (this groups can be split across multiple independent variables or just one), estimating the variance due to residual error σ^2 (caused by errors in measurement, noise etc.). This can be compared to estimates of variance between means σ_μ^2. The computed F-statistic of the ANOVA is therefore an estimate of

$$F(n) = \frac{\sigma^2 + n\sigma_\mu^2}{\sigma^2}, \tag{2.4}$$

which will exceed unity when σ_μ^2 is non-zero (Stahle and Wold 1989). As with the Chi-squared test, the calculated test statistic and the degrees of freedom can be used to compare

to a significance table, in order to determine whether to reject the null hypothesis or not. While this is informative, for $n > 2$ we do not know which group has a difference in means, or whether more than one group does. Obtaining this information requires further (post-hoc) tests, where issues of repeated testing may arise.

Many of the post-hoc tests are designed to compensate for repeated testing (Kim 2017), with common statistical software reporting an adjusted p-value. This is done so that depending on the number of comparisons made, the total type I error rate still remains at 0.05, while reporting the numbers in such a way that the adjusted value cutoff is still 0.05. A commonly used post-hoc test following an ANOVA is the Tukey Honest Significant Difference (HSD) as it does the adjustments automatically (Ludbrook 1998). It is important to realise that the number of pairwise comparisons N_p given by,

$$N_p = \frac{n(n-1)}{2}, \tag{2.5}$$

increases much faster than the increase in the number of groups, therefore significantly reducing the required significance level (*i.e.* requires a smaller, non-adjusted p-value to reject the null hypothesis with the same type I error) and experimental power. Often it is wise to reduce the group number or only observe a subset of the groups in order to detect more subtle effects.

2.3 Mathematical Modelling

The benefit of quantifying data is that the noise and variability within the data can also be quantified (Autran et al. 2021), enabling models to account for both the inner dynamics and the external environment factors. Improvements to computational and technical processes has resulted in a shift from reductionist to systems biology, which is important when observing such complex, multi-feedback processes (Morris and Tusscher 2021). The combination of modelling and high spatiotemporal resolution tools has led to a new standard in plant science (Autran et al. 2021). When generating a model, the hypotheses to be tested must be formalised, which ensures they are testable, and modelling systems enables preliminary testing, often for cheaper while being faster. The model predictions

can be verified experimentally, which in turn drives feedback on the model, yielding new predictions to test and driving the boundary of knowledge forward.

2.3.1 Diffusion

Many areas of quantitative biology are concerned with the physics governing transport and trafficking (Martins et al. 2013), where modelling has provided insight into many basic aspects of transport (Lin et al. 2021), in which the role of diffusion may be important and therefore cannot be ignored. The use of diffusion models has also been instrumental in the recent progress of AI generated images (Ulhaq et al. 2022; Borji 2022). The diffusion equation, analogous to the heat equation, was first derived by Adolf Fick in 1855 (Fick 1855) and can be derived from Fick's first law and the continuity equation. Fick's first law links the diffusion flux J to the gradient of the species concentration $\rho(\vec{r}, t)$, through the constant of diffusion D as,

$$J = -D\nabla\rho(\vec{r}, t). \tag{2.6}$$

The continuity equation simply states that the change in density or concentration in a part of a system can only be through movement of material in and out of that region (*e.g.* nothing is created or destroyed) and is represented as,

$$\frac{\partial\rho(\vec{r}, t)}{\partial t} + \nabla \cdot J = 0. \tag{2.7}$$

By substituting in our flux to the continuity equation, making the assumption that D is constant in all regions, therefore ∇ has no effect on it, we arrive at,

$$\frac{\partial\rho(\vec{r}, t)}{\partial t} - D\nabla \cdot \nabla\rho(\vec{r}, t) = 0, \tag{2.8}$$

where $\nabla \cdot \nabla$ is the Laplacian, often written as ∇^2 or Δ. Rearranging gives us Fick's second law, the diffusion equation,

$$\frac{\partial\rho(\vec{r}, t)}{\partial t} = D\nabla^2\rho(\vec{r}, t) \tag{2.9}$$

It is worth noting that the mechanisms behind diffusion (driven by thermal motion) and osmosis (driven by pressure) are different (Tomkins et al. 2021). A difference in thermal energy (or concentration) will produce a different rate of particle trajectories, resulting

in mixing and passive transport. Osmotic flow, however, is an entropic effect driven by a pressure difference across a membrane. Both diffusion and osmosis are important for transport between cells, but studying and separating them requires quantitative methods and modelling.

Many transport tunnels between cells in plants (*e.g.* plasmodesmata and aquaporins) are narrow, and may have complex, time-dependent geometries, therefore modelling flow with particle-based methods may be required (Hughes et al. 2021). Modelling the physics of advection (osmosis) and diffusion yielded insight into sugar loading in the phloem, facilitated through plasmodesmata, and similar mechanisms may be present in aquaporins (Tomkins et al. 2021). Quantifying parameters of plasmodesmata experimentally can be time-consuming experimentally, as well as costly (Hughes et al. 2021) whereas modelling has the potential to be quick and cost-effective, and may provide a framework to extend to other systems.

Passive transport of molecules within cells can be modelled by splitting the cell into regions and solving partial differential equations (PDEs) such as Eq. 2.9, with a host of previously established Monte Carlo methods and algorithms available (Martins et al. 2013), alongside extensions to include advection (Ekebjærg and Justesenu 1991). Transport of organelles, however, is a little more difficult. Brownian motion is often insufficient to reduce gradients which involve membranous organelles (Lin et al. 2016) due to the crowded nature of the cytoplasm. In these crowded environments, normal diffusion breaks down which results in anomalous (or sub-) diffusion (Bressloff and Newby 2013; Tomkins et al. 2021).

2.3.2 Other Transport Methods

Normal diffusion results in a linear relationship between mean squared displacement (MSD) $\langle r^2 \rangle$ and time t, with a gradient related to the diffusion constant. In anomalous diffusion, however, the relationship looks like,

$$\langle r^2 \rangle \propto t^{\alpha}, \tag{2.10}$$

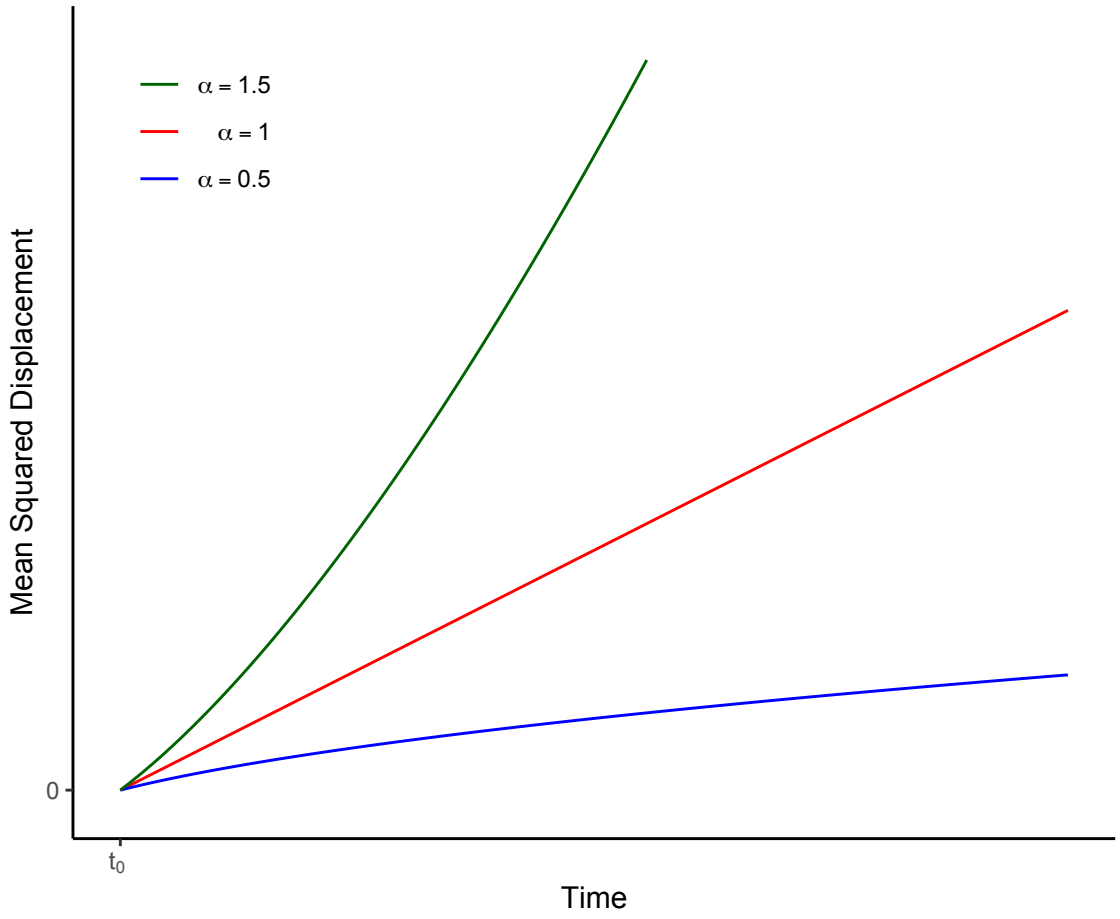

Figure 2.2: Normal and anomalous diffusion. Three particles with identical diffusion constants have drastically different displacements based upon their diffusive regime. Super diffusion, normally the result of active transport, results in significantly greater distance covered, particularly over longer timescales, whereas subdiffusion keeps the particle fairly confined in space.

where α is unity for normal diffusion, smaller for anomalous diffusion and greater for super diffusion, as shown in Fig. 2.2. Super diffusion is usually the result of active transport (Reverey et al. 2015; Chechkin et al. 2017), such as myosin motors walking vesicles along the cytoskeletal network.

Due to the size of organelles, any long range, directed trafficking is primarily due to active transport, while local, passive transport is most likely to be in an anomalous diffusion regime, with some diffusion in less crowded regions (Lin et al. 2021). Cytoplasmic flow may also achieve unidirectional transport, but this usually is only over short distances, although extremely long distance streaming can be seen in the aquatic plant *Chara* (Goldstein and Meent 2015). The even distribution of organelles and other membrane-bound compartments is vital for the survival and physiology of eukaryotic cells, which

is why a range or organisms have been shown to coordinate between passive and active transport mechanisms to achieve these distributions. Polar actin forces and opposing microtubules have been shown to enable the even distribution of peroxisomes and early endosomes in filamentous fungi (Lin et al. 2016). Organelle transport is often modelled as a combination of drift-diffusion (diffusion with a slow, unidirectional drift term from the cytoplasmic flow) and long-range, molecular motor driven transport.

Quantitative techniques and modelling have been invaluable in researching signalling networks, as the feedback and signalling mechanisms are so complex (Autran et al. 2021). Calcium ions are frequently part of these networks, and these molecules undergo a range of different transport regimes as an inter- and intra-cellular signalling molecule (Martins et al. 2013). Transport in the cytosol or through plasmodesmata is likely to result in anomalous diffusion, whereas calcium released into the apoplast is likely to diffuse normally and freely, while some signalling designs will result in transport through streaming or bulk flow.

2.3.3 Modelling Outside of Transport

Outside of transport, the reaction-diffusion equation can be useful for modelling the patterns of morphological diversity in bacterial colonies (Mimura et al. 2000). The use of network based algorithms (*e.g.* Dijkstra's) can provide insight into the organisation and connectivity of vascular tissue (Al-Diri et al. 2010) or the cytoskeleton and provide insight into the requirements of their roles. Image analysis of the ER has been used to extract and quantify the network geometry (Lin et al. 2017), and was found to be quantitatively similar to their ER model. Modelling the mechanisms of a system can reproduce experimental observations and can be used to make predictions which can be tested experimentally (Martins et al. 2013). This quantitatively similar ER model enabled a range of parameters to be tested in the model to provide further insight into what should be probed in the future.

Many systems, or aspects of systems, are difficult to probe experimentally (Sambade et al. 2012), and therefore modelling can be used to provide mechanistic insight previously unavailable. Modelling the orientation of fibres in guard cells provided understanding of

the requirements for guard cell opening, which drove the choice of mutants used to test hypotheses and validate model predictions (Woolfenden et al. 2017). This model enabled insight into the subtle differences in shape and how this generates various cell wall properties.

One issue with plants is their photosensitivity and the fact that various signalling pathways are triggered by light. The mechanisms behind the transition of microtubule arrays from longitudinal to transverse were found through modelling (Allan et al. 2022), as this is part of a light-signalling pathway. Visualising this experimentally can result in growth inhibition, therefore mathematical modelling can sidestep this issue.

One of the biggest barriers to modelling is the issue of defining and estimating parameters (Sumner et al. 2012). These parameters should be physical properties, which also have a relevant biological meaning, limiting the use of emperically derived properties where possible (Yin and Struik 2010). It is easy to perfectly fit any experimental data given enough parameters, but the point is to do so with as few and yet meaningful parameters as possible, while ensuring they are experimentally measurable (Beulke and Brown 2001). This also would likely simplify the task of comparing between models, as it is important to benchmark and understand their ability to represent the system at hand (Pullen and Morris 2014). It is more beneficial; however, to collect data from additional variables of the system, as opposed to collecting more data from just a few, and this increased knowledge can more effectively drive experimental design. It is important to consider experimental and model design when collecting preliminary data, and to construct the model in a way that it should be able to probe scenarios outside of the benchmarked parameter set.

Many biological systems have complex, multimodal fitness landscapes, where the issue of finding the desired optimum may be challenging. These systems will have many optima for different constrained regions of parameter space, yet still likely have a single, global optima over the entire parameter space. Searching the entire parameter space is very time-consuming, and given biological context, many of these parameter values not be useful in the system, as they might not be biologically relevant or realistic. The local optima, however, may still be problematic depending on the choice of starting parameter and optimisation algorithm. Some prior knowledge of the system, such as the fitness land-

scape or the nature of the parameter space, can aid in choosing sensible initial parameters or narrowing the scope of the search, as well as knowing which algorithm to choose. A common choice is simulated annealing, where the initial "high temperature" of the system can enable the parameter search to get itself out of local optima, and continue on to the global optimum. Other options such as Bayesian modelling and parameter inference may provide a solution to some models in systems biology (Pullen and Morris 2014).

Chapter 3

Quantifying the PEN3 Response

3.1 Introduction

Fungal and oomycete pathogens which aim to penetrate the cell wall through the use of degrading enzymes and physical force trigger the initial immune response: PAMP triggered immunity (PTI). This response generates many downstream penetration defence mechanisms, including upregulation of penetration defence genes (PEN). The roles of PEN1-PEN4 are discussed in detail in 1.5, and PEN3 is summarised below.

PEN3 encodes PDR8, an ATP binding cassette protein with homogeneous distribution in the plasma membrane (Stein 2006). When a penetration attempt has been detected, PEN3 recruitment is increased. This enables enrichment of PEN3 in the membrane proximal to the infection side, further aided by endocytic recycling of PEN3 from elsewhere in the membrane. This transport is made possible through the use of myosin motors trafficking these PEN3 endosomes along the actin cytoskeleton to the site of infection. Once in place, the role of PEN3 is to transport toxins and antimicrobials from the PEN2 metabolic pathway into the apoplast (Matern et al. 2019), which has been shown to contribute to *A. thaliana* resistance against a range of fungal and oomycete pathogens (Lipka et al. 2005; He et al. 2019).

This research aimed to develop a means of testing and quantifying the focal PEN3 trafficking responses to pathogens, through the use of an artificial penetration peg. Actin

depolymerising drugs, and *loss-of-function* mutants in actin nucleation were used to test the hypothesis that actin-driven trafficking delivers the PEN3 response.

3.2 Methods

3.2.1 Experimental Techniques

Arabidopsis thaliana ecotype Colombia-0 (Col-0) with PEN3-GFP were grown as the wild type, alongside loss-of-function mutations in Arp2 or three formin genes (Formins 4, 7 and 8); these are actin network nucleation regulators with stress-response phenotypes. *A. thaliana* seeds were sterilised with Cl_2 for 4-5 hours in a sealed container by mixing 100 ml of bleach with 3 ml of 37% HCl. Sterilised seeds were suspended in molecular biology grade water and stored in the dark at 3°C for a minimum of 5 days. To produce the extended hypocotyls, seeds were dark grown in a humid growth chamber at 21°C for 5 days. 100 µl half-concentration Murashige and Skoog (MS) growth medium with Gamborg's Vitamins containing 0.8% w/v agar was used as the growth medium, upon which the seeds were placed. 500 µl centrifuge tubes were used to contain the medium and support the hypocotyls.

We have developed a novel technique for artificial stimulation of the plant immune response. In order to simulate the physical pressure of a fungal or oomycete penetration attempt, custom cover slips were fabricated to contain microdiamonds on their surface which contacts the sample. Initially, standard glass (0.13-0.17 µm) cover slips were cleaned with a 5-minute acetone bath followed by an additional 5 minutes in isopropanol (IPA) before being dried with compressed nitrogen gas. Clean cover slips were coated in poly-methyl methacrylate (PMMA: 950k, A6) using a spinner at 3000 rpm for 55 seconds to create an even 500nm layer. A microdiamond suspension using IPA (0.14 mg ml^{-1}) was dropped onto the coated cover slip and left to bake on a hot plate at 165°C for 10 minutes. This caused the PMMA layer to plasticise and fix the diamonds to the surface while the IPA solution evaporated away. To ensure the diamonds protruded sufficiently from the surface, a profiler was used to record the surface height and is shown in Fig. 3.1.

To simulate the chemical stimuli presented by the invading pathogen, *A. thaliana*

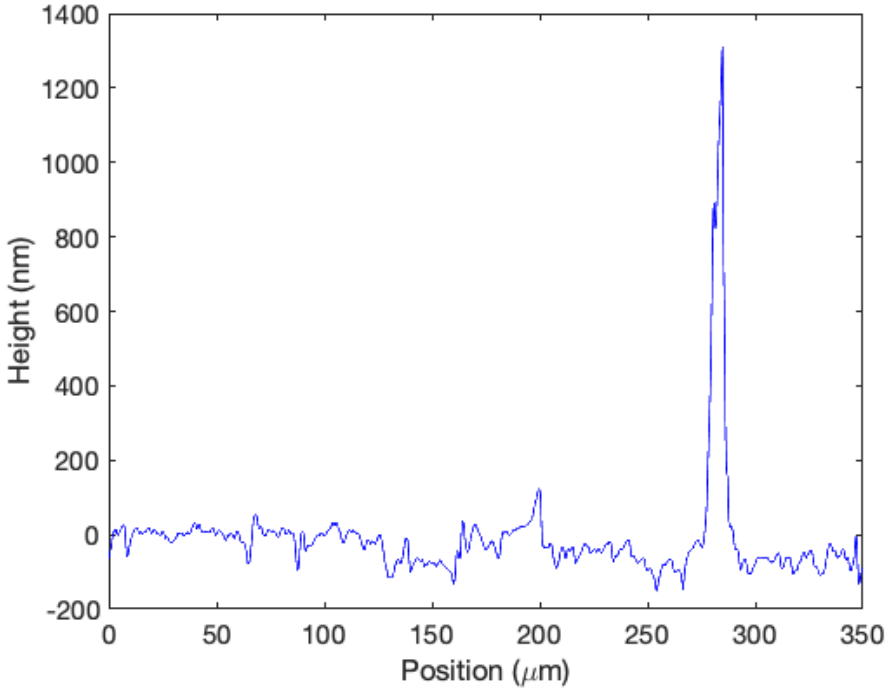

Figure 3.1: Cover Slip Surface: A typical diamond embedded in the PMMA layer of the custom cover slip is shown to protrude from the surface by a little over 1 µm. The system was designed to accurately measure the change in height, while position resolution was limited, so the ~10 µm width is likely less in reality, based upon visual inspection on various microscopes.

hypocotyls were submerged in a molecular pattern for four hours prior to physical stimulation and imaging. The aim of this was to upregulate PEN3 production and improve both response time and intensity to aid in data collections (Sassmann et al. 2018). This elicitation medium was prepared with 0.004% w/v driselase and 100 µg ml^{-1} of chitin granules. A chitinase suspension was added to activate the solution, containing 400 µl of 100 mM sodium phosphate (pH 6.1) and 400 µl glycerol to achieve a 0.05 mg µl^{-1} solution. In order to test the hypothesis that the actin cytoskeleton is vital in the role of the in PEN3 delivery, actin was depolyermised using 10 µM Latrunculin B diluted from a 10 mM stock in DMSO. A mock DMSO solution was also prepared as a control, with these solutions being added to the molecular pattern submerged hypocotyls 30 minutes prior to imaging.

A. thaliana hypocotyls were mounted on the custom cover slips with a mounting medium which contained 10% molecular pattern (as described above) and a 10 mM MES buffer at pH 7.5 to keep a consistent elicitation. The microscope slide was outlined with a layer of petroleum jelly to provide a water-tight seal when the cover slip and slide were taped together. When mounted on the spinning-disc microscope with an oil-immersion

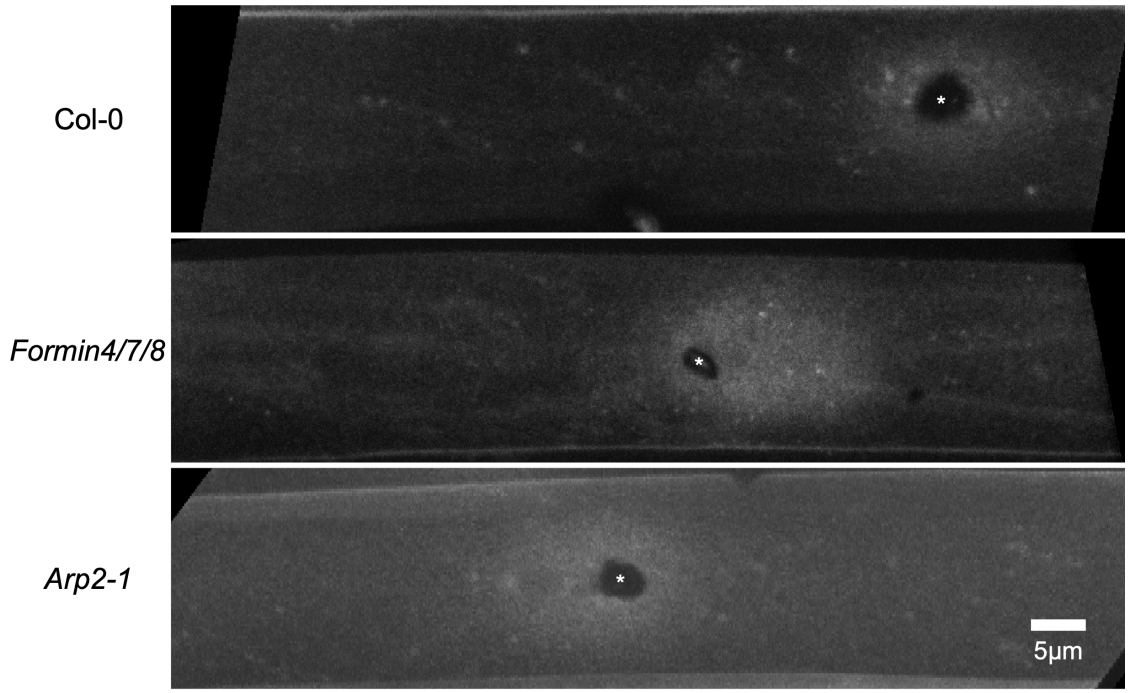

Figure 3.2: Artificially triggered immune responses. *A. thaliana* hypocotyl epidermal cells show enrichment of PEN3-GFP in a local region around the point of physical simulation (using our novel microdiamond assay, marked with an asterisk), 20 minutes after first contact. These images show the relative homogeneity of the background PEN3 distributions, as well as some bright PEN3 endosomes just below the membrane. The images are from a spinning disc confocal microscope, maximally projected from stacks with 0.55 µm separation and a 200 ms exposure.

60x lens (1.35 NA), the focal plane was adjusted to bring the xylem into focus before being reset back to the surface of the epidermal cells. The pressure from the lens movement was to provide the initial 'punch' in order to mimic a fungal pathogen, and is the point at which the timer was started. Z-Stacks (16 images, 0.55 µm separation, 200 ms exposure with 7 mW laser power at 488 nm) were taken 20 minutes after the punch. For the following 60 seconds, the stage was moved such that multiple images could be tiled together in order to provide a bigger picture of the response throughout a cell, as well as to significantly increase throughput. An image of each genotype responding locally to the physical stimulus is shown in Fig. 3.2.

3.2.2 Computational Analysis

All image stacks were projected into a single image: For every point in the x-y plane, each image in the stack was checked, and the highest value pixel was kept. This is done so that only pixels that were most in focus were kept, and any issues with non-flat surfaces were mitigated. A mask was drawn by hand around the cell of interest for every image,

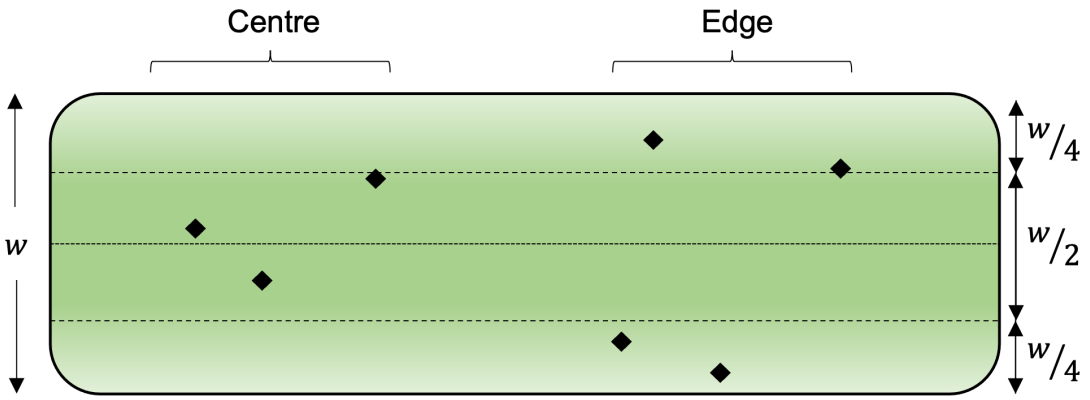

Figure 3.3: Determining Which Diamonds to Compare: The curved surface of hypocotyl epidermal cells means that the pressure exerted by the cover slip in the centre of the cell is greater than near the edge, and so this has to be controlled for. Any diamond whose centre is closer to the centre-line of the cell than the edge of the cell is categorised as in the centre. If the diamond centre is closer to the edge, it is categorised as on the edge. If any of the diamond footprint is outside of the cell, it is categorised as being in the cleft between cells.

and an additional mask was drawn around the microdiamond. The diamond mask was used to exclude the region from intensity measurements as it scatters the light significantly resulting in a darker region, which can been seen in Fig. 3.2, as well as providing information about the centre point from which to search for increased PEN3-GFP signal. Due to the curvature of the epithelial hypocotyl cells, which are normally approximately cylindrical, only diamonds in the centre of the cell width were considered. When sandwiched between the slide and cover slip, the centre of the cells makes good contact, but the curvature means that pressure is reduced near the cell edges, reducing the chances of an immune response from a physical stimulus. This method behind position categorisation is explained further in Fig 3.3.

To determine whether the cell had responded to the stimulus provided by the diamond, the local region around the diamond was compared to a background measurement of the cell intensity. A circle was drawn around the diamond, centred on the centroid of the diamond mask, with a radius of 50 pixels (4.75 μm). This radius was chosen based upon initial, by-hand, estimates of some PEN3 responses. It was made slightly smaller than the measurements to reduce the chance of false positives, as a few bright pixels averaged over the whole cell has a much less significant effect than a few dark pixels in the circle region of interest (ROI). If the circle ROI would extend outside of the cell mask, it

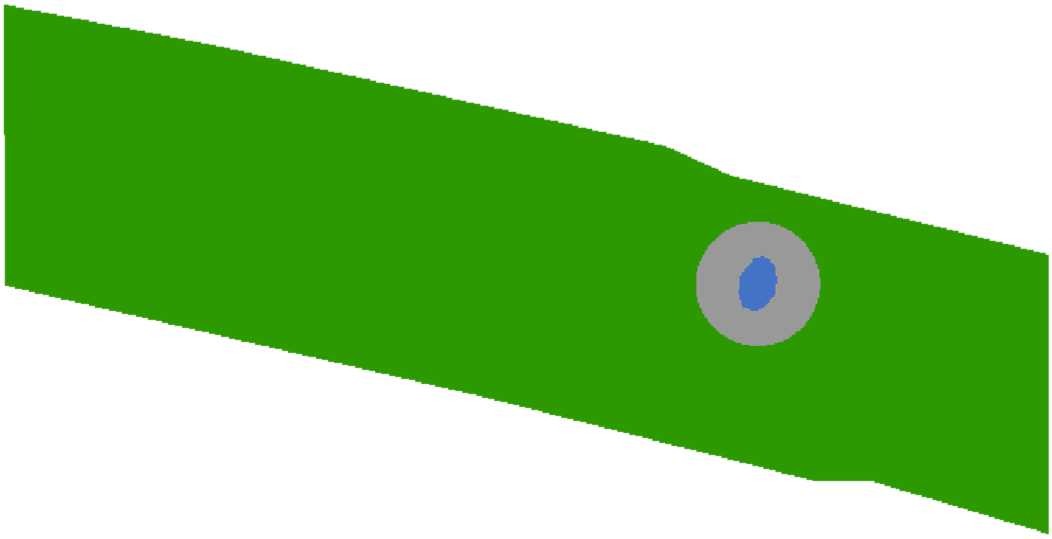

Figure 3.4: Determining a PEN3 Response: The cell background is measured in the green region, which is the cell mask minus the diamond mask (in blue) and the 50 pixel radius ROI (in grey) centred around the diamond. An immune response has been deemed to have occurred if the mean intensity of the grey region is brighter than 75% of the green region. These masks are from one of the images used in this data set.

was cropped to match the edge of the cell, and the diamond mask was also removed from the ROI due to it scattering the light from the PEN3-GFP. The various regions are depicted in Fig. 3.4. If the mean of the circle ROI was greater than the 75^{th} percentile of the background cell, the diamond was deemed to have induced an immune response. The 75^{th} percentile was chosen through visual inspection of multiple cells.

As the immune response frequency is a binomial distribution, the response frequency p was calculated as the number of detected immune responses divided by the total number of sites imaged N. Assuming this response frequency is equal to the response probability for a given genotype, the probability of getting k immune responses from N sites is given by,

$$P(k) = \frac{N!}{(N-k)!} p^k (1-p)^{N-k}. \tag{3.1}$$

Sampling N times from this probability distribution with a pseudo-random number generator (pRNG) produced a continuous variable output estimating the distribution of response frequencies for each genotype, each with its own value of N and p.

For the cells that were determined to have initiated an immune response, the size of the PEN3 disk was measured. First, to remove some of the background noise and correct any uneven illumination, the morphological opening of the image with a 35 pixel

radius disk was subtracted from the image. Next, to remove any salt and pepper noise still present, a median filter was applied to the image. From here, the 80^{th} percentile of the cell mask minus the diamond mask (leaving the green *and* grey regions in Fig 3.4) was measured and used as a threshold to create a binary image. This value was chosen to be suitable for rejecting objects which were not of interest, while still correctly identifying the PEN3 response in terms of position and size. Despite the filtering process, it was possible that several binary objects would be present. To pick the one that represented the PEN3 response, the objects were labelled and the labelled object which overlapped with the diamond mask was kept as the PEN3 response. An ellipse which encompassed this chosen binary object was fitted and its properties were measured: major (r_{maj}) and minor (r_{min}) axis size, orientation and position. The orientation of the cell mask was also measured such that the angle of the response relative to the cell could be determined. The eccentricity ϵ of the ellipse was determined from the radii using,

$$\epsilon = \sqrt{1 - \left(\frac{r_{\text{min}}}{r_{\text{maj}}}\right)^2}, \tag{3.2}$$

with $r_{\text{maj}} \geq r_{\text{min}}$, and the relationship is shown in Fig. 3.5. The effective radius $\bar{r}$ is defined as the radius of a circle with the same area as the ellipse, and is calculated by taking the geometric mean of r_{maj} and r_{min} such that,

$$\bar{r} = \sqrt{r_{\text{maj}} r_{\text{min}}}. \tag{3.3}$$

Finally, a visual inspection was performed on every result to ensure no problems had arisen.

3.3 Results

The response frequency, defined as the number of artificial infection sites which had a visible PEN3 enrichment patch divided by the total number of sites, is shown in Fig. 3.6A. Just under 68% of the 28 infection sites had a visible response in the wildtype while 79% of the 24 *arp2-1* sites responded. Nearly 83% of the 41 *formin4/7/8* triple mutant sites showed an immune response 20 minutes after the diamond made contact, significantly higher than

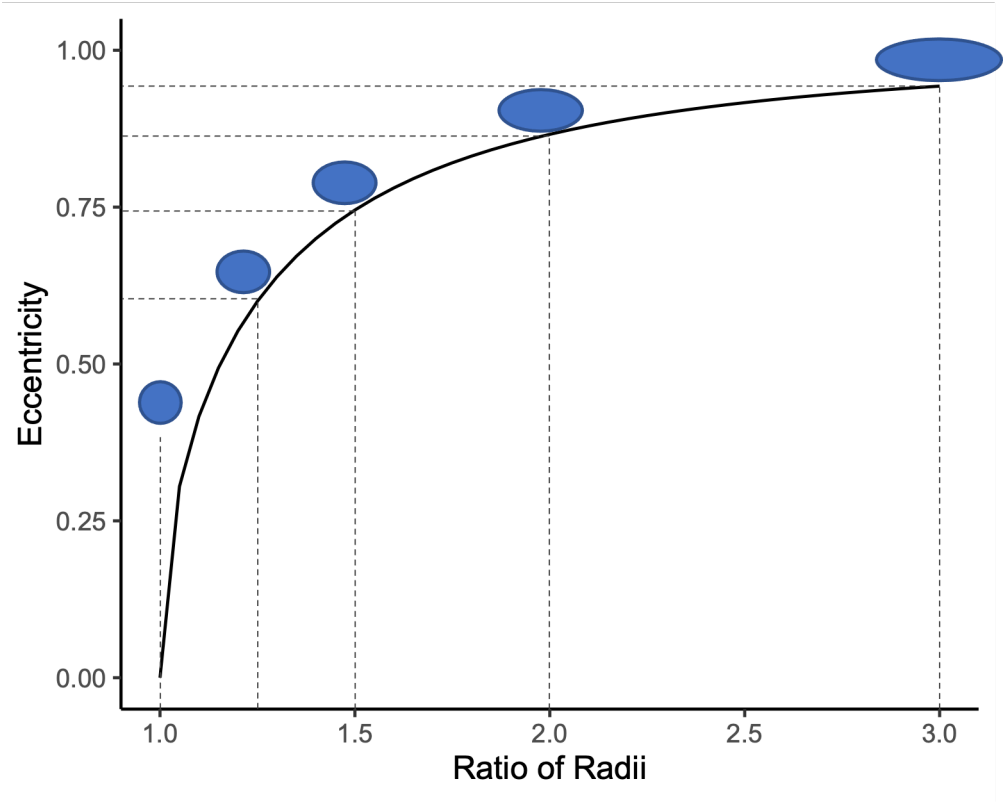

Figure 3.5: Eccentricity of an Ellipse: A visual depiction of the eccentricity of an ellipse highlights that objects still look fairly circular until eccentricity reaches close to 0.75, as the ratio between the radii (r_{maj}/r_{min}) becomes greater than 1.5.

the wildtype (Chi-squared test, p = 0.0388). This may be explained by a link between actin mutants and elevated systemic acquired resistance in a possible feedback loop with the salicylic acid pathway (Matoušková et al. 2014; Kalachova et al. 2020). The *arp2-1* appeared to have a slightly higher occurrence of dead or dying cells compared to the *formin4/7/8*, which combined with the randomness of the diamond locations on the cover slips resulted in the *arp2-1* mutant having a smaller sample size. While this had a small effect on the Chi-squared test, it is not the reason significant differences between wildtype and *arp2-1* were not found. Preliminary testing was also done on diamonds which fell into the edge of cleft categories, but the response frequency was very low and therefore no differences could be found. This, alongside difficulties of measuring a response size and shape when it is confined by the cell shape, is the reason that only central diamonds were considered for any ellipse fitting and response measurements. Statistical testing the response frequency was performed using the original binary data, instead of the output sampled from their binomial distribution which is shown in Fig. 3.6. This is because the assumption that the

measured outcome probability is completely biologically accurate is unlikely to hold, and that probability was used as fact to generate the binomial distribution, therefore drawing statistical conclusions from an uncertain assumption would not be robust.

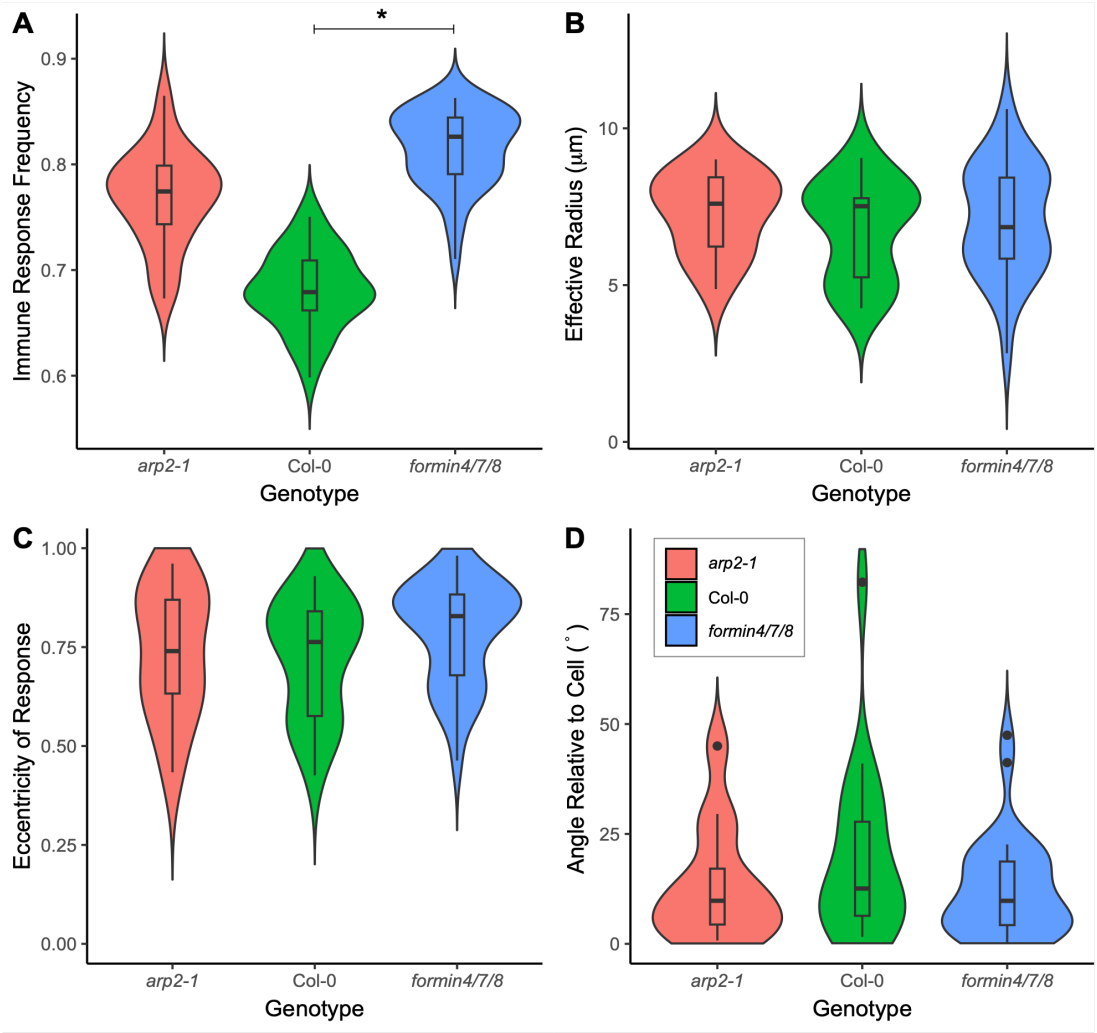

Figure 3.6: Artificial Stimulation of the Immune Response. The accumulation of PEN3 in the membrane of *A. thaliana* hypocotyl epidermal cells was imaged 20 minutes after the physical stimulus of the microdiamond was applied and this response was quantified in a range of ways. Wildtype (Col-0) was compared to loss-of-function mutants of *arp2-1* and *formin4/7/8* and a treatment of Latrunculin B for actin cytoskeleton depolymerissation. Samples sizes from wildtype, *arp2-1* and *formin4/7/8* were 28, 24, and 41 respectively. (A) The fraction of diamond sites which had a measurable PEN3 response 20 minutes after diamond contact, estimated from a binomial distribution with probability equal to the fraction of PEN3 responses. (B) The geometric mean of the major and minor axis radii, which yields the correct area using the formula for area of a circle. (C) The eccentricity of the response regions, calculated using Eq. 3.2. (D) The angle of the major axis of the response ellipse relative to the long axis of the hypocotyl epidermal cell, in the range [0,90].Statistical testing of (A) was performed using a Chi-Squared test on the original binary data set, where the asterisk denotes $p < 0.05$. ANOVA testing of (B)-(D) was performed and yielded no significance.

The effective radius of the PEN3 response, calculated from fitting an ellipse to the image and using Eq. 3.3, is shown in Fig. 3.6B. The size of the response regions was consistent between the genotypes, with a radius of 6.8 ± 1.6 μm for the wildtype, 7.3 ± 1.3 μm for

the *arp2-1* mutant and 7.1 ± 1.8 μm for *formin4/7/8*. No significant differences were found in the eccentricity of the response, shown in Fig. 3.6C. The mean eccentricity ranged from 0.72 ± 0.15 in the wildtype to 0.74 ± 0.17 in the *arp2-1* and 0.79 ± 0.13 in the *formin4/7/8* triple mutant.

All the immune responses were elliptical and most had their major axis aligned with the long axis of the hypocotyl epidermal cells, as shown in Fig. 3.6D. This may be due to the polarity of cytoplasmic streaming and the direction of travel of PEN3 vesicles, as the cytoskeleton also tends to align with the long axis of the cell. To emphasise the critical role of the underlying cytoskeleton in the role of PEN3 transport, the network was depolymerised using Latrunculin, and not a single infection site showed an immune response. Despite the possible impact of the loss-of-function mutants on the cytoskeleton, the immune response sites remained relatively unchanged. Even the *formin4/7/8* triple mutant, with its increased sensitivity and immune response frequency, had very similar response properties, showing the resiliency of the initial stages of the immune response and possibly the actin cytoskeleton.

3.4 Discussion

The measured outputs of the script were visually inspected to ensure any suspect data was flagged and removed. Occasionally, either the entire cell edge had accumulated PEN3 (more frequent in the mutants as might be expected, and can be seen in panel (d) of Fig. 3.7) or the cytoplasmic stream was very bright and running through the middle of the enriched zone, shown in panel (c) of Fig. 3.7. This meant that any thresholding was likely to include these regions when they were not relevant to the size, shape or orientation measurements we were interested in. Any such cases were flagged and in the case of this analysis had been removed from all results except frequency of response. I am confident that these do have a response, but additional noise and signal has made automating the extraction of the region impossible. Manual segmentation of these images could be performed the extra data or power was required for the experiments, but these were excluded to minimise bias in this case. Only 10-15% of all responses suffer from this problem, while most of the time the fitting works as intended, as shown in panels (a) and (b) of Fig. 3.7.

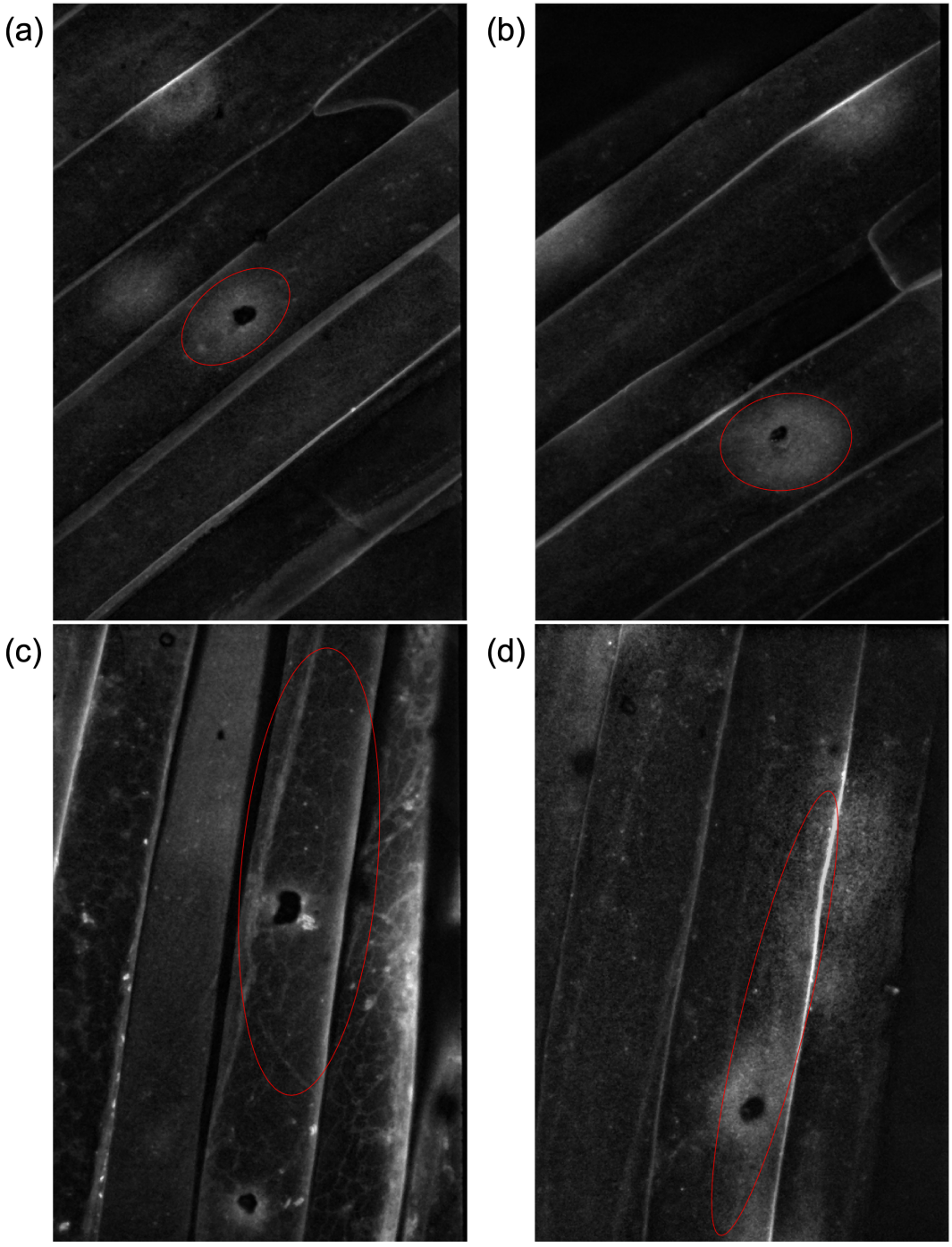

Figure 3.7: Ellipse Fitting Issues: A visual inspection was performed on each ellipse fitting to the PEN3 response, and erroneous fits were excluded from the analysis. (a) shows a correctly fit ellipse of an immune response which is aligned with the long axis of the cell. (b) also shows a correct ellipse fitting, but the response orientation is slightly off-axis. (c) shows an example of a small immune response which is tangential to a bright cytoplasmic stream. As the response is no brighter than the stream and the two objects are touching, creating a single binary object, the thresholding cannot separate them, resulting in erroneous fitting. This result is omitted from the immune response properties that have been reported. (d) shows a case where increased cell sensitivity and possible cell wall damage have resulting in PEN3 accumulation all along one edge of the cell, which overlaps with an immune response from a diamond. As the responses overlap, it is not possible to filter them out and separate them, resulting in an inaccurate fitting. This response has also been omitted.

Despite the differences in the response frequency of the wildtype relative to the *arp2-1* and *formin4/7/8* mutants, the similarity of the PEN3 distributions may point to these distributions being fundamental to the efficacy of the immune response. One possibility is that passive diffusion of PEN3 in the membrane is responsible for the consistency in response size. With a sufficient rate of diffusion, delivery could be highly localised to the central point of the infection. This would simplify the requirements of the underlying actin network while still providing fairly consistent PEN3 distributions, which may explain how the impaired actin mutants are so similar.

Another possibility is that the PEN3 distribution is chosen by design to be most effective for the given scenario. This could be achieved through the architecture of the actin patch, tightly controlling delivery of the PEN3 vesicles, or it could be done via a chemical signalling region for the delivery of these vesicles. It has been shown that a ROS burst can be detected within minutes of the cell being treated with a microbial elicitor (Sang and Macho 2017), and that apoplastic ROS regulates localised callose deposition (Daudi et al. 2012), which is likely regulated through actin remodelling - an outcome of the pattern-triggered ROS burst (Li et al. 2015; Li et al. 2017). Activation of RBOHD, which can generate these ROS bursts, relies on the activation of several calcium-dependent protein kinases (CPKs) (Boudsocq et al. 2010) through a rapid increase in the local Ca^{2+} concentration, also triggered from pattern-recognition. Many of these proteins are critical in the immune response, as mutations in RBOHD lead to a near complete loss in pattern-triggered ROS (Qi et al. 2017), likely affecting the signalling systems of salicylic acid and cytosolic Ca^{2+}. Any of the molecules in this signalling cascade could be responsible for controlling the size and/or shape of the PEN3 enrichment region. As ROS have been proposed to act as local or secondary messengers which can trigger additional immune response functions (Kadota et al. 2015) the use of a ROS biosensor alongside PEN3-GFP could provide useful insight here. Alongside this, a calcium biosensor should be tested due to the ubiquity of Ca^{2+} in plant cell signalling.

3.5 Conclusion

We developed a novel method for separating the physical and chemical stimuli of an immune response, and used this method to consistently measure the PEN3 accumulation of a focal immune response. Images were taken 20 minutes after the microdiamonds made forceful contact with the *A. thaliana* hypocotyl epidermal cells, and image analysis software I developed was used to determine whether an immune response has occurred, as well as quantifying the size and shape of the response.

We saw a statistically significant increase in the frequency that a response occurred in the *formin4/7/8* loss-of-function mutant relative to the wildtype, whereas the *arp2-1* mutant showed no measurable difference. For the measured responses in the wildtype and both of the mutants, no differences were seen in their size (through their effective radius), nor the eccentricity of the response, or the alignment of that response relative to the long axis of the cell. We discussed whether the lack of differences here are down to the response shape being a size effect of diffusion, or whether one of the many signalling chemicals vital to the focal immune response play a role in designating the delivery zone.

Actin depolymerisation using Latrunculin B showed that actin is critical for the immune response, despite the actin mutants showing no reduction in immune competency. The fact that the statistical difference was not biologically relevant suggested that the system is very robust. It is therefore possible that actin nucleation doesn't contribute directly to this early stage of the response, and instead global, cell-wide PEN3 transport on actin is more important that local dynamics in this case.

Chapter 4

Image Analysis: Testing and Development

4.1 Introduction

The role of actin in plant cells was introduced in 1.6, and the importance of the cytoskeleton in plant function and immunity cannot be overstated. Being able to extract spatial networks composed of one-dimensional structures, from road networks to sub-cellular biological filaments, is a recurring theme throughout many research areas. Nowhere is this more important than for the cytoskeleton, where resolution-limited imaging data can make network extraction extremely difficult. In addition, this problem is by far the most acute for actin, the narrowest element of the cytoskeleton, which is ubiquitous throughout eukaryotic cells.

This research aimed to design, create, test and validate a tool which is able to extract and quantify the cytoskeletal network from microscopy images. This tool needed to be simple, fast and fairly robust, while enabling a more detailed picture and understanding than was previously available from other tools in the area.

4.1.1 Analysing the Actin Network Structure

Being able to observe and quantitatively measure the structure of the cytoskeleton is important for understanding wild-type behaviour, mutant phenotypes, the effect of drug treatments, and the cellular response to external stimuli such as pathogen attack. The fact that the cytoskeleton is highly adaptive and versatile, rapidly responding to changes when required, only makes this task more difficult, not least because some small perturbations (such as HopW1 from *Pseudomonas syringe* (Kang et al. 2014)) are able to cripple the entire network and, by extension, the cell itself.

Typically, progress in this area requires significant amounts of data. This has become increasingly viable due to the development of genetically encoded probes (*e.g.* GFP-Lifeact and GFP-Fimbrin) which can be used across a range of imaging modalities to give significant insight into the actin network structure and its turnover. Analysing such large datasets by hand is undesirable for at least three reasons: subconscious bias can skew results, human error is hard to avoid, and the time required can be prohibitive. What is needed instead is a consistent, automatic, reproducible, objective method that can quickly and quantitatively analyse network changes.

The constant remodelling and treadmilling of the actin cytoskeleton poses a problem for any analysis method. Live-cell imaging can be limited by exposure times that lead to motion-blur of highly dynamic features. Cell fixation methods can alleviate this, but only give a single snapshot in time and are prone to artefacts from the fixation process. Modalities ideal for capturing highly dynamic actin networks such as Total Internal Reflection (TIRF) microscopy can be limited in their ability to capture the complete three-dimensional network. This can be better achieved by forms of confocal microscopy, but here too there can be limitations such as poor Z resolution. No imaging system will be able to perfectly capture every detail of the actin network, which makes maximising the information available from current methods a priority. The algorithm we develop here is a step towards achieving this.

4.1.2 Previous Work in this Direction

The importance of the cytoskeleton across many areas of cell biology has resulted in significant interest in automatic methods that enable visualisation and extraction of the network. We review those that are most relevant to our work here. For a recent review that summarises many of these tools and the different methods they employ, see Özdemir and Reski 2021.

One of the most common methods utilised for cytoskeletal extraction is based on open active contour models (Xu et al. 2011; Li et al. 2009a; Li et al. 2009b). These examine changes in the intensity gradient of an image in order to find ridges, which form the backbone of actin filaments. These backbones (often called "snakes") are defined in terms of the energy of their contour, which is minimised in the gradient field in order to generate the filament segmentation. This process can be computationally expensive depending on the number of iterations required to achieve accuracy, but the results tend to be impressive in terms of accuracy (precision and recall) (Xu et al. 2019). Several tools are available which use these models, including imageJ plugins like JFilament (Smith et al. 2010) and standalone programs such as SOAX (Xu et al. 2015) and TSOAX (Xu et al. 2019). Depending on the implementation, one drawback of these methods is that they often require significant human input to aid in the labelling of filaments and discern crossings. This has to be done separately for each image, which diminishes the utility of automatic methods. The more automated methods, such as SOAX, provide the option for batch processing and therefore require reduced input from start to finish. The number and sensitivity of the input parameters, however, make it difficult to achieve consistently accurate results across a variety of images, cell types and scenarios. While the input parameters can be adjusted on a per-image bases, this may interfere with the validity of any comparisons and could introduce bias into the results.

A complementary approach, based on the molecular mechanisms that govern actin network formation and dynamics, was developed by Schaub et al., and involves simulating the network itself and comparing the output to experimental images to determine the network properties (Schaub et al. 2007). Comparison between simulation results and experiments required knowledge of the imaging system point spread function, the reso-

lution of the charge-coupled device (CCD), any non-uniform responses from pixels, and the magnification and numerical aperture (NA) of the lens. These methods were able give a good estimate of the underlying network, but only under the assumption that the simulation correctly captures the true underlying network dynamics. At present, with current knowledge of actin biophysics, this may not be the case. Further, fitting a many-parameter simulation to experimental data can both be time consuming and experience problems of model identifiability (where significantly different parameter values lead to similar network structures).

Several approaches have been developed for other imaging modalities, as well as software designed to identify other structures linked to the cytoskeleton. CellArchitect (Faulkner et al. 2017) is a tool designed to extract automatically plant microtubule data from large quantities of confocal microscopy data using Gaussian filters and local thresholding to segment the network from the background. From here, two-dimensional measures such as length, density and width can be extracted. SIFNE (Zhang et al. 2017) is a tool designed to extract simple quantitative data (such as filament length and density) from the microtubule array imaged with single-molecule-localisation microscopy. ANNA-PALM (Strack 2018) is another super-resolution-based tool that can reconstruct microtubule arrays, either via PALM or DNA-PAINT microscopy (Ouyang et al. 2018). BundleTrac (Sazzed et al. 2018) and Actin Segmentation (Rigort et al. 2012) both extract the network of actin filaments from Cryo-Electron Tomography images. BundleTrac requires manual input of "seed points" to start filament identificiation, while Actin Segmentation is fully automated with analysis of the resulting networks yielding measurements of filament lengths, orientations and densities. Finally, FIESTA (Ruhnow et al. 2011) and TipTracker (Prahl et al. 2014) use epifluorescence microscopy to locate microtubules, with the former being shown to also work with TIRF microscopy (as does MTrack (Kapoor et al. 2019)).

Segmentation and analysis can be extended to additional biopolymers such as the endoplasmic reticulum. The MATLAB software AnalyzER (Pain et al. 2019) takes fluorescent labelled ER images from a confocal microscope (up to multi-channel 4D time-series data), enhances the tubular structures and then performs segmentation and skeletonisa-

tion. The skeleton is converted to a graph representation with nodes at junctions (containing data such as degree and branch angles) connected by edges (which also described length and average width). This approach was able to quantify the effects on the morphology of the ER under different drug treatments and abiotic stresses.

Depending on the assay, biopolymer of interest and imaging requirements, there are a range of techniques tested and available (Özdemir et al. 2018; Xia et al. 2019; Hadjidemetriou et al. 2008; Tsugawa et al. 2016; Park 2020; Nanguneri et al. 2019; Lavoie-Cardinal et al. 2020). However, most of these solutions are tailored to specific forms of biological network and research questions, consequently they do not integrate a broad categorisation or quantification of individual network properties.

4.2 Results

4.2.1 Algorithm Development

Using an initial set of 20 images of GFP-Lifeact (Smertenko et al. 2010) labelled actin in wild-type *A. thaliana* (obtained as described in the Methods), we first developed our algorithm for automatically extracting the actin skeleton from either a single 2D image or a 3D stack of images. We decided to base this in MATLAB due to the power of the image processing toolbox. MATLAB also has excellent backwards as well as forwards compatibility, ensuring easy adoption both by users with older versions and by future users with as yet unreleased versions.

Our algorithm follows five sequential steps (see Methods and the Supporting Information for full details): initial preparation, skeletonisation, image rotation, skeleton labelling and property measuring. We discuss the first four steps here, leaving the last for the next subsection.

For the first image preparation step, the images were filtered to reduce noise and eliminate uneven background illumination. Any filtering process will result in the loss of information, but is necessary to facilitate extraction of the true actin signal. A range of filters and algorithms were tested, each with a range of parameters, in order to determine the most suitable option. Best results were found by using a top-hat filter with a spherical

structuring element. A top hat filter subtracts the morphological opening (an erosion followed by a dilation) of the image from the original image. This is similar to the rolling ball background filter in ImageJ, a commonly-used approach to analyse biological images. This aids in noise removal as well as correcting non-uniform illumination. A radius much larger than the width of the thickest filament was found to be suitable (between 2 to 3 times the width), otherwise filament signal may be removed or contrast at the edges may be lost. A Gaussian filter was also tested, but proved less successful as the filament edges were not preserved, making subsequent enhancements of tubular structures more difficult and measurements of thickness unreliable.

The second step was to convert the filtered image to a binary image of the skeletonised network, attempting to keep the filaments without any of the background. Simply applying a threshold to the raw image led to poor results (either struggling with detecting finer filaments or failing to adequately remove noise), so we first enhanced tubular structures using the MATLAB function *fibermetric* as shown in Fig. 4.1B. This works by calculating the Hessian of the image, determining its eigenvalues and searching for pixels with a small intensity change in one direction and a large change in the other (Frangi et al. 1998). Pixels satisfying this signify a tubular structure and so have their signal boosted. The benefit of this function is that it automatically adapts to various filament sizes, removing the need for any additional parameter tuning.

With the desired structures enhanced, we then created a binary image by using a threshold, shown in Fig. 4.1C. We tested both an adaptive and fixed threshold. For the adaptive threshold we used both the MATLAB default neighbourhood of around $1/8^{\text{th}}$ of the image size as well as smaller sizes. However, this failed to perform any better than a fixed threshold, while being significantly more computationally expensive and requiring an additional parameter. It is possible that by fine tuning the neighbourhood size and the sensitivity, an adaptive threshold will produce an improved binary for some data sets, but this would require specific tuning for each image, something that would compromise comparisons between images. We therefore decided to use a fixed threshold, with the threshold value determined as a specific percentile of the image intensity distribution. We believe this approach reduces the sensitivity of the threshold parameter, enabling it to

work better across multiple images and data sets, although it is worth noting that it is still the most sensitive parameter of our algorithm. A threshold intensity of between the 87^{th} and 92^{nd} percentile of the resultant image worked well in various scenarios, so we settled on 90% for the parameter value from this point forward.

Despite filtering and parameter tuning there was still some remaining noise in the binary image. It was possible to remove some of this, before skeletonisation, by deleting objects with an area below some critical value. This critical value strongly depends on the imaging conditions and modality, and so would likely need to be determined independently for each given dataset.

The final part of the second step was the skeletonisation itself. To do this, pixels were removed from the perimeter of all binary objects, through a medial axis transform (Lee et al. 1994), until removing more would have altered the topology or Euler number (the number of objects in an image minus the number of holes). This yielded a single-pixel-thick line that represents the backbone of the actin network.

The third step involved image rotation. To simplify downstream analysis, images were rotated such that the long axis of the cell (or ROI) was parallel to the horizontal axis of the image. The rotation angle was determined by fitting an ellipse around the image mask and calculating the orientation of its major axis. When rotating discrete pixels, some positional accuracy is inevitably lost. If the rotation is performed before the binary stage, then this can be remedied by using a smoothing algorithm. However, if performed after skeletonisation then, as with a Gaussian filter, this would smooth the edges we have tried to preserve. The best solution we found to this was to implement the rotation step both before and after skeletonisation, and then combine the two outputs via a pixel-wise OR, as shown by the parallel workflows of Fig. 4.1. If after this step any filaments were thicker than one pixel, they were skeletonised again.

The fourth step was to label the skeleton so that individual filaments were identified by distinct positive integers and is shown in Fig. 4.1E. This required significant testing and development in order to eliminate edge cases. The details of each step taken to achieve this are described in detail in the Supporting Information. In brief, to leverage the flood-fill

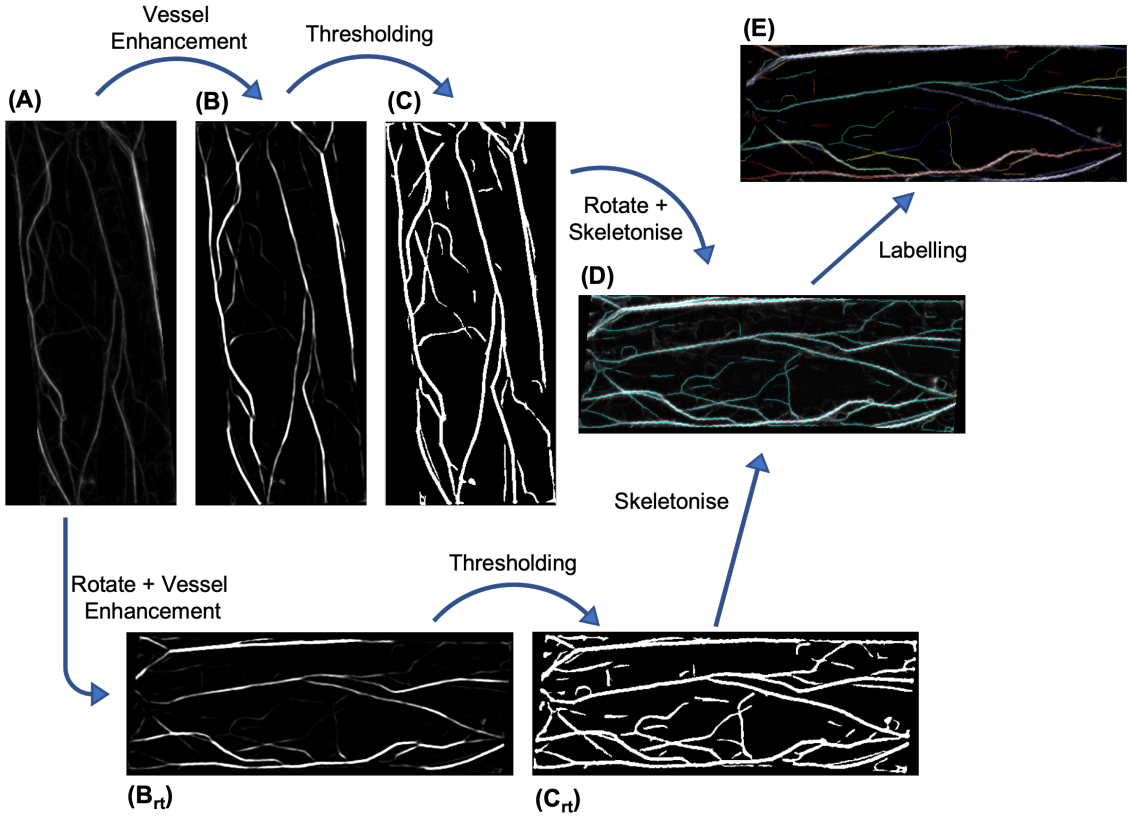

Figure 4.1: Skeletonisation Algorithm. Two parallel pathways are taken from the initial image (A) after background removal and filtering. The image had vessels enhanced (B) before thresholding into a binary image (C) before being skeletonised and rotated (D). Alongside this, the initial image was separately rotated before vessel enhancement (B_{rt}) and thresholding (C_{rt}) followed by skeletonisation (D). The skeleton results were combined to ensure no loss of information occurred in the rotation steps. From the combined skeleton, the labelling and relabelling processes were applied (E) to identify each filament and branch for further analysis

labelling algorithms in MATLAB, the filaments first had to be broken apart at every branch point so that branching filaments were given a different label ID to the main filament. It was found to be easier to also fragment the main filament in the process, and then rebuild and relabel afterwards. This was achieved by determining the labels around all (now removed) branch points, looking at the angles relative to each other, and rejoining the two that formed the straightest line.

4.2.2 Quantitative Measures

Once the actin skeleton had been extracted and correctly labelled, the fifth and final step involved extracting quantitative measures that described key properties of the network. It is these measures that can be used to characterise the actin cytoskeleton, providing a way of (i) understanding the underlying nature of the network and (ii) comparing different

image sets (*e.g.* across cell types, mutants or drug treatments) in order to determine if there are significant differences. Seventeen types of measure are defined for 3D data and these are summarised in Table 4.1 and Fig. 4.2, as well as being described in detail in the Supporting Information. These measures are split into five different categories: whole cell properties, overall network properties, individual filament properties, curvature and branching properties, each of which is described below. Additional measures can easily be added if required at a later date.

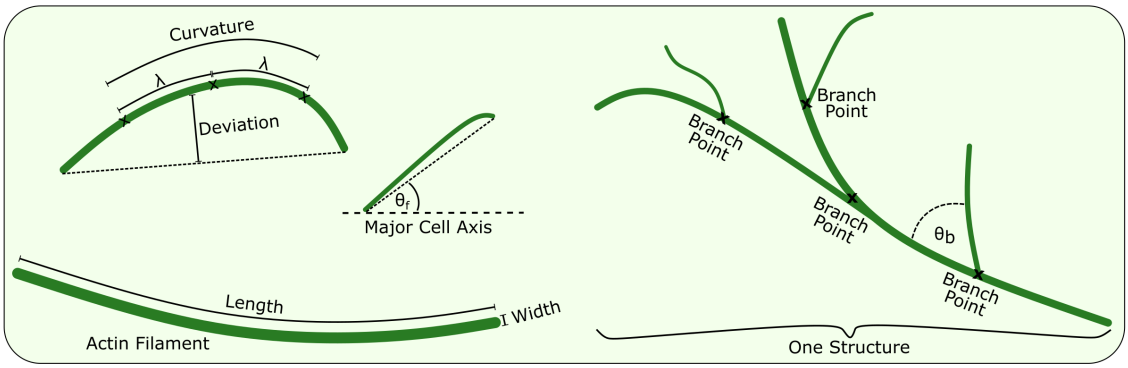

Figure 4.2: Network quantification. A visualisation of several of the measurements we are able to make in order to quantify the cytoskeletal network. The cell or ROI size was measured as the area encompassed by the black line of the outer bounding box and was used in the calculation of any densities, such as the skeleton or branch point density. The orientation was measured as the angle of that box relative to the horizontal axis prior to the rotation that ensured they were both in alignment. The curvature, both signed and unsigned, was averaged over the whole length of each filament and was measured as a series of three points separated by a characteristic length scale, λ. The deviation measured the average distance between a filament and a straight line connecting the end points. Filament widths were averaged over their whole length and filament orientation θ_f was measured relative to the major cell axis, and the same was done relative to the imaging plane to estimate the 3D filament length from a 2D projection. The branch angle θ_b was measured at every branch point, both in 2D and 3D. The branch ratio was simply the number of branch points divided by the number of labelled filaments. The total length of every structure was measured, such that statistics like the mean could be calculated.

Whole cell properties. The *cell size* is measured by counting the number of pixels in the ROI mask. This can then be used for density calculations in order to give quantities that are independent of the cell size. The *cell orientation* relative to the horizontal axis is measured by fitting the ROI to an ellipse and measuring the angle the ellipse makes to the horizontal axis. This measurement can then be used to align all cells to the horizontal axis to make further measurements more easily comparable.

Overall network properties. The *skeleton density* is measured as the total skeleton length in pixels divided by the cell area and can be used to highlight how tightly packed the network is. While many of the networks in our data sets were typically connected

to each other, new disconnected filaments and structures could form. To measure this, we calculate the number of these structures and the mean *structure size*. A significant change in this value may indicate, for example, disruption to severing activity. Network branching frequency is measured using the *branch ratio*, calculated as the average number of branches per labelled filament, while the *branch point density* is calculated as the total number of branch points divided by the ROI area.

Individual filament properties. We also calculate a range of filament descriptors, including orientation, length and width. *Filament width* is defined as the average width in pixels and will provide information about bundling activity. The *filament lengths in 2D* are measured by counting the number of pixels in the filament and adding $(\sqrt{2} - 1)$ for every diagonal connection, then converting from pixels to physical length. For *filament lengths in 3D* these lengths are then scaled by $\cos \theta_z$ where θ_z is the angle of displacement of the filament from the imaging plane. Changes in filament lengths may be indicative of growth, depolymerisation, or severing activity. The *filament angles in 2D* are obtained by calculating the angle relative to the horizontal axis of the line connecting the two filament end points. For *filament angles in 3D* the angle relative to the imaging plane is measured. The z-position of the filament end points is estimated by determining the position in the stack that contains the brightest pixel, which then allows the true angle to be measured. Finally, the *average filament length* is calculated as the mean of the 3D filament lengths.

Curvature properties. The curvature and non-linearity (deviation) of filaments are measured and represented by three different values. The curvature is measured over a fixed length scale λ in order to make the results independent of pixel size. For our data we chose $\lambda = 475$ nm, which is equivalent to five pixels. This is large enough that individual noise at the pixel level does not adversely affect the results, and small enough that the calculated value is a good estimate of the local curvature. Further, this value should work for a range of common imaging modalities and resolutions. For all non-end points in a filament, a point either side is chosen as close to λ away as possible. These three points then have their Menger curvature calculated. The *signed filament curvature* is the absolute value of the average of these curvatures (including their signs). The *unsigned filament curvature* is the mean of the magnitudes of the curvatures (ignoring their signs). The non-linearity

of the filament, referred to as the *deviation* from linear, was measured by calculating the absolute value of the mean distance between the filament and a straight line connecting the end points.

Branching properties. The *branch angles in 2D* are measured as the angle that a myosin motor would have to deviate to take the branch path instead of remaining on the main filament. This measurement is not calculated in the case that no branches are available. Finally, the *branch angles in 3D* is similar to the 2D measurement, but with the additional information of the z-position of the end points determined from the image stack. The distances between each pair of points are then calculated and used to determine the branch angle in 3D.

4.2.3 Algorithm Testing and Validation

Although testing the output of our algorithm against manual network segmentation gives some confidence that the algorithm can correctly extract the underlying actin network, it of course suffers from the problem that the human extraction may itself be faulty or biased. Rectifying this requires knowing the ground truth for a given network. To address this, we generated over 1,300 200x200 px artificial images where the locations and shapes of all filaments were known perfectly in advance. Individual filaments were generated by drawing a smoothing spline between two randomly generated points and their midpoint, which was shifted from the middle by a random amount to ensure a curve was formed. In order to accurately represent various filament thicknesses, each image dimension was scaled by a factor of 19, reducing pixel size from 95 nm^2 (the pixel size in our microscopy assay) to 5 nm^2 such that F-actin can be represented by a pixel-thick line. A Gaussian blur was then applied to match the diffraction limit of our of microscopy assay, before the image was downscaled back to 200x200 pixels by taking the mean of each 19x19 block of pixels. To adjust the signal-to-noise ratio (SNR), the filament brightness was scaled to a desired value, then salt and pepper noise added and randomly (via a uniform distribution) scaled up to a maximum parameter value depending on the SNR level that was targeted. Finally, a Gaussian blur matching the diffraction limit was applied to the noise before the image of the filaments and noise were combined, yielding a simulated microscopy image. Several

Category	Name	Type	Code	Description
Whole cell properties	Cell size	N	cellSize	Total number of pixels in the region of interest (ROI)
	Cell orientation	N	orientation	Angle in radians that the image is rotated by such that the long axis of the cell is parallel to the x axis
Overall network properties	Skeleton density	N	skelDensity	Number of pixels in the skeleton divided by cell size
	Structure size	L	Structures	Number of pixels in structures
	Branch ratio	N	branchRatio	The number of branch points divided by the number of filaments
	Branch point density	N	cellBPDensity	Number of branch points in the ROI divided by cell size
Individual filament properties	Filament width	L	filWidth	Average width of each filament
	Filament lengths in 2D	L	filLenXY	Length of each filament in 2D, accounting for angles and curvature
	Filament lengths in 3D	L	filLenXYZ	Length of each filament in 3D (the 2D length divided by the cosine of the filament angle relative to the imaging plane)
	Filament angles in 2D	L	filamentAng.angXY	Angle of each filament relative to the x-axis
	Filament angles in 3D	L	filamentAng.angZ	Angle of each filament relative to the confocal imaging plane; roughly estimated from endpoints and limited z-resolution
	Average filament length	N	avgLen	Mean of the 3D filament lengths
Curvature properties	Signed filament curvature	L	curvatureSigned	Average signed curvature of each filament, measured over length scale λ
	Unsigned filament curvature	L	curvature	Average unsigned curvature of each filament, measured over length scale λ
	Deviation	L	deviation	Average distance of each pixel in a filament from a straight line joining the endpoints
Branch properties	Branch angles in 2D	L	branchAng.angXY	Angle between main filament and a branch in 2D
	Branch angles in 3D	L	branchAng.angZ	Angle between main filament and a branch in 3D

Table 4.1: Quantitative network measures. The seventeen quantitative measures that we calculate for each extracted network,along with a description of each. Full details are given in the Supporting Information. N=single number, L=list of numbers.

of the parameters throughout these steps were varied in order to mimic changes in the quality of the data or differences. This allowed us to test the robustness of the network extraction process. For more detail of this process, see the Supporting Information.

In order to quantify algorithm performance, two metrics were used: sensitivity and precision. These are calculated using the frequencies of true positives (TP), true negatives (TN) and false negatives (FN). Sensitivity, also known as the true positive rate (TPR), describes the proportion of the network that is correctly detected and is given by TPR = TP/(TP + FN). Precision, also known as the positive predictive value (PPV), measures the positional accuracy of the identified network and is given by PPV = TP/(TP + FP). This showed the limitations of the algorithm in low quality data, resulting in significant drops in sensitivity. It also highlighted the trade off between sensitivity and precision that can be adjusted through the threshold parameter.

The same was repeated on real data using manual segmentation of the image for comparison and yielded a precision of 96% with a sensitivity of 72%.

First, by adjusting the maximum noise and filament brightness values, the signal-to-noise ratio (SNR) was varied. Because there is randomness associated with the image generation process, a range of SNR values correspond to a parameter set, and scaling between the parameters and SNR is non-linear. Three different noise levels were generated (each with 100 images), each containing 10 filaments (see Fig. 4.3A). Precision remained at or above 97% across the three SNR levels, while the sensitivity drops from 89% at an SNR average of 7.3 to 86% at an average SNR of 4.3. For the low SNR group (average of 3.4) the sensitivity drops significantly to 57% for an average SNR of 3.4, highlighting the point of limitation for the algorithm and the data. Although our algorithm was designed to attempt to try to keep both precision and sensitivity as high as possible, it is possible to optimise for one of these by adjusting the binary threshold and/or the minimum filament size as explained below.

Second, to test the effect of network density, a range of filament numbers (in a fixed size image) were considered. This noise value was chosen to be around the point where the algorithm performance changes rapidly, so that differences could be seen more easily.

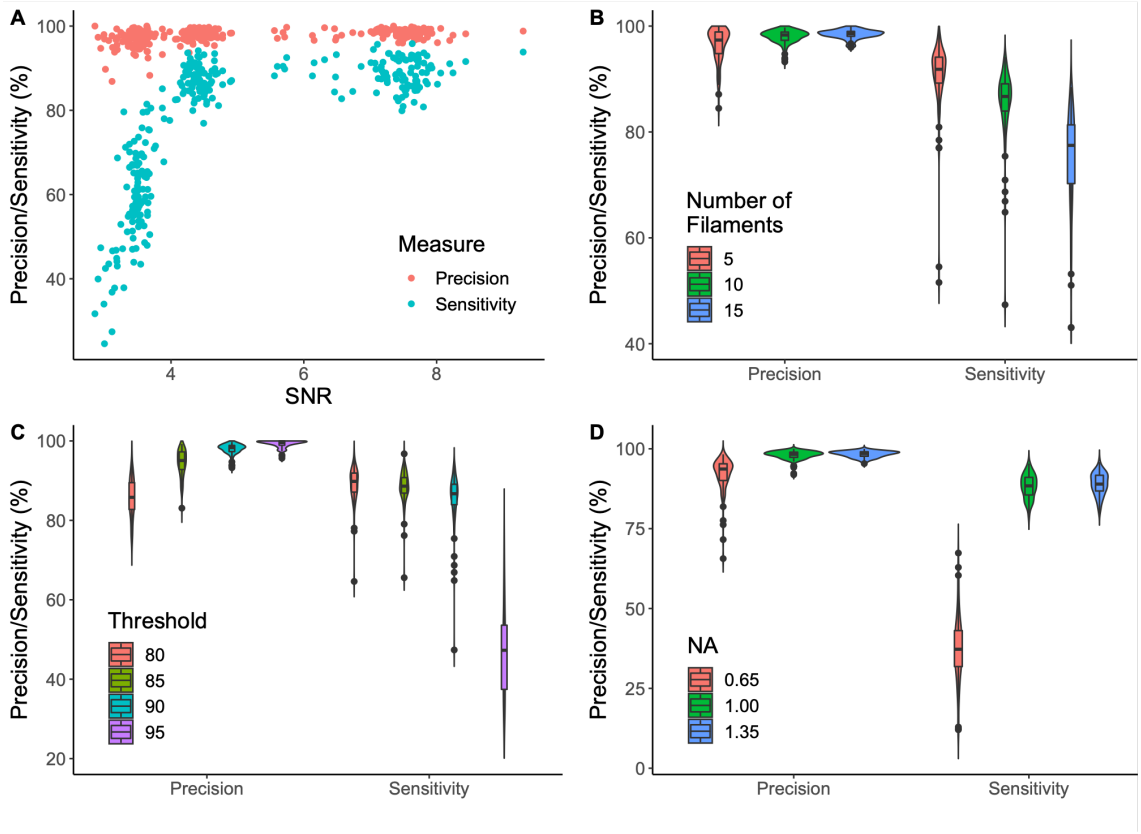

Figure 4.3: Testing network extraction performance. Artificially generated data was analysed with our algorithm and the results compared with the known ground truth. **(A)** To measure the effect of different signal-to-noise ratios, images were generated with three different levels of signal and noise intensities (100 each), showing that a critical SNR value of at least 4 is required to extract the most from the data in this assay. **(B)** To measure the effect of network density, images were generated with 5, 10 and 15 filaments (100 images for each), showing increased network density reduces sensitivity. **(C)** To explore the effect of the threshold parameter, four different threshold values were tested (100 images for each), highlighting the trade off between sensitivity and precision and that the optimal range is 87-92. **(D)** Finally, to investigate the effect of the numerical aperture (NA) of the lens, images were generated with a range of point-spread functions (100 for each), showing that even with high quality data, a minimum NA of 0.7-0.9 is required to achieve the resolution required.

As shown in Fig. 4.3B, increased network density leads to a drop in sensitivity while precision remains relatively unchanged. This is because of the high default threshold value, chosen to ensure minimal noise is measured for high quality data. While a reduction in the total number of filaments reduces the chances of filament crossover and close-proximity, it does not remove these possibilities, as can be seen for the precision outliers with only five filaments. A lower network density leads to a reduced network size and therefore any errors will constitute a larger percentage error.

Third, to measure the impact of the algorithm threshold parameter (the most sensitive parameter), this parameter value was varied from its default value of the 90th per-

centile of the intensity distribution of the image. The results, shown in Fig. 4.3C, highlight the trade off between sensitivity and precision. A higher threshold ensures greater precision, but at the cost of sensitivity. Conversely, dropping the threshold increases sensitivity, but beyond a point the precision falls and noise begins to adversely effect the output. Depending on the structures of interest, the resolution available and the experimental assay used, this value will need to be adjusted by the user to achieve the desired results.

Finally, to test the effect of the microscopy assay and resolution, the point spread function was varied to mimic various numerical apertures (NA) relevant to confocal microscopy. The results, shown in Fig. 4.3D, were tested using a high signal-to-noise ratio as all other tests were done on the point spread function mimicking the high NA lens setup, allowing the changes purely due to resolution to be clearly seen. For high quality data, we found a critical NA of 0.7-0.9, where the resolution becomes too poor and the sensitivity of the algorithm suddenly decreases. When designing and testing a microscopy assay, it is important to know where this limitation lies in order to ensure the extraction algorithm performs well. This may be particularly important for light-sheet microscopy where NA is limited by the physical configuration of the modality.

For high quality data, the sensitivity only drops when multiple filaments cross or are in close enough proximity that they begin to blur together and the tube-enhancing filter cannot distinguish them. The filaments here are drawn as 5 nm thick and then blurred to match the resolution of our microscopy assay. Any filaments that fall within about 200 nm of each other are likely to be nearly indistinguishable in accordance with the Rayleigh criterion. This also means that any crossings, even those that are completely perpendicular, are likely to be seen as globular instead of filamentous and may therefore drop below the threshold. In the cases where they do not, the lack of resolution and the skeletonisation process will represent the crossing poorly, typically appearing more as an 'h' or 'x-wing' shape (see SI for details).

In order to assess algorithm suitability to intermediate filaments and microtubules, we also tested the effect of filament thickness. We used supersampling to create filaments of width 5 nm (F-actin), 15 nm (intermediate filaments) and 25 nm (microtubules) and downscaled to fit a 95 nm^2 pixel size (which matches our microscope assay). No differ-

ences were found in the success metrics of our algorithm, as expected for objects significantly smaller than the available resolution. This demonstrates that our algorithm is likely to be easily adaptable to deal with other elements of the cytoskeleton.

4.3 Discussion

In this study we have developed a novel software algorithm, the DRAGoN tool, that can automatically extract and quantify multiple characteristics of complex actin networks, with particular focus on plant cells. Our software is designed to work with both 2D and 3D (*i.e.* stacks of 2D images used to estimate 3D structure) data. We have demonstrated its utility by establishing that it can accurately extract the large-scale actin structure for a range of cell types and mutants.

Our tool provides seventeen distinct quantitative measures of actin networks (see Table 4.1), including properties of the overall network (such as skeleton density and branch ratio), individual filament properties (such as filament widths, lengths, directions and curvatures) and branching properties (such as branch angles). The code can easily be extended to include additional measures as required by the user.

We validated our algorithm in a number of ways. This involved generating artificial networks (where the ground truth was perfectly known) consisting of individual filaments with various properties, including a number of edge cases. The length, curvature and deviation of these filaments were measured with the algorithm and shown to have high (>90%) precision and sensitivity with parameters corresponding to typical imaging modalities. This process was then repeated with various branch angles, again with similarly high detection rates.

To facilitate further development or optimisation for particular data sets, we have made the DRAGoN software freely available and open source: DRAGoN. The flexibility and non-specificity of this tool is one of its main advantages and should enable it to be useful in a range of organisms, mutants, tissues, cell types and environments. A number of key parameters (particularly those for the filtering and skeletonisation steps) can be adjusted to best fit a given image modality and labelling method.

4.4 Conclusion

The actin cytoskeleton is essential in eukaryotes, not least in the plant kingdom where it plays key roles in cell expansion, cell division, environmental responses and pathogen defence. Yet, the precise structure-function relationships of properties of the actin network in plants are still to be unravelled, including details of how the network configuration depends upon cell type, tissue type and developmental stage. Part of the problem lies in the difficulty of extracting high-quality, three-dimensional, quantitative measures of actin network features from microscopy data. To address this problem, we have developed DRAGoN, a novel image analysis algorithm that can automatically extract the actin network across a range of cell types, providing seventeen different quantitative measures that describe the network at a local level. This algorithm has been tested and benchmarked against both real and artificially generated such that its performance can be quantified and used to analyse new data.

4.5 Methods

4.5.1 Plant Growth and Imaging

Arabidopsis thaliana ecotype Colombia-0 (Col-0) with GFP-Lifeact were grown as the wild type. *A. thaliana* seeds were sterilised with Cl_2 for 4-5 hours in a sealed container by mixing 100 ml of bleach with 3 ml of 37% HCl. Sterilised seeds were suspended in molecular biology grade water and stored in the dark at 3°C for a minimum of 5 days. To produce the extended hypocotyls, seeds were dark grown in a humid growth chamber at 21°C for 5 days. 100 µl half-concentration Murashige and Skoog (MS) growth medium with Gamborg's Vitamins containing 0.8% w/v agar was used as the growth medium, upon which the seeds were placed. 500 µl centrifuge tubes were used to contain the medium and support the hypocotyls.

Images were taken with a spinning disc confocal microscope, equipped with a 60x lens and NA of 1.35. A laser power of 7 mW at a wavelength 488 nm was used for imaging GFP-Lifeact. Images were taken with 200 ms exposure and z-stacks had a separation of 0.55 µm.

4.5.2 Image Analysis Algorithm

We break our network extraction algorithm into a number of sequential stages—initial steps, skeletonisation, image rotation, skeleton labelling and measuring properties—which we discuss in turn. For full details of our method, see the Supporting Information section 4.6.

4.5.2.1 Initial steps

The initial step involves background filtering. While a Gaussian blur or median filter can smooth and modulate noise, they do not preserve edges (Zhang and Allebach 2007), which are critical in filament detection. Conversely certain non-linear techniques, such as the rolling ball algorithm, are able to preserve edges and features whilst removing noise and non-linear illumination (Cannistraci and Alessio 2016). Therefore, based on a rolling ball method, our raw images are first filtered to remove background noise and uneven illumination through a top-hat filter with a sphere shaped structuring element (via the *imtophat* function in MATLAB). The disk should be wider than the structures that must be preserved. However, since the algorithm time roughly scales with the square of the disk radius, there is a necessary balance between accuracy and speed. A radius of 15 pixels (approximately 1.4 μm in our images) was chosen as optimal for the actin structures we encountered.

4.5.2.2 Skeletonisation

The resultant image then has fibrous structures enhanced by using a Hessian-based multi-scale filter (via the *fibermetric* function in MATLAB). No thickness values were passed to this filter as actin bundles vary in thickness and we wish to preserve all of them. The resulting significant contrast between filaments and the background then allowed a simple threshold to produce a binary image. We found a value of the 90^{th} percentile of the fluorescence intensity produced reliable results for our data. Any elements containing fewer than 20 pixels are then removed, and the binary was eroded by the *bwskel* function, which removes pixels from the perimeter of objects until a single pixel thick skeleton remains.

4.5.2.3 Image rotation

Images are then rotated so that the long axis of the cell aligned with the horizontal axis. We tried rotating both before and after the skeletonisation step, finding that rotation first can lose some information due to the discrete nature of the pixels, while rotating the skeleton afterwards can result in fragmentation of areas. In the end, we found the best result involved performing the image rotation both before and after the skeletonisation process, with the results then combined with pixel-wise OR logic. The results are then eroded away again to ensure each filament is only one pixel thick.

4.5.2.4 Skeleton Labelling

We label each filament in the skeleton with its own unique integer, such that only the pixels within that filament have that number. To avoid connected branches having the same label, we first temporarily remove the branch points using the *bwmorph* MATLAB function. Next, we flood-fill all the components of the network to label the different isolated filaments, using a combination of *bwconncomp* and *labelmatrix*. A side effect of this process is that long filaments with multiple branches are broken into distinct pieces between branch points. To rectify this we use a custom joining algorithm to re-join filaments (see Supporting Information for details) so that, at each branch point, the two filaments that are closest in direction are joined. This is done for every branch point and a final pass ensured that the labelling is continuous for all filaments.

4.5.2.5 Measuring Properties

After every filament is uniquely labelled along with a list of start and end points, a number of quantitative measures can be calculated. First, filament length in two dimensions is found by counting the number of pixels with a given filament label with diagonal connections weighted by an additional factor of $\sqrt{2}$ (see SI for details). If three-dimensional data (*i.e.* multiple z-stacks) is available, the filament length is extended to three dimensions. To do this, the location of the brightest pixel in the image stack is used to determine the z-position at each point in the skeleton, from which the mean angular displacement of the filament relative to the image plane can be calculated. The 2D projection length then gives an estimate of the real 3D length (see SI).

Second, filament width is estimated by measuring the local direction of a filament and then measuring the length of the binary image (before erosion for skeletonisation) perpendicular to that direction. This is repeated for every pixel along the length of the filament and averaged to find the mean filament width.

Third, filament angles are defined relative to the major axis of the cell. Using the MATLAB *regionprops* function, the binary mask that was initially used to remove all data outside of the cell can be used to determine the cell orientation relative to the horizontal axis. The image can then be rotated such that the major axis is parallel to the horizontal axis. This is not necessary for cells without any polarity. Once the image is rotated, all labelled filaments have their 2D orientation determined by finding the displacement in x and y between their endpoints and using the inverse tangent. As no information is typically available about the direction of the individual filaments, their angle is only defined in the range $[-\frac{\pi}{2}, \frac{\pi}{2}]$. The same can be repeated in 3D by calculating the displacement and therefore the angle relative to the image plane.

Fourth, filament curvature is defined using the Menger curvature: the inverse of the radius of the circle that passes through three points (Léger 1999). Each internal pixel (no curvature is defined at the endpoints) in a filament is chosen as a central point. Then the adjacent points a characteristic length λ away are determined. For pixels closer than λ to an endpoint, the largest possible distance is chosen (*i.e.* the endpoint itself is used). The curvature is measured for these three pixels, iterating along the filament and averaging to determine the average curvature of a filament. The deviation of a filament is defined as the average distance between each pixel in the filament and the straight line joining the two endpoints.

Finally, calculation of the branch angle requires a branch point and two or three labelled filaments connected to it. The filament end points not connected to the branch point are determined and used in conjunction with the branch point itself. Each unique pair of end points (three in total) are combined with the branch point in the middle to produce three different angle pairs. The angles with the smallest deviation travelling from one filament to the branch was taken to be the main filament, with the middle angle then defined as the branch angle. The branch ratio is a measure of how much a network

system branches, defined as the total number of branch points divided by the number of individual filaments.

All of the available measures can be found in table 4.1

4.6 DRAGoN Supporting Information

4.6.1 Algorithm Design

Properties of individual filaments are determined by iterating through filament labels and creating a binary image of each filament. Label numbers are contiguous from 1 to the number of filaments, so the filaments are first separated into their own binary images by only keeping the pixels with the number equal to that of the filament label. This enables measurements to be made more easily, without interference with other filaments and allows the easy storage of data in an array, where the index corresponds to the filament label. This process allows the leverage of powerful tools built-in to MATLAB, such as *bwmorph* for manipulating binary images and skeletons through a range of morphological operations.

4.6.1.1 Filament Orientation

Filament orientations in the two-dimensional imaging plane, frequently referred to in the program as the XY plane, are relative to the major axis of the cell. The major axis is found by fitting an ellipse to the cell mask which has an angle from the x-axis to the major axis of the ellipse with the same second-moments as the cell mask, via the *regionprops* function. The image is then rotated by this angle such that the major axis is now aligned with the x-axis, allowing easier comparisons between cells. Filament orientation doesn't use *regionprops* however, but instead takes the line joining the end points, which are found via *bwmorph*, and calculates the angle relative to the x-axis via the inverse of the tangent function. This ensures the ultimate direction of cargo travelling along the network is measured, despite any kinks in the filament due to microtubule movement or long curves around organelles or even curved walls and membranes. As the 2D image used for extracting the network is a maximum projection of a stack of 2D images at a range of z-positions, this stack is used to estimate the 3D position of the filaments. For each pixel in the skeleton, the intensity

of the corresponding pixel in each image of the stack is measured and compared, with the plane of the greatest intensity being reported. While resolution in z is much poorer than in the imaging plane, an estimate of the filament orientation can be made based upon stack separation and these maximum pixel values. The cosine rule is used to estimate the angle of the filament in 3D relative to the filament in the maximum projection.

4.6.1.2 Filament Labelling

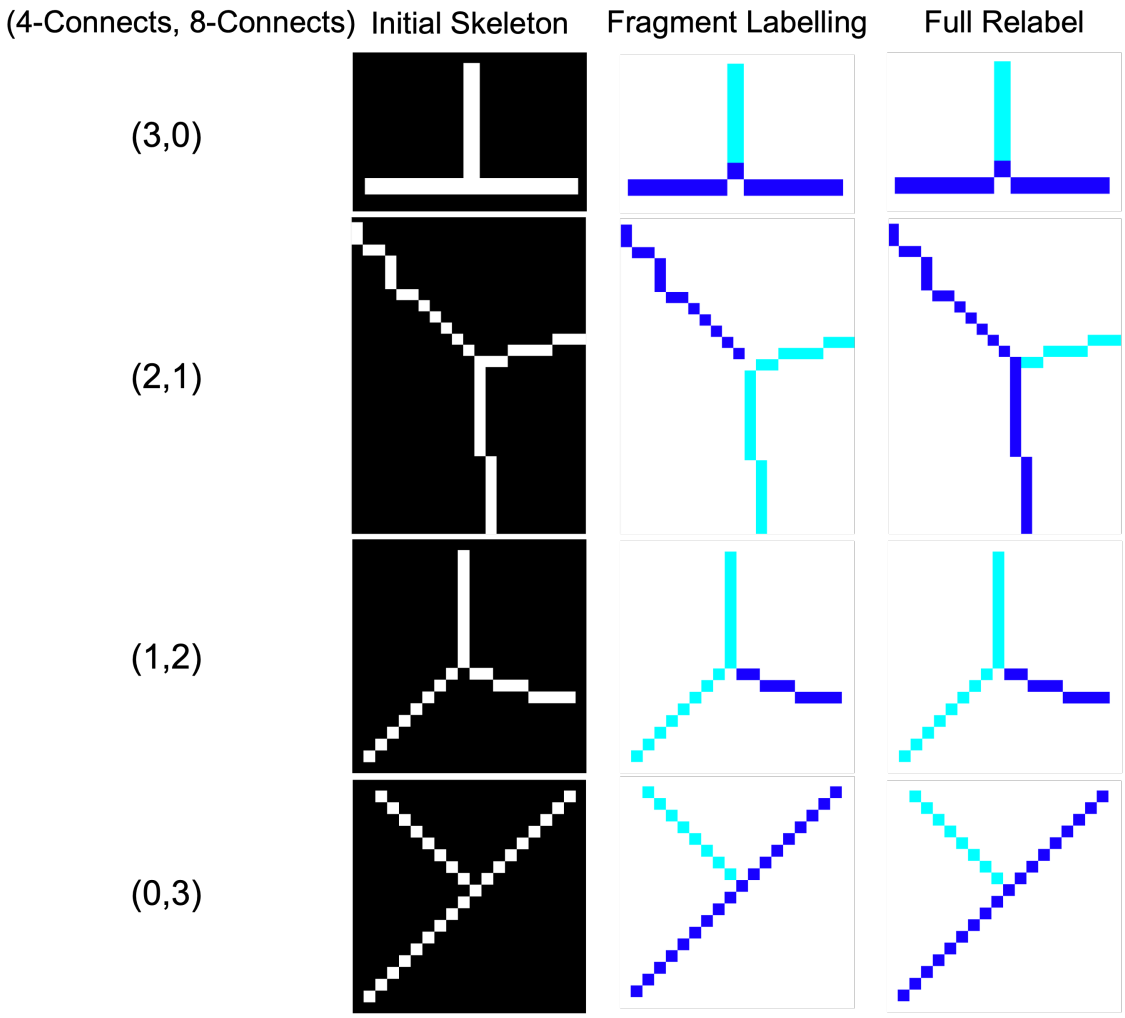

Figure 4.4: Filament Labelling: Flood fill algorithms used for labelling filaments require disconnects at branches to function as desired, otherwise every pixel in the skeletons shown would have the same label, making the process redundant. This fragmentation process can cause issues, however, as remaining 8-connected filaments can connect the network incorrectly in some cases. Additional checks and relabelling have been implemented in the right-most column to address this infrequent issue.

Correctly labelling each filament enabled all of the measurements made in the analysis tool. This process was done in stages, further refining the labelling at each stage to accurately represent the network. Fragmentation of the network was the first step, to give

each filament, between branch points, and on branches, a unique label via a flood-fill algorithm. This was achieved by determining the branch points with *bwmorph* and removing them from the skeleton. Multiple passes had to be made to ensure that filaments connected horizontally or vertically weren't still connected diagonally after the initial branch point removal. As this process split filaments at every branch point, these points were checked in order to determine how to rejoin the network with the branch getting one label and the main filament another. Comparing the orientations of different filament pairs connected to the branch point allowed the straightest pairing to be giving a single label and rejoined, while the branch was left with a different label. A parameter for the characteristic length away from a branch point was used for the filament orientation, as long cables are free to bend and change orientation far from the branch and this shouldn't influence the choices made. As this process resulted in a label number being unused, these numbers were stored and once the process was complete, the highest number labels were replaced with these missing values. This ensures that for n filaments, the labels are always from 1 to n. In some cases, the branch point removal only resulted in two filament labels, but had the labelling still incorrect, as shown in figure 4.4. Relabelling these filaments is more problematic, and this only occurs when a branch point has two 4-connected pixels and one 8-connected pixel, albeit only some of the time. All of these cases are checked, with the 4-connected pixels removed in order to yield 3 fragments, with another flood fill process occurring to separate the labels. The same algorithm as described above can be used to determine the correct labelling, with the extra step of replacing those previously removed 4-connected pixels, and converting the new label numbers (always 1,2,3) back to whatever the original pair of labels were. This process only had two labels to begin with, so no renumbering was required.

4.6.1.3 Filament Length

Filament lengths in the XY plane are determined by their number of pixels N_{px} and the way these pixels are connected. A fixed number of pixels orientated horizontally or diagonally will have a different length, and filaments which are not linear cannot be measured by calculating the distance between endpoints. The distance between 4-connected pixels (horizontally or vertically) is equal to the size of a pixel, but the distance between any

diagonally connected pixels is larger by a factor of $\sqrt{2}$. To determine the number of diagonal connections, each filament is relabelled, but this time with a restriction that filaments can only be 4-connected. Therefore the number of labels N_{lbl} is equal to the number of diagonal connections plus one. From here, the filament length l is calculated as,

$$l = N_{\text{px}} + (N_{\text{lbl}} - 1)(\sqrt{2} - 1). \tag{4.1}$$

For 3D length calculations, the average angle of the filament relative to the imaging plane is first calculated (the 3D filament orientation), then the 2D length is scaled by the reciprocal of the cosine of that angle.

4.6.1.4 Branch Angles

At a branch point, there are three possible pairs of filament directions that could be used to define branch angles: the angle of the main filament relative to itself before and after the branch as well as the angle between the branch and the main filament, both before and after the branch. If the main filament isn't perfectly straight, this gives three different angles. First, to measure the angles, a length scale is defined in order to avoid any kinks or deviations far from the branch in longer filaments. From here, the filaments are temporarily cut, and the three end points determined via *bwmorph*. The three ends form 3 unique pairs of ends, with the branch point being the third point of the triangle. These three angles are calculated via the cosine rule, and the middle angle is selected as the branch. This is because a small angle would be associated with going backwards down the main filament and having to change direction significantly to follow the branch, while a large angle is likely to be continuing down the main filament. The selected angle is then taken away from π such that the final angle is actually a measure of the deviation a molecular motor would have to take in order to follow the branch instead of continuing on the main filament.

4.6.1.5 Filament Width

Filament widths are determined by the average width at every point along a filament. For every pixel in a filament, the direction of the filament is found, such that the perpendic-

ular direction can be calculated in order to determine the width. A parameter is used to determine the length scale over which to determine the direction, as longer lengths can be more accurate in the case of a straight filament but can be erroneous for curved filament, therefore a length of approximately 0.5 μm was chosen to be suitable here. The binary image before skeletonisation is used to measure the width, as the filtering and thresholding process is consistent and provides a good estimate for filament width. The algorithm moves pixel-by-pixel along the width until the binary image yields a false value, then does the same in the negative direction, in case the skeleton isn't perfectly central. These two distances are added to give the width at this point, and this is repeated for every pixel to yield an average width.

4.6.1.6 Curvature and Deviation

Almost all filaments in the networks analysed were not completely straight, so these deviations and the curvature needed to be characterised and measured. The deviation is a very simple measure in which a straight line was drawn between the filament endpoints, and the distance between this line and each pixel in the filament was measured, such that an average could be taken. The distance for the point (p_x, p_y) away from the line defined by $(e_{1,x}, e_{1,y})$, $(e_{2,x}, e_{2,y})$ is given by

$$r = \frac{|(e_{2,x} - e_{1,x})(e_{1,y} - p_y) - (e_{1,x} - p_x)(e_{2,y} - e_{1,y})|}{\sqrt{(e_{2,x} - e_{1,x})^2 + (e_{2,y} - e_{1,y})^2}}. \tag{4.2}$$

The curvature of a filament, while always being defined as positive as it's the reciprocal of the radius, was made up of measurements of the curvature at every pixel, and therefore these individual components could be signed. Two separate measures are used here, where the components are summed as is, or the magnitude is always taken, before finding the mean and taking the absolute value of the final result. To measure the curvature at a given point, the position of the filament at a characteristic length λ away from the point is chosen, in both directions. The triangle formed from these three points (a, b, c) was used to measure the Menger curvature with

$$c(a, b, c) = \frac{1}{R} = \frac{4A}{|ab||bc||ca|}, \tag{4.3}$$

where the triangle area is determined by

$$A(a,b,c) = \frac{1}{2}|(x_a - x_c)(y_b - y_a) - (x_a - x_b)(y_c - y_a)|, \tag{4.4}$$

and the side lengths are

$$\begin{gathered} |ab| = \sqrt{(x_b - x_a)^2 + (y_b - y_a)^2}; \qquad |bc| = \sqrt{(x_c - x_b)^2 + (y_c - y_b)^2}; \\ |ca| = \sqrt{(x_a - x_c)^2 + (y_a - y_c)^2}. \end{gathered} \tag{4.5}$$

The choice of λ affects the result of the curvature due to the coastline paradox, and was used to uncouple the relationship between pixel size and curvature. The length defined here, is the maximum distance (always chosen if possible) between each point in the triangle. This process is repeated for all filament pixels not located at endpoints.

4.6.2 Algorithm Validation

4.6.2.1 Length, Curvature and Deviation

Figure 4.5 shows three filaments which contain the same number of pixels with substantially different lengths and curvatures. Each filament has its length measured, its average Menger curvature calculated, and the average distance from each pixel to the straight line joining endpoints determined. The curvature is determined on a length scale suitable to the resolution of the image and the capture device (up to 5 px between sampled points in this case) and is calculated both in signed and unsigned variants, before the absolute value being taken. Filament a has the shortest length of 23 pixels, with filament b being the longest at 32.1 pixels and filament c is 27.1 pixels long. Filament a has no curvature or deviation, whereas filament b has the greatest unsigned curvature with a smaller deviation than c. For signed curvature, c has greater curvature due to its consistent direction relative to b.

Additional testing of curvature was performed on unit circles and alongside manual calculations for three given points, all of which were accurate.

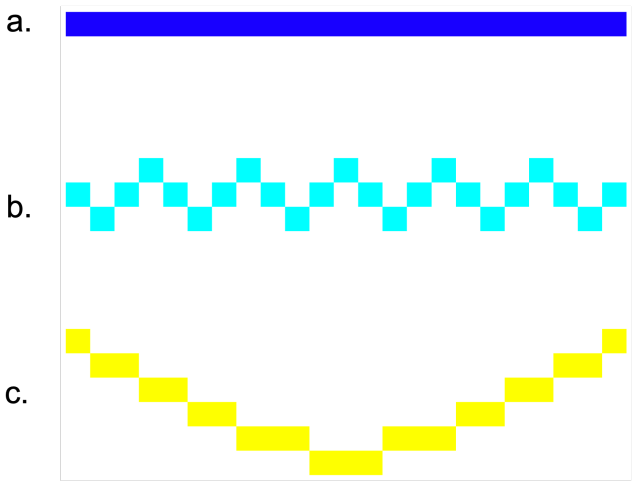

Figure 4.5: Describing Filaments: Various arrangements of 23 pixels represent filaments with different lengths, curvatures, and deviations from being linear. A range of statistics describing the different properties of these filaments is used to classify and differentiate them.

4.6.2.2 Branch Angles

A range of different angle cases were tested and are shown in figure 4.6. The scenarios were made to test a range of different edge cases, with straight lines between known coordinates of ends and branch points used to calculate the expected result accurately. As the algorithm uses a length scale over which to determine the angle, and the pixel network is discretised and therefore the lines are not perfectly represented, small errors in the calculated angle are expected. The errors measured here range from 0.05% to 1.25% and therefore are perfectly valid in the scope of the project. The benefit of testing branch angles is that it encompasses testing filament angle measurements as well, and these must therefore also be accurate.

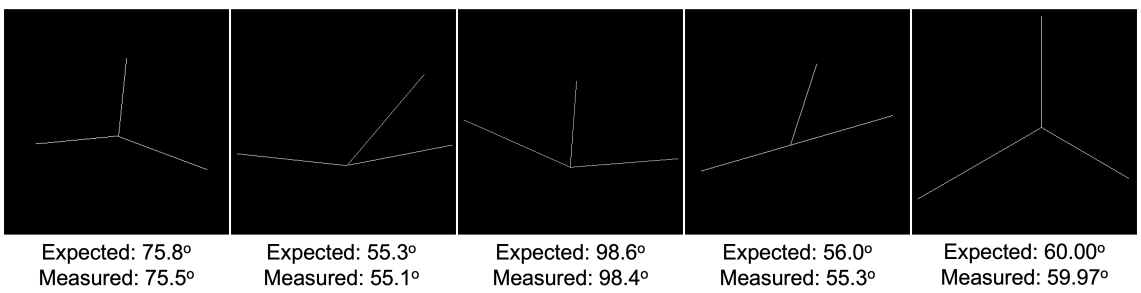

Figure 4.6: Branch Angle Validation: A range of different branch scenarios were tested, with known angles being compared to those measured. Small deviations from expected measurements are due to branch point estimates being a pixel out in some cases, or imperfect representation of lines onto discrete pixels, as well as small errors from not measuring the full filament length. Largest error is 1.25% and the smallest is 0.05%.

4.6.3 Skeletonisation Testing

4.6.3.1 Superscaling

Sampling data more frequently (spatial, temporal or both) than the desired output and averaging over several data points to achieve higher resolution has been used for a wide range of applications. As the targeted microscopy assay for the testing has a pixel size of $95nm^2$ and the filaments to be sampled started at 5 nm thick, we employed this technique spatially when artificially generating filament data. To achieve the 5 nm size, the pixels were cut into 19 subpixels in each dimension, resulting in a 19^2 increase in array size (200x200 -> 3800x3800). Any filaments were reconstructed in the new array with their positional co-ordinates being scaled by 19 and the desired thickness based upon filament width. From here a Gaussian blur with standard deviation matching the point-spread function of our microscope was applied to the array, with the pixel size scaled by 19 to match the new pixel size. From here, each 19x19 block of subpixels in the image was combined and averaged to reform the 200x200 image.

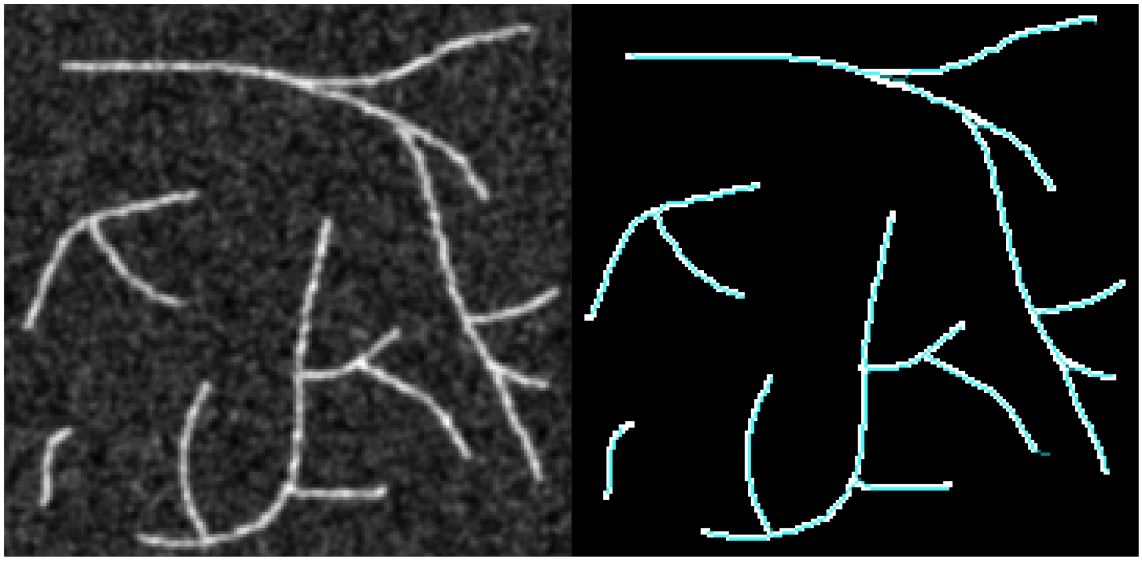

Figure 4.7: Skeletonisation In An Artificial Data Set: The initial image is shown on the left, with the skeleton that was extracted, roughly following the centre-line of the filaments, superimposed over the image on the right.

4.6.3.2 SNR Variation

The images generated for skeletonisation testing were 200x200 unsigned 8-bit integer arrays (uint8, range: 0-255). Two random points in this array were chosen as the filament ends, by uniform random number generation of values between 1 and 200, for both co-

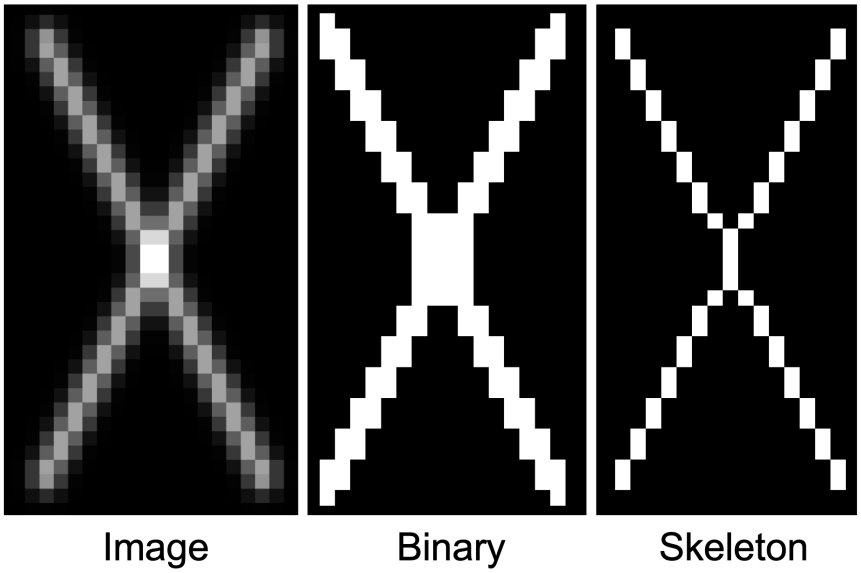

Figure 4.8: Crossing Issues: Two filaments intersecting frequently results in their skeletons combining for several pixels around their crossing. This makes evaluating branching and crossing very challenging.

ordinates. The midpoint of the line connecting these end points was calculated by taking their mean, and both the co-ordinates of this midpoint were shifted by a random amount between 0 and 15 to add curvature. 10 filaments were generated independently of each other and added to the image. These filaments were 3 pixels thick and had varying brightness depending on the signal-to-noise ratio being targeted. For high SNR, the filaments had an intensity of 80, while the medium and low SNR groups had an intensity of 60 and 50 respectively. A binary image of the filament-only image was also generated to give the mask for SNR calculations. To generate the noise, another 200x200 uint8 array was generated with salt and pepper noise, resulting in 40% of the values being 1 and the remaining 60% being 0. Each element of the array was scaled by a random number, ranging from 0 to the maximum noise value parameter, which varied depending on the SNR level being targeted. This was 80 at high SNR, with 120 and 140 being used for the middle and low SNR images. The noise array was added to the array containing the filaments, and a Gaussian blur (0.9 pixel radius) was applied to obtain the final image. The SNR is defined in equation 4.6. The mean value of the signal μ_{sig} was measured as the mean value of all the true pixels in the filament-only binary image, while the standard deviation of the noise σ_{noise} was simply the standard deviation of all of the remaining pixels.

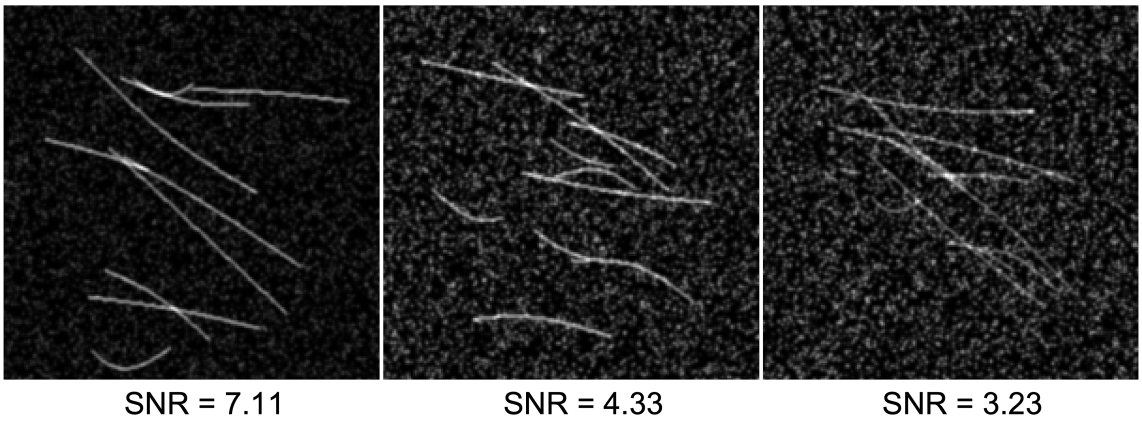

Figure 4.9: Various SNR Levels: Example images of artificially generated data at different SNR levels. As the SNR drops below 4, the amplitude of the noise eclipses the filament signal and any filaments in proximity of each other are indiscernible.

$$\text{SNR} = \frac{\mu_{\text{sig}}}{\sigma_{\text{noise}}} \tag{4.6}$$

4.6.3.3 Numerical Aperture

For a zero mean Gaussian distribution, we derive the full width at half maximum (FWHM) to determine the relationship between the minimum resolvable distance and the Gaussian standard deviation σ. A zero-mean Gaussian is given by

$$f(x) = \frac{1}{\sigma\sqrt{2\pi}} e^{-\frac{x^2}{2\sigma^2}}. \tag{4.7}$$

If $x_{0.5}$ is the point that the Gaussian amplitude reduces to half it's maximum value, then the FWHM is defined as $2x_{0.5}$ due to the symmetry about the mean of zero, therefore we can write

$$f(x_{0.5}) = \frac{1}{2\sigma\sqrt{2\pi}} = \frac{1}{\sigma\sqrt{2\pi}} e^{-\frac{x_{0.5}^2}{2\sigma^2}}. \tag{4.8}$$

By cancelling the common amplitude constants and applying a natural logarithm, we arrive at

$$\ln\frac{1}{2} = -\ln 2 = -\frac{x_{0.5}^2}{2\sigma^2}. \tag{4.9}$$

Rearranging and solving for $x_{0.5}$ we see that

$$x_{0.5} = \pm\sigma\sqrt{2\ln 2} \approx \pm 1.177\sigma \tag{4.10}$$

and therefore the minimum distance between two objects which can be resolved is $\approx 2.355\sigma$. We can set this equal to the FWHM resolution limit to get

$$2\sigma\sqrt{\ln 4} = 0.51\frac{\lambda}{\text{NA}}. \tag{4.11}$$

We can solve for σ and get

$$\sigma = \frac{0.51\lambda}{2\sqrt{\ln 4}\text{NA}} \approx 0.217\frac{\lambda}{\text{NA}}, \tag{4.12}$$

which, for the optimum GFP emission detection at 510nm, we arrive at

$$\sigma \approx \frac{110}{\text{NA}}\text{nm}, \tag{4.13}$$

highlighting that NA and resolution are inversely proportional. From here, we have an equation which can directly influence the size of the Gaussian blur that we apply to account for the effects of microscopy, such that we can test various NA values of different lenses. For our microscopy assay, we have a lens with NA of 1.35, giving a blur radius of 82nm, around 90% of the CCD pixel size.

Chapter 5

Image Analysis: Results and Findings

5.1 Introduction

The aim of this chapter of research was to use the DRAGoN tool on real, experimental data to display its ability to detect subtle differences in the network, highlighting its usefulness and robust nature. Three hypotheses were tested, and these are split into relevant sections in the results. Our first hypothesis states that any cytoskeletal differences in the actin mutants (*arp2-1* and *formin4/7/8*) compared to the wildtype will be subtle, due to their mild phenotype, but should still be detectable and quantifiable with sufficient data. This was tested on wildtype hypocotyls, prepared identically to Chapter 3, just with GFP-Lifeact labels and no immune responses. The next hypothesis stated that cell geometry and tissue types play a significant role in cytoskeletal design and structure. The hypocotyls from before were compared to older leaf tissue cells, which are different sizes, shapes, and in a different developmental stage, to give a sizeable shift in cytoskeletal requirements. The final hypothesis stated that the cytoskeletal requirements for pathogen invasion are different to normal cell function, therefore the properties of the network are expected to change. This was tested on leaf cells which had undergone a real, 48 hour infection under a powdery mildew.

5.2 Results

5.2.1 Application 1: *Arabidopsis* Hypocotyl Cells

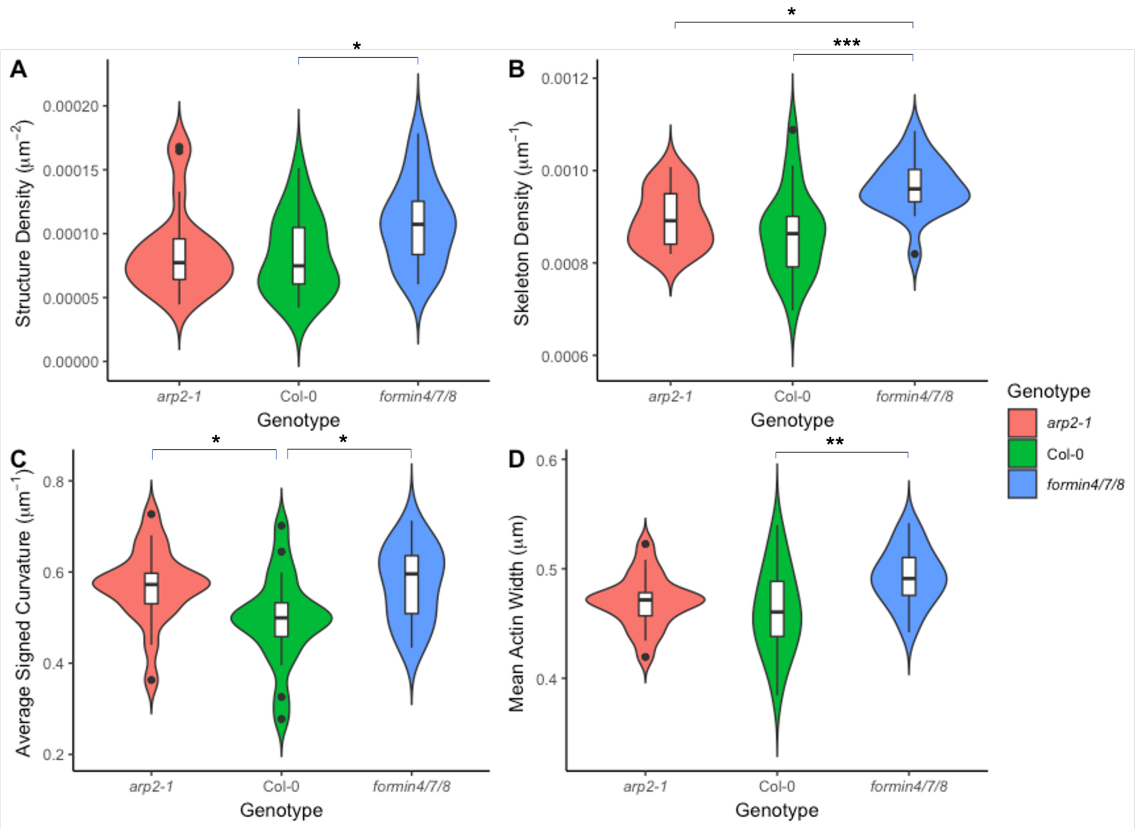

Figure 5.1: Comparison of the actin network in hypocotyls of the wild type, formin mutant and Arp2 mutant. Four measures (structure density, skeleton density, average signed curvature and mean actin width) showed significant changes between the wild type and *formin4/7/8* triple mutant. One of these (average signed curvature) also showed a significant difference between the wild type and *arp2-1* mutant and another (skeleton density) displayed a significant difference between the *arp2-1* and *formin4/7/8* mutants. Pairwise testing was performed with Tukey HSD after a MANOVA test. Single/double/triple asterisks represents $p < 0.05, 0.01, 0.001$ respectively. Sample size is 20 for the wildtype, 20 for the *arp2-1*, and 19 for the *formin4/7/8*.

Wild-type (Col-0) *Arabidopsis* hypocotyl epidermal cells with GFP-Lifeact were imaged and the actin network extracted as described above. These were compared to cells with loss-of-function mutations either in Arp2 (Mathur et al. 2003) or in three formin genes (Formins 4, 7 and 8 (Sassmann et al. 2018)). These were chosen as they are both mutants of actin filament nucleation regulators with stress-response phenotypes. First, a MANOVA (multivariate analysis of variance) test was used to determine if significant differences existed based on eleven dependent variables (skeleton density, branch point density, 2D filament angle, structure size and number density, filament width, deviation, signed and unsigned curvature, branch ratio and average 3D filament length). Only these

eleven measures were used, rather than the full set of seventeen, because they either were unimportant (cell orientation), used in other measures (cell size, filament angle from imaging plane), redundant (2D equivalents of the 3D measurements) or unsuitable for the data (branching angles are pointless if no branches are detected and this reduces power). The MANOVA test uses a linear combination of the dependent variables to create a single combination variable that is then tested against the genotypes. This showed significant differences between the three genotypes ($p < 0.001$), although it cannot reveal exactly where these differences lie. Next, to determine the variables most responsible for this significant difference, the Tukey honest squares difference (HSD) post hoc test was used, which identified a number of key differences between the wild-type, *arp2-1* and *formin4/7/8* plants.

First, a statistically significant difference was found in the density of cytoskeletal structures (see Fig. 5.1A). While the *arp2-1* knockout showed no significant difference to either the wild-type or the formin mutant, the *formin4/7/8* mutant displayed a statistically-significantly increased structure density compared to the wild type ($p = 0.046$), with an average increase in density of 31%. Given that no differences were found in the average size of these structures, this suggests that the formin mutant cells may have more filamentous actin, leading to a higher network density.

Second, the skeleton density was also significantly greater in the *formin4/7/8* mutant compared to both the wild type ($p < 0.001$) and the *arp2-1* mutant ($p = 0.012$), while the *arp2-1* mutant was similar to the wild type (see Fig. 5.1B). This again suggests a more tightly packed network in *formin4/7/8* deficient cells, perhaps due either to increased filamentous actin content or increased cytoplasmic volume per unit cell surface area. A reduction in coupling of the network to the cell membrane is unlikely to significantly reduce the cell surface tension, however, due to its relatively small contribution compared to the internal turgor pressure.

Third, compared to the wild type, the average signed curvature of filaments was increased in both the *arp2-1* ($p = 0.029$) and *formin4/7/8* ($p = 0.020$) knockouts (see Fig. 5.1C). As the Arp2/3 complex and formins are involved in coupling the cytoskeletal network to the membrane, a reduction in coupling could result in a drop in filament tension. It is

plausible that this tension creates more linear filaments, so that a reduction in tension would lead to more curved bundles in the mutants.

Finally, the mean width of actin bundles was higher in the *formin4/7/8* knockout compared to the wild type ($p = 0.0075$) whereas no statistical significance was found with the *arp2-1* mutant (see Fig. 5.1D). While the difference in thickness is smaller than our pixel size (32 nm versus 95 nm), this is an average over filaments, which are then averaged over their length, meaning that small differences can be detected. This may not seem surprising given the greater network density measured in *formin4/7/8* knockout cells, but some formins have been shown to have a function related to bundling and thicker bundles tend to be present in hyper-elongated cells, whereas the *formin4/7/8* mutant phenotype in hypocotyls showed slower elongation and smaller cells. This suggests that these cells may already be adapting in order to try to reduce these deficiencies.

5.2.2 Application 2: Comparing Hypocotyl and Leaf Cells

We next examined the actin cytoskeleton in epidermal cells across two tissues: hypocotyl and leaves. To do this, all hypocotyl experiments described above were repeated on 4-6-week-old *Arabidopsis* leaves, their actin networks were extracted and then compared. The MANOVA test was used again, this time with an additional independent variable (cell type). Inclusion of leaf cells rendered the combined tissue genotype less statistically significant ($p = 0.056$), whereas the cell type itself showed significant differences ($p < 0.001$). Hypocotyls and leaves have epidermal cells with distinct morphologies and different rates of cell expansion, which may be the dominant reason for differing cytoskeletal characteristics. For example, hypocotyl cells exhibit accelerated directional growth (these cells must rapidly expand and elongate to reach the soil surface in order to have access to light). This rapid growth needs to be supported by the cytoskeleton (Sampathkumar et al. 2011) and therefore a lack of important actin binding proteins may impact this growth rate and result in more exaggerated differences between the genotypes in the hypocotyl cells.

Given this MANOVA result, the Tukey HSD post-hoc tests were then performed on only the wild-type data in order to minimise any confounding variables. All genotypes are shown in Fig. 5.2 for completeness, which highlights the subtlety of the phenotype in

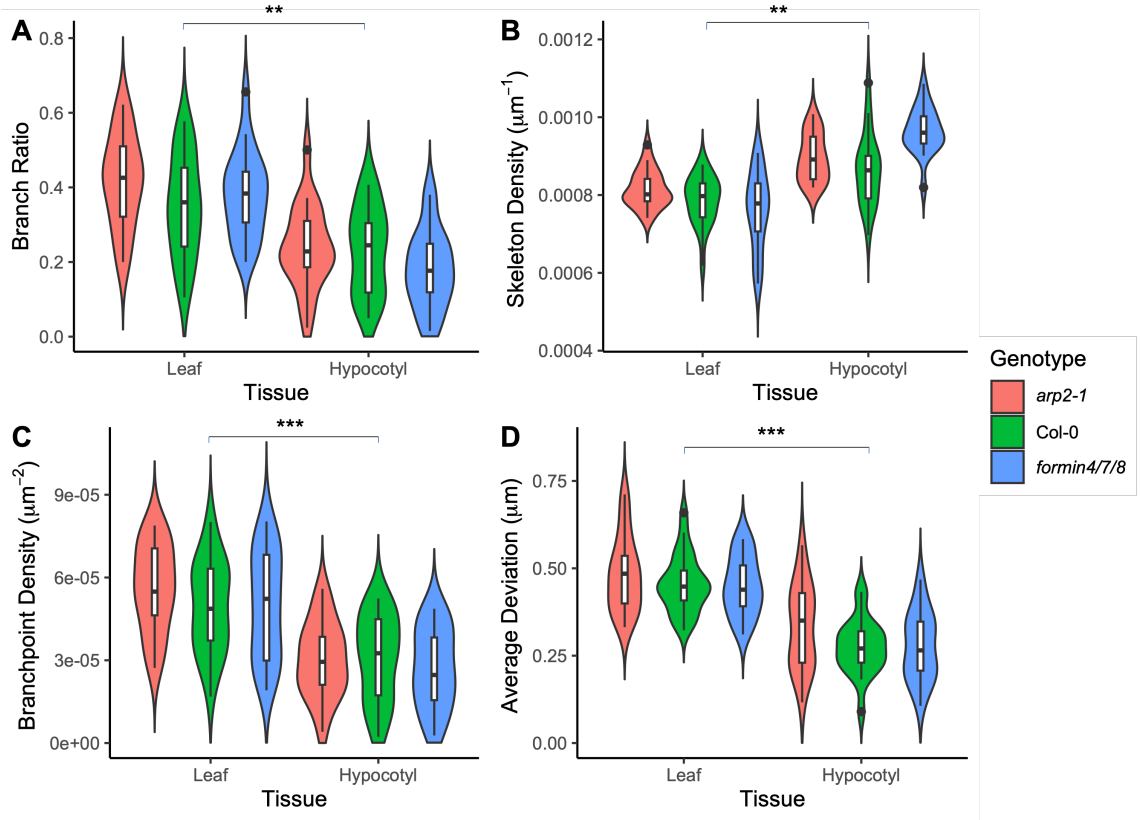

Figure 5.2: Effect of cell tissue on actin cytoskeleton. Four (branch ratio, skeleton density, branchpoint density, average deviation) out of eleven measures showed significant differences between wild-type hypocotyl and leaf cells. Significant differences are only shown between wild-type cells, although similar significance values were found between most genotype pairs. Pairwise testing performed with a Tukey HSD test after a MANOVA test. A double asterisk represents $p < 0.01$ and a triple asterisk denotes $p < 0.001$. Error bars show one standard deviation from the mean. Sample size for the wildtype is 20 hypocotyls and 23 leaves, for *arp2-1* it is 20 hypocotyls and 21 leaves, and the *formin4/7/8* has 19 hypocotyls and 20 leaves.

the mutants compared to the significant differences between cell type.

The branch ratio and branch point density, shown in Fig. 5.2A and Fig. 5.2C respectively, were both significantly higher in wild-type leaf cells than hypocotyls ($p = 0.0043$ and $p < 0.001$ respectively). The increased branching in leaves may be partly due to the less restrictive nature of the cell shape, allowing the network to form crossover junctions closer to perpendicular angles. This is likely to also be influenced by the large levels of cytoplasmic streaming that are observed in the long, thin hypocotyl cells. This streaming is generated through myosin motors on the actin filaments and bundles. Because the direction of motor assisted transport is defined by the structure of the cytoskeleton, these filaments are mostly aligned in the direction of the cytoplasmic flow (Goldstein and Meent 2015).

The skeleton density of wild-type leaf cells was lower in leaf cells compared to hypocotyl cells ($p = 0.0020$), shown in Fig. 5.2B. While the *formin4/7/8* knockout was significantly different to the wild type in hypocotyls, the leaf cells appear much more consistent across genotypes. This difference in tissues is again likely down to the different cell shape and size constraints: perhaps more space afforded by wider cells and a smaller vacuole, as well as less reliance on cytoplasmic streaming, reduces the need for such an organised, polarised network in leaves.

Finally, the average deviation of filaments and bundles from linear is significantly different ($p < 0.001$) between cell types, with greater deviation in leaf cells compared to hypocotyls (see Fig. 5.2D). As with the other differences, this is possibly due to a different set of requirements for the cytoskeletal network due to differences in cell shape and developmental stage. For optimal cytoplasmic streaming in the long and narrow hypocotyls, the actin network needs to be highly parallel to the major cell axis and straight. This is in contrast to the highly irregular shapes of leaf cells, which have a width much closer to their length. The curved cell membrane and cell wall impart significant deviations in the linearity of actin filaments near the cell edges.

5.2.3 Application 3: *Blumeria* Infections

Wild type, *arp2-1* and *formin4/7/8* knockout leaves were all infected with *Blumeria graminis* (*Bgh*) and imaged at 48 hours post infection. MANOVA testing showed no significant changes due to genotype ($p = 0.25$), pathogen ($p = 0.079$), or a combination of the two ($p = 0.086$). Despite this, it is possible that some combination of measures could still show a significant difference. To test this, a principal component analysis (PCA) was performed, which scales, shifts and combines all variables into an alternative, yet equivalent, set of principal components. The aim of this is to encapsulate as much of the variation in the data as possible using only a subset of the principal components. This variance as a function of the principal component number is shown in Fig. 5.3, with the dotted line showing the mean percentage of variance over all principal components. The first four principal components contribute more than this mean, containing between them 77% of the total variation. By selecting only these four components and performing another MANOVA

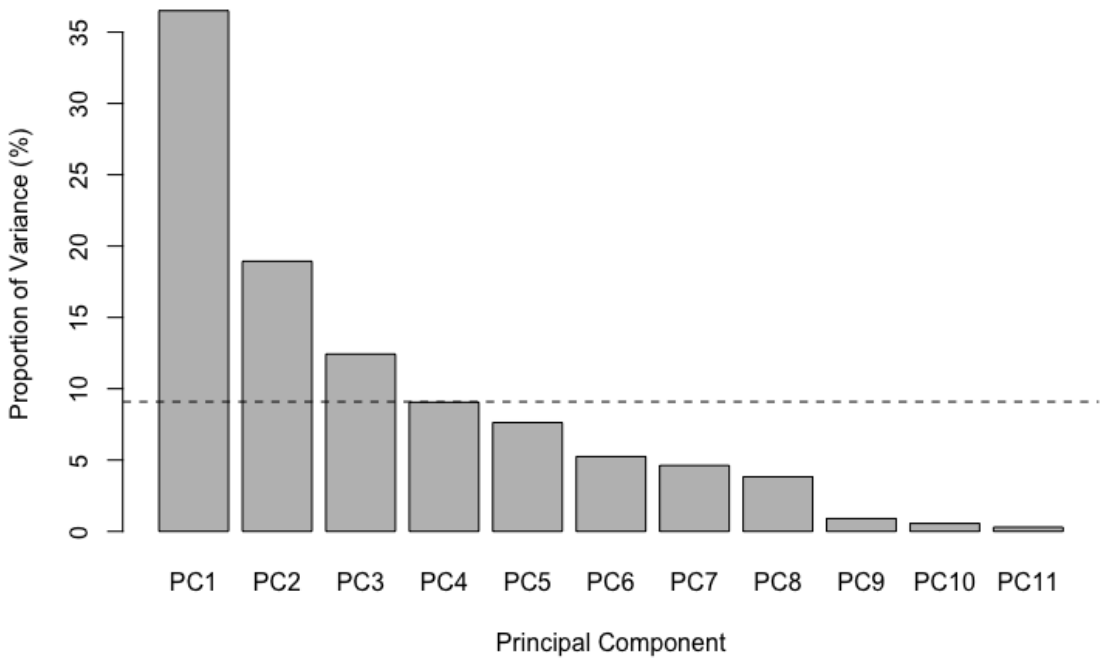

Figure 5.3: Principal component analysis (PCA) of *Blumeria graminis*-infected and uninfected leaves. Shown is the percentage of the variance that is explained by each of the principal components. The dotted line shows the mean percentage of variance over all principal components. The first four components contribute more than or equal to this mean and are therefore kept for future analysis. Sample includes 20 uninfected leaf cells and 5 infected cells.

test, genotype ($p = 0.037$), pathogen ($p = 0.0020$) and their combination ($p = 0.033$) were all significant.

Bgh was chosen as a pathogen due to its reported ability to perturb the actin network and direct trafficking during non-host immune responses (Takemoto et al. 2006). Cell wall reinforcement and successful defence have been shown to be dependent upon actin dynamics (Yun et al. 2003). These effects are however highly localised and their impact upon the overall properties of the cytoskeleton across the cell is likely to be subtle. However, it is promising that, despite this, our algorithm is still able to identify significant differences between infected and non-infected cells (albeit without allocating these to specific descriptors). With a larger sample size or higher resolution images, a better understanding of the filamentous actin around the infection site would likely be achievable by using our algorithm at the sub-cellular level to compare local network properties.

5.3 Discussion

In this study we applied our code to several real examples from *Arabidopsis thaliana*. First, we examined how the actin cytoskeleton differed in wild-type cells compared to two null mutants: *arp2-1* and *formin4/7/8*. We found that, in hypocotyl cells, both mutants showed significant differences relative to the wild type in four separate measures, including filament curvature and width. The signed curvature was greater in both mutants compared to the wild type, while the average actin width was larger in the *formin4/7/8* mutant than the wild type. Both mutants had a higher skeleton density than the wild type, but only *formin4/7/8* had an increased structure density. This possibly points to the reduction of membrane anchoring points for the cytoskeleton, one function of formins (Cvrčková 2013), reducing tension and support in the network, which may result in adaptions being made in order to bolster strength.

Next, we examined hypocotyl versus leaf cells, finding significant difference in branching (leaves have a higher branch point density) and network density (hypocotyls have higher density). The detection of these significant differences between tissues highlights the different requirements of leaf and hypocotyl cells. It is plausible that the difference arises since hypocotyl cells require much of the network to run parallel to the cell's long axis to aid with transport, increasing packing density of the cables and reducing the need for branching. This may further be reinforced by reduced deviation of the filaments in hypocotyl cells.

Finally, we examined the response of *Arabidopsis* leaf cells to infection by *Blumeria*. Identifying significant differences were more difficult in this case, although was possible by using PCA analysis. By taking the four principle components that contributed more than the mean total variance, we showed that *Bgh* has a detectable impact on the actin network, although we were unable to identify the particular microscopic network differences at play. Our analysis only considered the actin network of the whole cell. Since *Bgh* infection may only modify the cytoskeletal network close to the point of infection, we may have missed local network changes. This could be remedied by optimising data acquisition to analyse the network of the region around the infection site. This would need to be performed at diffraction-limited resolution and at high time resolution to prevent

dynamic filament smearing in projected images.

The ability to identify differences in specific parameters can indicate the action of specific classes of actin binding proteins and their associated signalling pathways in tissue differentiation. The measured changes across genotypes shows that even more subtle differences can be detected and measured, which should allow even better insight into the mechanisms underlying the cytoskeletal processes. While we were unable to quantify the differences in the network induced by pathogen invasion, the fact a difference could be found using principal component analysis suggests that as yet undefined ratios of network properties characterise the response to pathogen assault. The changes in proximity to the appressorium are often highly visible, whereas the rest of the network appears to remain similar. It is possible that changes occur here, but they will be very subtle, therefore most of the changes are going to occur in a small region and measurements across the whole cell will only change by a very small amount. A much larger data set or perhaps an artificial stimulation of the immune response (*e.g.* a microneedle assay (Hardham et al. 2008)) may help in discerning these changes in more detail.

The dynamic nature of the actin cytoskeleton and the noisy nature of microscopy means that a perfect network extraction tool cannot exist. Our tool has a number of limitations. First, we focus on extracting actin bundles rather than the finer F-actin structure (which was motivated by the nature of our training data but precluded analysis of highly dynamic filament populations). Second, while the code has support for 3D data sets and measurements, these are currently implemented in only a simple manner by estimating z-positions from stack intensities. In future, better isolation of the filament position in 3D would enable additional information to be gathered on measurements such as curvature and branch angles, as well as enable new types of 3D measurements. Third, our tool is designed to work at single time points. A future extension could involve frame-by-frame filament tracking. This would allow network remodelling to be analysed in greater detail, and the network in nearby time points could be used to inform and improve filament detection, providing more information than is possible by using single images in isolation.

While the software was designed using data from *A. thaliana*, particularly images from leaf and hypocotyl cells, we have aimed to create a general resource that is easily

adaptable to other cell types and organisms. For example, quantifying the network structure in other plant tissues and cell types, such as roots and root tips, would likely be straightforward. Further, we expect our algorithm (with suitable parameter changes) will also perform well on other organisms, including animal cells. Structures other than actin are likely to be analysable with only minor modifications. For example, extracting the microtubule network is a substantially easy task than that for actin due to their increased and more-consistent thickness. However, it is worth pointing out that there will be significantly more crossing events for microtubules and so an improved method of network reconstruction (perhaps by more fully utilising every image in a 3D stack) would be needed. Finally, it will be worth investigating whether out approach can be used to extract multiple different networks from single images. For example, since filament width is already on output of our algorithm, it may be relatively straightforward to add a method that segments the cytoskeleton into F-actin, intermediate filaments and microtubules (given sufficient labelling and resolution to distinguish between them).

In addition to the points mentioned above, there are a number of further ways that our tool could be extended in future. First, we have used the 3D data provided by z-stacks only to estimate 3D filament lengths and angles. More fully reconstructing the full 3D network could have a number of important applications, particularly in animal cells where the lack of a central vacuole increases the importance of the full three-dimensional actin structure. Second, we currently analyse images at single time points. Identifying the network at neighbouring time points (with, for example, some modified Hungarian algorithm) could lead to both an improved accuracy of network extraction and a way to quantify dynamic network changes (for example, in response to fungal attack). Third, previous work in this area utilised analysis of the actin structure to measure organelle motility (Breuer et al. 2017). With our algorithm, this could naturally be extended by using the improved network quantification that our software yields. By including measurements such as curvature, matching organelle movement to actin tracks is likely to be more accurate and provide additional data to explore mechanisms and design mathematical models. Fourth, since analysis of a single frame takes only a couple of seconds with our algorithm, network extraction could be performed in real time, with results instantly fed back to the microscope user. Near real-time analysis could inform which areas of the cell to probe for

an immune response or for how long to apply a perturbation (such as in the nanoindentation experiments that have been used to test for actin remodelling to a physical stimulus (Branco et al. 2017)). Further, for laser dissection experiments, immediate and detailed information and statistics of the actin network could suggest which cables to sever.

Our DRAGoN tool demonstrates that accurate extraction of the actin network structure can be accomplished with only minimal human interaction. Further, the same general algorithm will be relevant across cell types, tissues, organisms and network types. Applications of this work are widespread and range from basic biological understanding to global crop security. As a result it is likely that such tools will become increasing common and important in biology as improved methods of imaging the fine detail of actin and other cytoskeletal elements become available.

5.4 Conclusion

Using the DRAGoN algorithm, we studied a number of cases in *Arabidopsis thaliana*, including several different tissues, a variety of actin-affected mutants, and cells responding to powdery mildew. In many cases we found statistically-significant differences in actin network properties. In addition to these results, our algorithm is designed to be easily adaptable to other tissues, mutants and plants, and so will be a valuable asset for the study and future biological engineering of the actin cytoskeleton in globally-important crops.

5.5 Methods

The DRAGoN algorithm was used to analyse images of the cytoskeleton using GFP-Lifeact infused *A. thaliana* hypocotyl and leaf cells, as described in 4.5.

5.5.1 Plant and Pathogen Growth

5.5.1.1 Plant Material

Arabidopsis thaliana ecotype Colombia-0 (Col-0) with GFP-Lifeact were grown as the wild type, alongside loss-of-function mutations in Arp2 (SALK SALK_003448) or three formin

genes (Formins 4, 7 and 8) as described in Sassmann et al. 2018.

5.5.1.2 *Arabidopsis* Hypocotyls

A. thaliana seeds were sterilised with Cl_2 for 4-5 hours in a sealed container by mixing 100 ml of bleach with 3 ml of 37% HCl. Sterilised seeds were suspended in molecular biology grade water and stored in the dark at 3°C for a minimum of 5 days. To produce the extended hypocotyls, seeds were dark grown in a humid growth chamber at 21°C for 5 days. 100 µl half-concentration Murashige and Skoog (MS) growth medium with Gamborg's Vitamins containing 0.8% w/v agar was used as the growth medium, upon which the seeds were placed. 500 µl centrifuge tubes were used to contain the medium and support the hypocotyls.

5.5.1.3 *Arabidopsis* Leaves

10-15 *A. thaliana* seeds were sown onto F2 soil with sand, mixed with vermiculite in a 3:1 ratio. The seeds were left in the dark at 3-5°C for a week, then transferred to a growth cabinet (16 h light, 8 h dark) at 21°C. After 1-2 weeks more, plants were transferred to a new pot as to grow uncontested.

5.5.1.4 *Blumeria Graminis*

Blumeria graminis (*Bgh*) was cultivated on "Golden Promise" barley (16h light, 8h dark) at 17°C by weekly infection of three-week old barley plants.

5.5.1.5 *Blumeria* Infection

After 7 days of cultivation on barley, *Bgh* spores were sprinkled on whole plants for the elongated hypocotyls; they were placed back in the dark at 17°C for 24 hours and remained in their centrifuge tubes. For leaf infections, 4-6 week old A. *thaliana* plants were cut at the base of the petiole and placed on damp filter paper in a petri dish before spores were sprinkled on the adaxial (dorsal) surface. This assay was left in the dark for 48 hours at 17°C before imaging.

5.5.2 Imaging Methods

Images were taken with a spinning disc confocal microscope, equipped with a 60x lens and NA of 1.35. A laser power of 7 mW at a wavelength 488 nm was used for imaging GFP-Lifeact. Images were taken with 200 ms exposure and z-stacks had a separation of 0.55 μm. Entire hypocotyls were mounted while 5x5 mm squares of leaf were cut, away from the central vascular tissue, in order to keep everything as flat as possible.

Chapter 6

Mathematical Modelling of PEN3 Distributions

6.1 Introduction

The role and function of PEN3 was discussed in detail in 1.5 and briefly reviewed in 3.1. The occurrence and distributions of the zones of PEN3 enrichment in response to artificial stimulation were measured in 3.3 and discussed in 3.4. Here we will take a deeper look into these distributions and the possible mechanisms that generate them through the use of mathematical modelling. The required parameters relating to diffusion were determined through experimental methods and matching to models.

The aim of this chapter of research was to estimate the diffusion regime of PEN3 in the membrane (under normal conditions) and use this to explore the effect of various PEN3 delivery zone sizes on the shape of the PEN3 immune response. This was to enable testing of the hypothesis that the size of the PEN3 enrichment region is a product of diffusion in the membrane.

6.1.1 Theory of Extracting the Diffusion Constant

Once PEN3 has been transported to the membrane and secreted, it is free to diffuse in two dimensions. A range of methods exist in biological contexts to determine the prop-

erties associated with this diffusion, such as fluorescence recovery after photobleaching (FRAP) and single particle tracking (Saxton 1997; Shen et al. 2017). Single particle tracking provides a fairly simple analysis pipeline for the extraction of D through the relationship described in Eq. 2.10. For normal diffusion, a single particle with η degrees of freedom will travel a mean squared distance $\langle r^2 \rangle$ of,

$$\langle r^2 \rangle = 2\eta D t. \tag{6.1}$$

For our 2D membrane, simply fitting a line to $\langle r^2 \rangle$ vs t and extracting the gradient will provide the diffusion constant. The process of tracking a single particle; however, can be challenging, require specialist equipment, and carefully selected fluorescent probes (Alcor et al. 2009).

The FRAP method is much more accessible, as it requires looking at an entire ensemble of particles. By damaging the fluorescent label of a species in a relatively small region of interest (ROI), the exchange of fluorescing and non-fluorescing particles can be measured as a change in fluorescence intensity in the ROI (Shen et al. 2017). The calculations and measurements only require analysis of raw images and as many confocal microscopes are able to perform photobleaching, this is technique available to most. The downside of using FRAP is that analysis is based upon the average movement of many particles, therefore a more limited set of information is available and as such larger data sets may be needed.

A range of models mapping FRAP data to the diffusion constant are available, each with varying assumptions and complexities. One commonly used is the Soumpasis equation, which relates the radius of the bleached spot r to the characteristic diffusion half-recovery time $\tau_{1/2}$ (Wu et al. 1977; Bryers and Drummond 1998; Leddy and Guilak 2003). This half-recovery time is defined as the time it takes for the mean fluorescence intensity of the bleach ROI to reach halfway between the post-bleach F_0 and the steady state value F_∞. This requires finding the value of t that satisfies

$$F(t = \tau_{1/2}) = F_{1/2} = \frac{F_0 + F_\infty}{2}. \tag{6.2}$$

With these values, the constant of diffusion is calculated as,

$$D = 0.224\frac{r^2}{\tau_{1/2}}. \tag{6.3}$$

This is very simple, but is based upon the assumption that the bleaching laser is uniform and effectively instantaneous (*i.e.* diffusion during bleaching is negligible) (Soumpasis 1983) such that the edges of the bleached regions can be represented by a step function. As many systems violate these assumptions to varying degrees, adjustments need to be made. An extensive comparison of models and methods was performed by Kang *et al.* with extensions made such that the nominal and effective bleach radii are both taken into account (Kang et al. 2012). Full derivation and analysis can be seen in the Kang paper, but the main point is as follows: The nominal radius r_n, which is used to tell the laser where to bleach and the size of the spot to analyse for fluorescence recovery and $\tau_{1/2}$ calculation, is always smaller or equal to the effective radius r_e of the bleach ROI. As every laser has an effective spot size, and many have a Gaussian profile, this must be taken into account. Using Eq. 6.3 with r_n gives a lower bound estimate of D while using r_e gives an upper bound. Kang derived a measurement for the isotropic diffusion constant taking both of these measurements into account and found that

$$D = \frac{r_n^2 + r_e^2}{8\tau_{1/2}}, \tag{6.4}$$

which in the case of $r_e = r_n$ gives near-agreement with Soumpasis.

For diffusion in a membrane, where the surface area is much greater than the bleach spot size, the membrane can be treated as an infinite, two-dimensional plane ($\mathbb{R}^2$). A Gaussian laser profile is often used for the bleaching, which has an intensity profile I_{r_n} given by

$$I_{r_n}(r) = \frac{2I_0}{\pi r_n^2}\exp\left(-\frac{2r^2}{r_n^2}\right), \tag{6.5}$$

where $r^2 = x^2 + y^2$. If using circular bleach ROIs and assuming isotropic diffusion, it makes sense to use a coordinate system that matches the geometry, therefore any angular terms in Eq. 2.9 will disappear due to symmetry. Assuming that the concentration of the

fluorescent protein satisfies Eq. 2.9 then the fundamental solution for $\rho(\vec{r}, t)$ is given by,

$$\rho(\vec{r}, t) = \frac{1}{4\pi D t} \exp\left(-\frac{r^2}{4Dt}\right). \tag{6.6}$$

While it has been shown empirically that the shape of a FRAP bleach spot can be described as a function of a constant minus a Gaussian (Bryers and Drummond 1998), this is only true for spot sizes that are similar to the radius of the bleaching laser. For larger spots, a sigmoidal function can be employed instead. One option for a sigmoidal function is a cumulative function of a Gaussian, which will ensure that the sloped edges of the bleach will match the profile of the laser, but with a flat base near the centre as expected for a larger bleach ROI, which can be see in Fig. 6.1. This function is described as

$$I(r) = I_{-} + \frac{I_{\Delta}}{1 + \exp\left(m(r - r_e)\right)}, \tag{6.7}$$

where I_{-} is the intensity of the bleached ROI and I_{Δ} is the intensity difference inside and outside the bleached ROI. The parameter m describes the slope at the edge of the bleached region and r_e is the effective size of the bleach. In polar co-ordinates, r is defined as always positive so bleach profiles will need to be radial (2D, averages over concentric circles from bleach centre) rather than 1D lines bisecting the ROI.

All parameters can be simply extracted (using fitting techniques for r_e and linear interpolation or function fitting for $\tau_{1/2}$) that are required for Eq. 6.4 and the diffusion constant can be determined.

While using image analysis of FRAP is a simple and powerful tool for measuring diffusion, it does not always tell the whole story. Many biological systems are incredibly cramped, contain barriers or gates which restrict movement or have species with domains that extend outside of the cell (Saxton and Jacobson 1997; Schütz et al. 1997; Nicolau et al. 2007; Krapf 2015). PEN3 is membrane bound and has domains which extend outside of the membrane (Meyer et al. 2009), and as plants cells have cell walls, the extracellular domains of these membrane proteins may bump into the wall and affect its ability to diffuse freely. As secretion of PEN3 into the membrane involves the addition of mem-

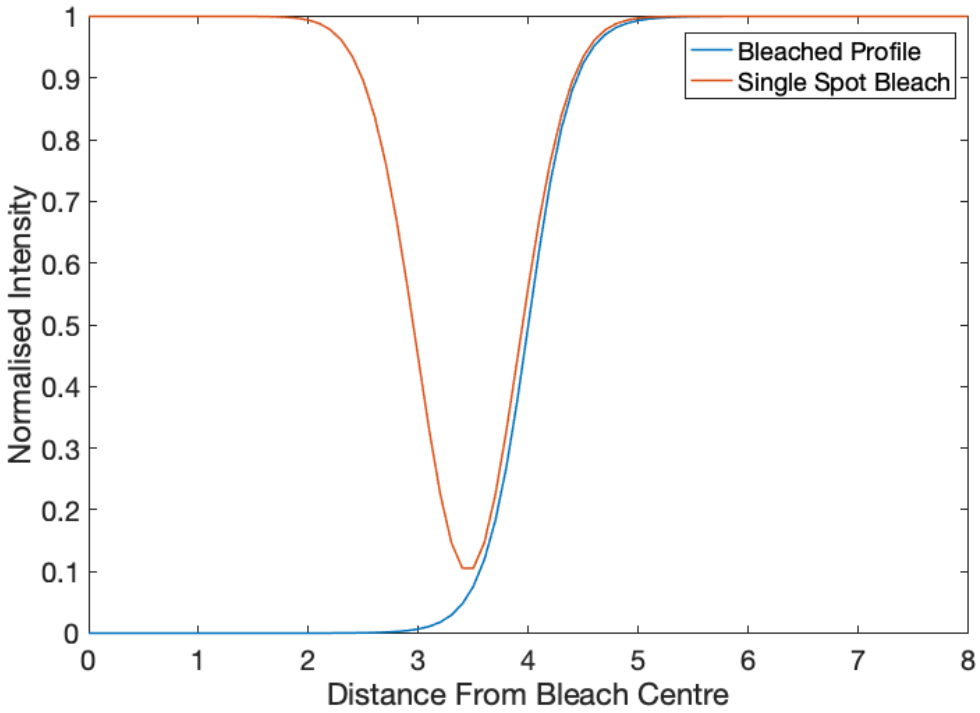

Figure 6.1: Sigmoidal Radial Bleach Profiles. By using a cumulative Gaussian to fit the bleach profile, the shape of the laser (with a Gaussian profile) is taken into account, while the flat bottom of a large bleach ROI is also present. The baseline of the bleached region is expected to be lower than the single spot bleach due to overlapping of the Gaussian tails as the bleach spot is moved.

brane material from vesicles into the PM, active external forces will likely also influence the movement of PEN3. These factors can result in the linear relationship between mean squared displacement and time no longer being true, therefore traditional FRAP methods are insufficient, thus the introduction of mathematical modelling can provide deeper insight into the movement and distribution of these key defence proteins.

More recent advances in mapping FRAP data to diffusion have enabled more detailed measurements of the diffusion constant, and even theoretically enable measurements of a time-dependent diffusion constant. By converting the equation which describes the fluorescence recovery over time (Kang et al. 2012) into a linear model, the resulting function $g(t)$ can give the half time of recovery using a single time point (Kang 2022). As can be seen from the equation,

$$g(t) = \frac{F_{\text{data}}(t) - F_0}{F_\infty - F_{\text{data}}(t)} = \frac{8D}{r_e^2(1+\gamma^2)}t, \tag{6.8}$$

where γ is r_n/r_e, this linear relationship becomes very susceptible to noise as $F(t) \to F_\infty$

as the denominator becomes very small, so the data used for the linear fit should be cut off before this happens. By noting that $g(t = \tau_{1/2}) = 1$ and $g(t = \tau_{2/3}) = 2$, you can cut the data at $t = \tau_{2/3}$, fit a linear model and use the single data point at $\tau_{1/2}$ to estimate D. The benefit of this method is that you can choose the cut off at any point, and use your data to calculate the diffusion constant at any point in time. Doing multiple linear fits and analysing at different time points gives information about any changes in D over time, which can be used to (given enough high-quality, low SNR data) estimate anomalous diffusion properties. This method still requires fitting of the bleach profile to estimate r_e, and requires a long enough imaging session to determine F_∞, which for very slow diffusive systems can lead to issues of photobleaching and phototoxicity.

All of the previously described methods rely on imprecisely fitting a diffusion profile, therefore estimating diffusion parameters can be prone to noise and errors. By exciting a fluorescent sample with patterned illumination and taking measurements in the spatial Fourier domain, knowledge of the post-bleach profile or the PSF are not required (Geiger et al. 2020). Fourier analysis in the spatial domain yields a single exponential decay for normal diffusion, and analysis of multiple harmonics over several length scales can provide information of anomalous diffusion parameters. This method can yield highly detailed and accurate estimates of diffusion parameters, but requires a complex, non-conventional microscopy assay which we do not have access to.

Several tools exist to analytically or numerically simulate diffusion and match it to experimental data (Schaff et al. 2009; Rapsomaniki et al. 2012; Blumenthal et al. 2015) but many are simplistic or prone to errors. PyFRAP has been developed and benchmarked against many of these available models, and showed significant improvements in accuracy on simulated data (Bläßle et al. 2018). One issue with this model, however, is that it assumes that D is constant over time. This makes it unsuitable for testing for anomalous diffusion, and therefore I had to develop software to numerically analyse our FRAP data.

6.2 Methods

6.2.1 Experimental Techniques

A. thaliana ecotype Columbia-0 (Col-0) with PEN3-GFP were grown as described in 3.2.1. As photobleaching can cause cell wall damage, and PEN3 is trafficked to these damaged sites, drugs which arrested myosin-mediated active transport (Pentabromopseudilin) and depolymerised the cytoskeleton (Latrunculin B) were used to ensure that any recovery of PEN3 in the bleach site was through membrane diffusion only. 30 minutes prior to imaging, each drug treatment was added to separate *A. thaliana* hypocotyls, at 10 mM concentration with DMSO, and a control with only 10 mM DMSO was also included.

To determine the parameters associated with diffusion, FRAP experiments were used alongside model fitting. The entire 5-day old plant was mounted with a standard glass slide and cover slip of thickness 0.13-0.17 μm. A spinning disc confocal microscope, with 60x lens and 1.35 NA (oil immersion) was used for image acquisition. A 488 nm laser set at 10.5 mW power was used to excite and image the PEN3-GFP with a 200 ms exposure. Stacks of 11 images with 0.55 μm separation were taken every 20 seconds for 15 minutes, immediately after a 20 pixel (~1.9 μm) radius photobleach event using an 405 nm laser at 30 mW power. This energy density was chosen to enable a clean bleach while removing or minimising any of the downstream changes associated with cell wall damage or phototoxicity.

As the FRAP region was circular and therefore rotationally symmetric, alongside the assumption that diffusion was consistent in all directions, radial distributions of the FRAP region were measured. This time series of images was projected in z (maximum z-projection) before being aligned in Fiji is just ImageJ (Fiji) program, using a rigid body transformation, to ensure the position of the FRAP region was constant. Due to the repeated imaging, a simple ratio photobleach correction was applied to the series of images also in Fiji. To determine the radial profile of the FRAP region, concentric circles with regular intervals in r had their mean intensities measured at every time point. These distributions were used as input and comparison to diffusion models in order to determine the parameters associated with diffusion.

6.2.2 Diffusion Model Fitting

As it is unknown whether diffusion of PEN3 in the membrane is based upon Fick's Law (Fick 1855), shown in Eq. 2.9, or whether the diffusion is anomalous, traditional methods of determining the diffusion constant through purely experimental means were insufficient. To overcome this, a diffusion model was built in which the initial conditions of a FRAP experiment could be used as a starting point. From here, each time step with an equivalent experimental time point for comparison was used to determine how well the model matched the data. A range of diffusion parameters were tested such that the best fitting parameters could be found.

Anomalous diffusion can be characterised by the parameter α describing the power relationship between mean squared displacement and time, seen in Eq. 2.10. Barriers, obstacles and cramped environments can result in $\alpha < 1$ which is known as subdiffusion, whereas active transport can result in superdiffusion with $\alpha > 1$. Modelling anomalous behaviour and fitting it to observations allows us to determine which diffusive regime the protein moves under, and to what degree. Anomalous diffusion is defined using a adapted version of 2.9 with fractional derivatives corresponding to the value of α, but these are very tricky to implement numerically and require knowledge of all previous time steps, which is highly memory intensive and not very physical. Instead, it is possible to just scale the diffusion constant in such a way that it produces the same result. At each time point, the coefficient of diffusion is updated to be

$$D = D_0 \alpha t^{\alpha - 1}, \tag{6.9}$$

were D_0 is the rate of diffusion at $t = 0$ seconds. You can see in Eq. 6.9 that for $\alpha = 1$ you obtain the standard diffusion constant $D = D_0$ again, as required.

The protein is membrane-bound and the FRAP region is circular, therefore the obvious choice of a co-ordinate system is 2D polar. Expanding the Laplacian on the right hand side of Eq. 2.9 and realising that the system is circularly symmetric (*i.e.* all derivatives in

angular terms are zero) yields,

$$\frac{\partial \rho(\vec{r},t)}{\partial t} = D\nabla^2\rho(\vec{r},t) = D\left(\frac{\partial^2\rho(\vec{r},t)}{\partial r^2} + \frac{1}{r}\frac{\partial \rho(\vec{r},t)}{\partial r}\right). \tag{6.10}$$

There are many options for converting the above into a numerical method, but one of the simplest and most common is the forward Euler method. This uses a forward step in time Δt and a central step in space Δr (FTCS) for the differentials. Rewriting Eq. 6.10 using FTCS results in,

$$\frac{\rho_r^{t+\Delta t} - \rho_r^t}{\Delta t} = D\left(\frac{\rho_{r-\Delta r}^t - 2\rho_r^t + \rho_{r+\Delta r}^t}{(\Delta r)^2} + \frac{\rho_{r+\Delta r}^t - \rho_{r-\Delta r}^t}{r(2\Delta r)}\right). \tag{6.11}$$

The central difference in space means that for the first-order partial differential term, concentrations either side of the current point are used and thus the distance between them is $2\Delta r$. Rearranging this to make the concentration at the new time point the subject of the equation gives,

$$\rho_r^{t+\Delta t} = \rho_r^t + D\Delta t\left(\frac{\rho_{r-\Delta r}^t - 2\rho_r^t + \rho_{r+\Delta r}^t}{(\Delta r)^2} + \frac{\rho_{r+\Delta r}^t - \rho_{r-\Delta r}^t}{r(2\Delta r)}\right), \tag{6.12}$$

which allows us to evolve the system through time given some starting conditions $\rho_r^{t=0}$ and compare to experimental results. The second term in the brackets is due to the system being 2D, and while it contributes close to the centre (where $r \approx \Delta r$) it quickly diminishes in size as r increases.

One limitation of the forward Euler method is stability. Both Δr and Δt have to be chosen in such a way as to maintain the following relation (Puwal and Roth 2007),

$$D\frac{\Delta t}{(\Delta r)^2} \leq 0.5. \tag{6.13}$$

This relationships shows that an increase in spatial resolution by a factor n (and thus a decrease in Δr by the same factor of n) requires an increase in temporal resolution of n^2. In our case, we are using experimental FRAP data as the start point and as points of comparison, therefore Δr is fixed by the resolution of the microscope and the pixel size of the CCD. This means Δt had to be chosen to be small enough for stability but also

needed to be a integer divisible value of the time step between sequential experimental data points, such that comparisons can be made. As we tested a range of values of D_0 and α, the largest value tested needed to still conform to Eq. 6.13.

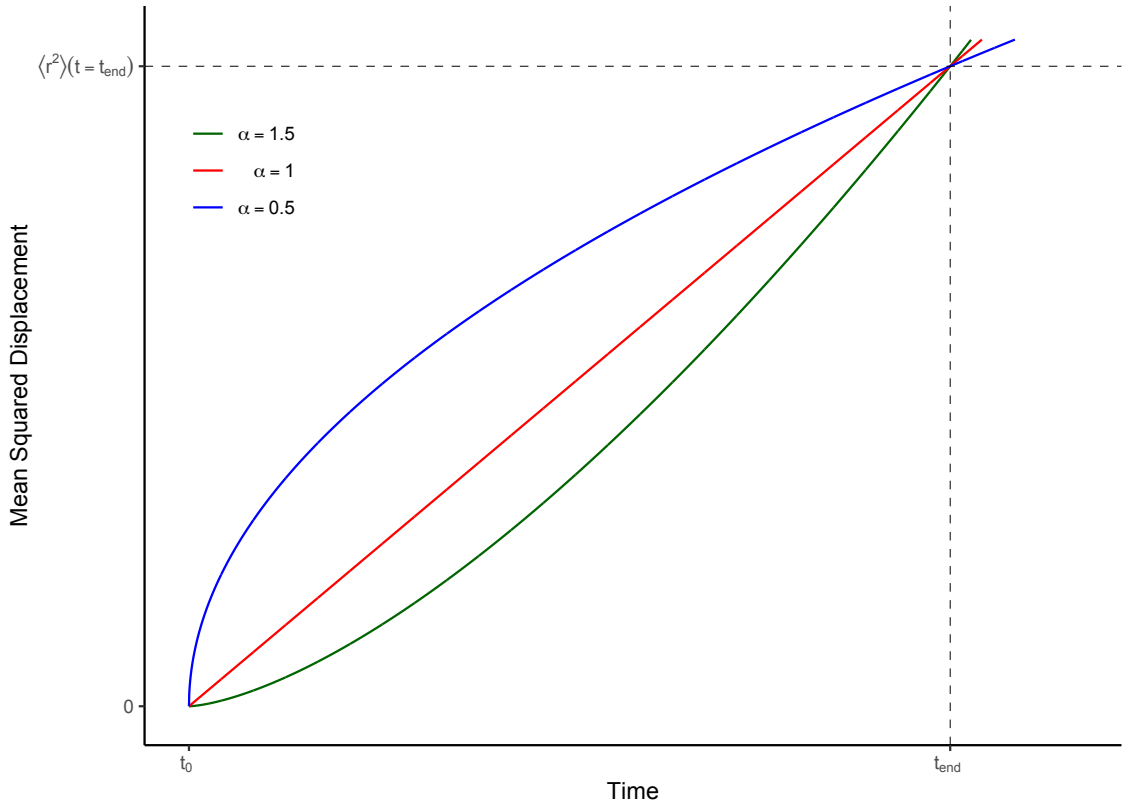

Figure 6.2: All roads lead to Rome. With identical starting conditions and only fitting to a single time point, there are an infinite number of pairs of α and D_0 which have a minimised fit. By fitting to additional time points, the chance of a significantly incorrect pairing having a minimised fit value decreases, therefore we fit to every time point we have available, each with equal weighting.

A range of values of D_0 and α were simulated (101 of each parameter for 10201 simulations in total for every FRAP experiment) using Eq. 6.12 in MATLAB. The starting distribution was taken from the first image post-bleach in the FRAP experiments, then the simulated distribution at each time point (*e.g.* $t = 20$ s, 40 s, ...) was compared to the distribution measured experimentally. The *fit*, which determined the quality of the parameter pairing, was measured as the sum of the difference in ρ at every position per time point, then summed over every time point. This ensured that every position and time point was weighted equally, as the changes in D due to α can otherwise introduce issues as shown in Fig. 6.2.

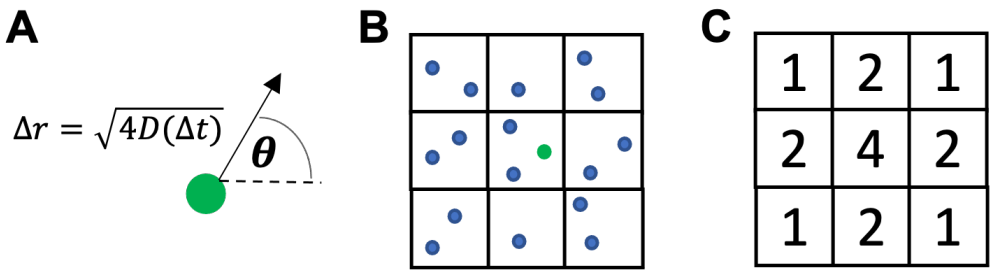

Figure 6.3: Diffusion and Imaging in ATIS. A) The distance Δr a membrane-bound protein travels in a given time step Δt is related to the diffusion coefficient D. The direction of travel is random, sampled from a uniform distribution of all possible angles in a circle, which yields Brownian motion. B) Each protein object is iterated through to determine which pixel it is located within, which is needed for exporting an image of the system. C) For the highlighted (green) protein in panel B, intensity values are added to the pixels in a 3x3 neighbourhood. For a Gaussian PSF of max intensity 4, the non-diagonal pixels have a rounded intensity of 2, and the diagonal pixels have a rounded intensity of 1. This is correct to the nearest integer, as the image being taken is 16-bit.

6.2.3 Modelling PEN3 in *A. thaliana*

In contrast to the distribution-based diffusion model used to determine the diffusion coefficient, the model of PEN3 transport and distribution in *A. thaliana* immune responses was particle based. This enabled trivial exchange of these proteins between the membrane and cytoplasmic stream populations as was required, and also removed the requirement of a rotationally symmetric 2D distributions which was no longer true. The *Arabidopsis thaliana* Immune Simulation (*At*IS) was built in C++17 due to the potential computational complexity and intensive memory requirements, and snapshots of various time points were exported to reflect the image acquisition process that would be undertaken experimentally. The code in its entirety can be found in Appendix A.

The *At*IS PEN3 model contained two distinct components and distributions: the protein in the membrane was free to diffuse (normally, $\alpha = 1$) in two dimensions, and the protein being actively transported within the cell was fixed in its drifting trajectory (referred to as the stream from now on). To model diffusion of individual particles, they were moved by a distance determined with Eq. 6.1 where $t = \Delta t$ (the size of the time step), and an angle randomly generated from the uniform distribution $[0, 2\pi)$, shown in Fig. 6.3A. While sampling the distance from a normal distribution with a mean from Eq. 6.1 may be more biologically accurate, this should yield near-identical distributions over our 20 minute time-scale.

A single stream of actively transported protein travels in a straight line along the length of the cell, intersecting or running proximal to the site of infection. The proteins are normally distributed perpendicular to this line of transport, and all move at a constant speed biologically estimated to be 5 $\mu m\, s^{-1}$, a typical speed for vesicular transport in *A. thaliana*. A zone of delivery, centred on the infection site, which was varied in order to explore the change to the size and shape of the PEN3 enrichment zone, was used for net transport of protein from the stream into the membrane. This delivery zone was highly customised through the use of various zone diameters, heterogeneous delivery probabilities and zones influenced by membrane conditions. Many options were tested and a homogeneous, circular zone with decreased probabilities based upon PEN3 membrane density was chosen as it is biologically sensible and produced visually appropriate results.

Each protein in the model was an object with various properties describing its position, fluorescent properties, and ability to diffuse. An array of these objects was stored for the membrane and a second array for the stream, such that these could be handled separately for movement without additional checks, and so that images with and without each component could be taken if desired. To image the system, a grid of pixels was drawn over the simulation, and every protein within each pixel contributed to increasing the intensity of the pixels in a 3x3 grid around them, as shown in Fig. 6.3 panels B and C respectively. Repeating this for every pixel produced a matrix of intensities, which was exported as a TIFF file using the TIFF library. Exporting the data as an image instead of a table or numbers enabled downstream processing pipelines to remain near identical to experimental data for qualitative and potential quantitative analysis.

Many of the parameters in the simulation associated with protein density and brightness are related due to the relative nature of the background and response regions of the cell. The density of the proteins in the membrane before any immune response is fairly irrelevant as the simulation has no interaction between them for diffusion. The requirement, based upon measurements in experimental data, was that the intensity of the response region was approximately two to three times greater than the cell background. While matching the intensity of these regions of the simulation to experimental data is possible and fairly trivial, such as through the use of an intensity gain or changing the

Name	Symbol	Value
Diffusion Constant	D_0	0.0025 µm^2 s^{-1}
Diffusion Regime	α	1.0
Background Concentration	ρ_{bg}	536 µm^{-2}
Stream Concentration	ρ_s	$1.29\rho_{bg}$ = 691 µm^{-2}
Stream Velocity	v_s	5 µm s^{-1}
Base Delivery Chance	Γ	0.651
Delivery Reduction Factor	λ_m	1.2
Protein Delivery Limit	L_p	100 s^{-1}
Pixel Size	l_{px}	0.095 µm
Peg Radius	R_p	$6l_{px}$ = 0.54 µm

Table 6.1: *At*IS Parameters. The parameters in the *At*IS model were either directly fitted or estimated from biological observations, with exceptions in the pixel size (determined by our microscope) and the peg radius (large enough to be visible without impacting the result significantly). Many of these parameters are related, therefore changing one would require refitting several others.

protein density, it was not required and the latter option would have a significant impact on computational time. For this reason, the chance for a protein to be delivered to the site of infection, by being transferred from the stream population to the membrane population, decreased as the protein density increases, through a relationship which achieved the two-to-three ratio of background to response that was required over the 20 minute period. The chance of a protein being delivered P_d to the membrane is

$$P_d = \Gamma e^{-\rho_m/\lambda_m}, \tag{6.14}$$

where ρ_m is the current, local density of proteins at the point of delivery, measured in µm^{-2}, and λ_m is the decay factor, modulating the decrease of delivery probability. Γ is a global scale factor which ensures that the stream doesn't immediately dump all its contents upon reaching the infection site. A limit to the total number of proteins that can be delivered every second is also applied, as in reality the delivery is not instantaneous and the resources for exocytosis are not infinite. For higher density backgrounds; however, these parameters will need to be adjusted.

While PEN3 can be produced during an immune response, it also undergoes endocytic recycling from the membrane to the site of infection. To mimic this removal far from the site of infection, any proteins which move beyond the edge of the simulation are removed.

A series of simulations were run in *At*IS with varied delivery zone diameters D_p which were chosen as a scale factor of the penetration peg size (1, 2.5, 4, 5.5), in order to explore whether delivery is localised to the infection site or whether a zone is designated through a signalling pathway. The stream was at a fixed angle of 4.72° below the horizontal (and cell) axis, but was shifted by the radius of the penetration peg $\pm R_p$ from passing through the centre of the delivery zone such that the effect of position and direction of the stream on the resultant distribution could be observed, especially for the smaller delivery zones. All parameters are shown in Tab. 6.1.

6.3 Results

6.3.1 Diffusion Model Fitting

The radial distributions of PEN3 FRAP regions were extracted at every time point and fed into the simulation, where the value of D_0 was tested in the range $[0.001, 0.011]$ $\mu m\, s^{-1}$ and α in the range $[0.75, 1.25]$, each with 101 different values. Those which had the best fit against the limit of the D_0 range were run again with extended limits, and this was done to increase overall throughput. The distribution of the D_0 and α parameter pairs is shown in Fig. 6.4A, where all drug treatments were similarly distributed, with a single pentabrompseudilin data point as an outlier in the lower left. The curved relationship between D_0 and α is expected, and this is further shown in Fig. 6.4B, where the contour plot of the fit parameter has a similar shape. Away from this dark band the fit rapidly becomes worse, therefore the point of best fit was highlighted with a white cross. This consistent, deep fitting valley, means that a smarter way of sampling various parameter value pairs, such as using a binary search algorithm or gradient based optimisation (Sancibrian et al. 2004), would significantly reduce search time without the risk of finding local minima.

The distributions of α across treatment groups is shown in Fig. 6.4C, with no significant differences found between these groups using ANOVA (p=0.379). To determine if any of the treatments had a mean α value different from 1, a students t-test was used for the DMSO and pentabromopseudilin groups, and the non-parametric Mann-Whitney test for latrunculin B treated samples (normality was tested for using the Shapiro Wilks test). Corrections were applied for repeated testing (see 2.2.2 for further details). None of

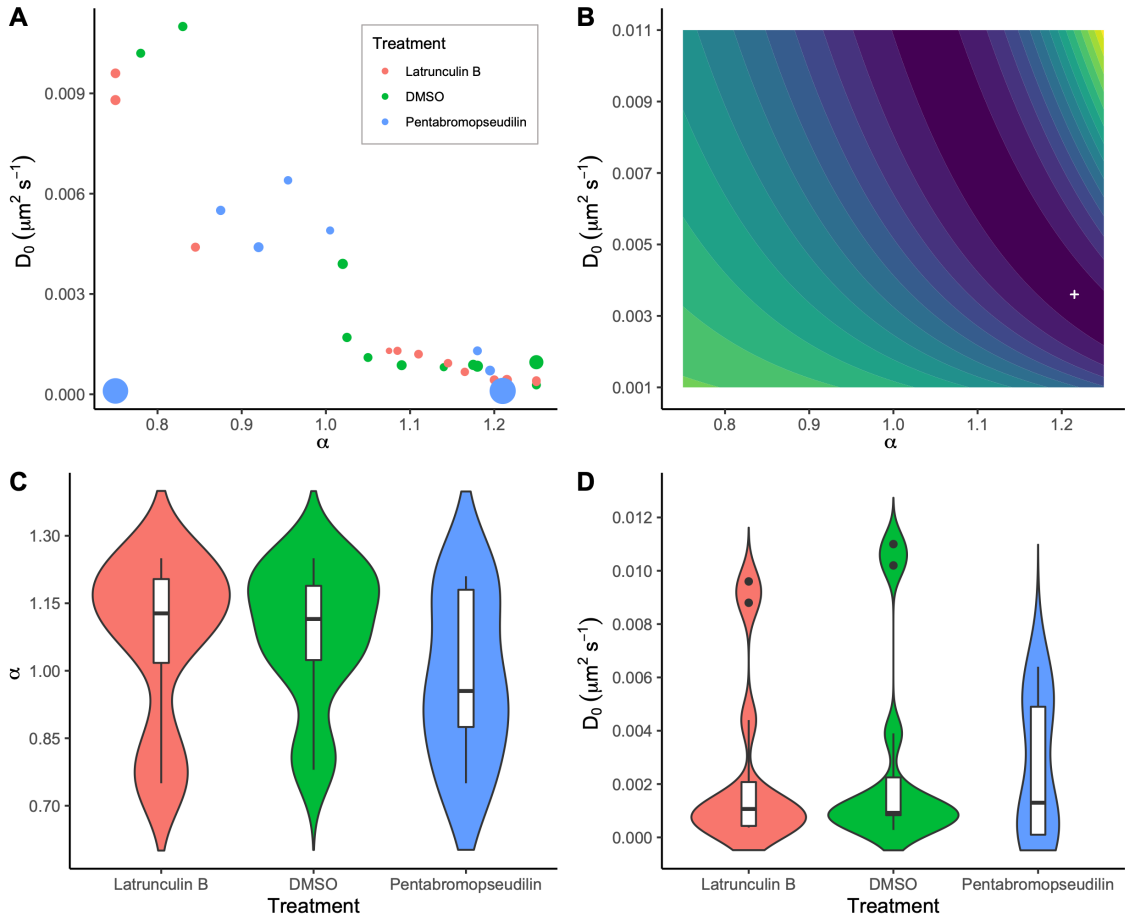

Figure 6.4: Fitting diffusion parameters to FRAP data. Control (DMSO, $n = 12$) *A. thaliana* cells were used alongside an actin depolymerising drug (Latrunculin B, $n = 12$) and a myosin inhibitor (pentabromopseudilin, $n = 12$) to determine the rate and modality of diffusion of PEN3 in the membrane. A) The simulated parameter pair (D_0 and α) which fit best to the experimental FRAP data. Smaller point sizes show a better (minimised) fit to the experimental data, further highlighting the issues with the outlier in pentabromopseudilin. B) A surface plot of the fitting parameter for one simulation of an experimental FRAP region. The better the fit parameter, the darker the colour, with the minimum (best fit) marked by a white cross. C) The distribution of α parameters across the three treatment groups, where no significance was found between groups or compared to a distribution with mean of one and variance the same as experimentally measured. D) The distribution of D_0 parameters, which also found no significant differences between groups. Statistical tests were performed using an ANOVA.

the treatments were found to have a mean α parameter significantly different to one with the same variance and a mean of 1.0, therefore in this instance we can assume a normal diffusive regime.

The D_0 parameter, shown in Fig. 6.4D, had no significant differences between treatment groups either. The latrunculin B treatment should have depolymerised the cytoskeleton, therefore cortical actin should not restrict movement of the membrane-bound PEN3 proteins. The lack of any difference in diffusive transport of the control and latrunculin B treated cells suggests that cortical actin does not provide a barrier to PEN3 diffu-

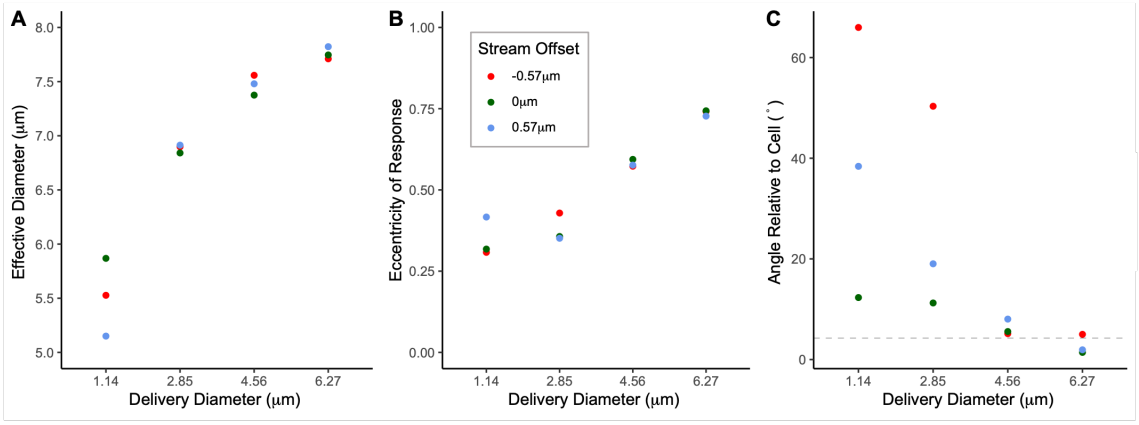

Figure 6.5: Artificial Simulation of the Immune Response. Each unique combination of delivery diameter and stream offset was run and analysed once, for a total sample size of 12. A) The effective diameter of the immune response for various delivery diameters, calculated as the geometric mean of the major and minor axis lengths of the ellipse fitted to the image. B) The eccentricity of the PEN3 response ellipse for various delivery diameters, calculated with Eq. 3.2. C) The angle the major axis of the fitted ellipse relative to the long axis of the cell. The horizontal dashed line represents the angle of the PEN3 delivery stream, which we hypothesised was a factor in the shape and orientation of response. Delivery diameters are chosen as multiples of the penetration peg radial size R_p = 6px = 0.57 µm

sion in the membrane, whereas these structures have been shown to influence membrane-bound proteins in animal cells (Andrews et al. 2008).

As the simulations resulted in a distribution of α not significantly different from a mean of 1, the simulations of PEN3 delivery and immune responses assumed normal diffusion, with a mean D_0 value of 0.0025 $\mu m^2 s^{-1}$, taken from the best fit with a fixed $\alpha = 1$. This mean was taken with just DMSO data, as it best reflects the environment and state of the cell we were simulating.

6.3.2 Modelling PEN3 Response

For consistency with my previous work, the *At*IS images at $t = 20$ minutes, obtained with the parameters in Tab. 6.1, were extracted and quantified with the same PEN3 response analysis pipeline, described in 3.2.2. The simulations were set up to have a 100% response frequency and the analysis pipeline was in agreement. The quantitative results are shown in Fig. 6.5 where changing the size of the PEN3 delivery zone was tested and compared to experimental data.

The size of the immune response increased with a larger delivery diameter, shown in Fig. 6.5A. Although all were larger than even the largest delivery diameter, suggesting

that diffusion does contribute to an increased disc size, but is not the only factor. All but one of the response sizes were within one standard deviation of the wildtype mean size found in 3.3, with the 0.57 μm offset of the small delivery diameter (1.14 μm) being below. While the threshold value of the analysis script was changed to be more appropriate for these data, the consistency of the simulation data outside of the response site, using the intensity distribution to determine a threshold is likely less appropriate here. The smaller delivery zones were much dimmer in their response, which is not seen experimentally, as we were testing this to an apparent non-realistic extreme, and therefore a fixed intensity value for the threshold may be more appropriate. The simulation was designed to target a certain density of PEN3 in the membrane before a response, therefore this region can easily be quantified and rejected, which is not true in reality. The stream offset had a more significant impact in the response size for the smallest delivery zone, which was to be expected as the stream proteins are distributed with a Gaussian distribution that has a standard deviation equal to the smallest delivery diameter. By offsetting the stream, much of it never passed through the delivery zone and reduced the response size. Experimentally; however, the stream is often not fixed and therefore this would likely have minimal influence on the result, and with larger (and more biologically relevant) delivery zones this is already the case.

The eccentricity of the response increased with the delivery diameter, shown in Fig. 6.5B, as might be expected given the width of the stream relative to the response region. Experimentally, the wildtype response eccentricity was 0.72±0.15, and for the largest delivery diameter, the mean eccentricity was approximately equal to this, with the smaller 4.56 μm delivery diameter just within one standard deviation below the mean. The two smallest delivery zones were significantly lower, which may suggest a larger delivery zone is present in these plant cells. There are many assumptions and simplifications in the delivery process; however, which may result in underestimations of the eccentricity. The issue with the threshold for measuring the response region may have also had an influence on the result.

The angle of the long axis of the response ellipse relative to the long axis of the cell is shown in Fig. 6.5C, with a decreasing difference in angle for larger delivery diameter.

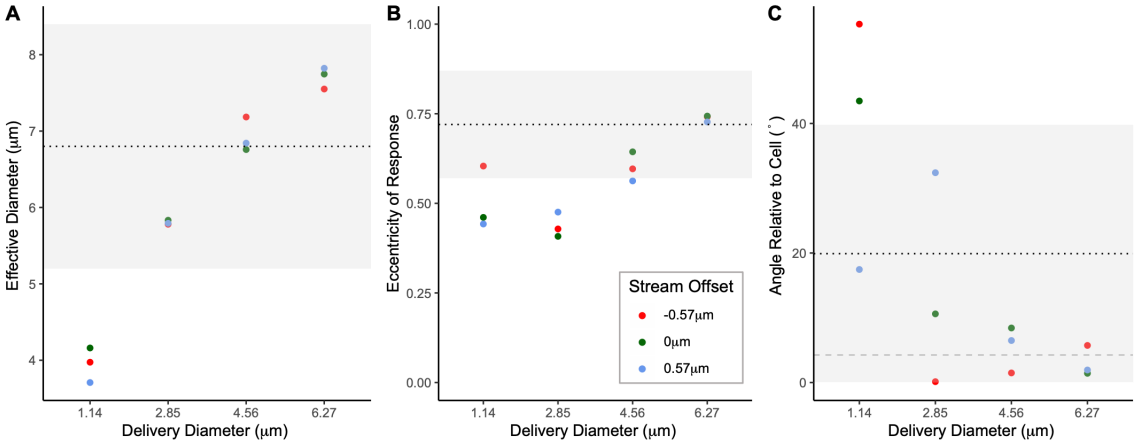

Figure 6.6: Reanalysis of *At*IS with updated thresholding. Each unique combination of delivery diameter and stream offset was run and analysed once, for a total sample size of 12. A comparison of *At*IS model outputs against experimental data, with the experimental mean being shown as a dashed line and one standard deviation being covered by the grey shading. A) The effective diameter of the PEN3 immune response shows that a small delivery zone is unlikely to be realistic, and this is backed up by the eccentricity of the response, found in (B). C) The orientation of the major axis of the response ellipse relative the to long axis of the cell. The dashed line shows the angle the delivery stream makes, and the larger, more eccentric responses tend to cluster around this angle.

The angle the stream makes relative to the cell is shown by the dashed line, with two largest delivery diameters having mean angles just above and just below this value. While the stream direction and orientation is likely in part responsible for the orientation of the response ellipse, the stream would normally move and change angle over the time period. Any initial offset between stream and cell angle is therefore likely to change and perhaps even disappear over extended time periods.

Due to the uniformity of the background signal of the *At*IS images, it was possible to alter the thresholding method to better detect the PEN3 response across the extremes being simulated. The model was designed to match the 2-3x increase in intensity for the PEN3 response region, therefore the threshold was adapted to be 2x the median of the background region and the analysis redone. The results are shown in Fig. 6.6, with a dotted line showing the mean experimentally measured value from 3.3, and the shaded region denoting one standard deviation from the mean. The dashed line in Fig. 6.6C, is the angle of the delivery stream, as is the case in Fig. 6.5C. From these results, it is clear that the smaller delivery zones are unlikely to be realistic. A delivery diameter of 4.56 µm appears to be best for predicting the effective size; however, this size underestimates the eccentricity of the response, while the 6.27 µm diameter is much better in this case. It is

therefore likely that the correct delivery diameter is somewhere in between these values, and a mean of 5.4 μm would be a sensible prediction based upon the simulations.

6.4 Discussion

Through the use of FRAP experiments and modelling, we were able to deduce that the diffusion regime of PEN3 in the membrane of *A. thaliana* epidermal hypocotyl cells was normal (Fickian) diffusion. Fitting the diffusion model to the data yielded the diffusion constant of 0.0025 $\mu m^2\,s^{-1}$ which we used in a model (*At*IS) of PEN3 in an immune response. *At*IS had several other parameters based upon biological observations, such as the velocity of actively transported PEN3 vesicles and the rate of delivery to the membrane, and all parameters are shown in Tab. 6.1. We tested various delivery diemeters and stream positions, running the simulation for 20 minutes such that the same downstream analysis from 3.2.2 could be used and the results were compared. The larger delivery zones resulted in increased response eccentricity and better alignment to the cell and the stream, which is seen experimentally. These larger zones gave response sizes that were between the mean and the upper bound of experimental sizes, however. Due to the nature of *At*IS, a change to the analysis method likely resulted in a more accurate representation of the response, but prior knowledge of current results and those in 3.3 made it difficult to not introduce bias for a desired outcome, although this was minimised by making choices based upon experimental data.

The properties of the plasma membrane, as well as the size of PEN3, resulted in the diffusion constant being small. A slower rate of diffusion makes conventional FRAP experiments difficult, as the time required to reach a steady state equilibrium of fluorescence is long, which can cause issues with photobleaching and phototoxicity, while also significantly reducing throughput. By fitting the experimental data to a model, throughput was increased and anomalous diffusion regimes could be tested. This should be applicable to any 2D diffusive system with rotational symmetry (*i.e.* Diffusion is uniform in all directions) and a circular bleach spot. For systems with unknown behaviour, an improved search algorithm for parameters would be beneficial, significantly reducing analysis time (~60-70 minutes for a single time-series with 101x101 parameter pairs), although limits

on D_0 and α would need to be imposed to ensure stability. This could be sidestepped by adjusting Δt based upon Eq. 6.13 and the current parameter pair, although it was decided that for consistency it was best to keep all other variables constant.

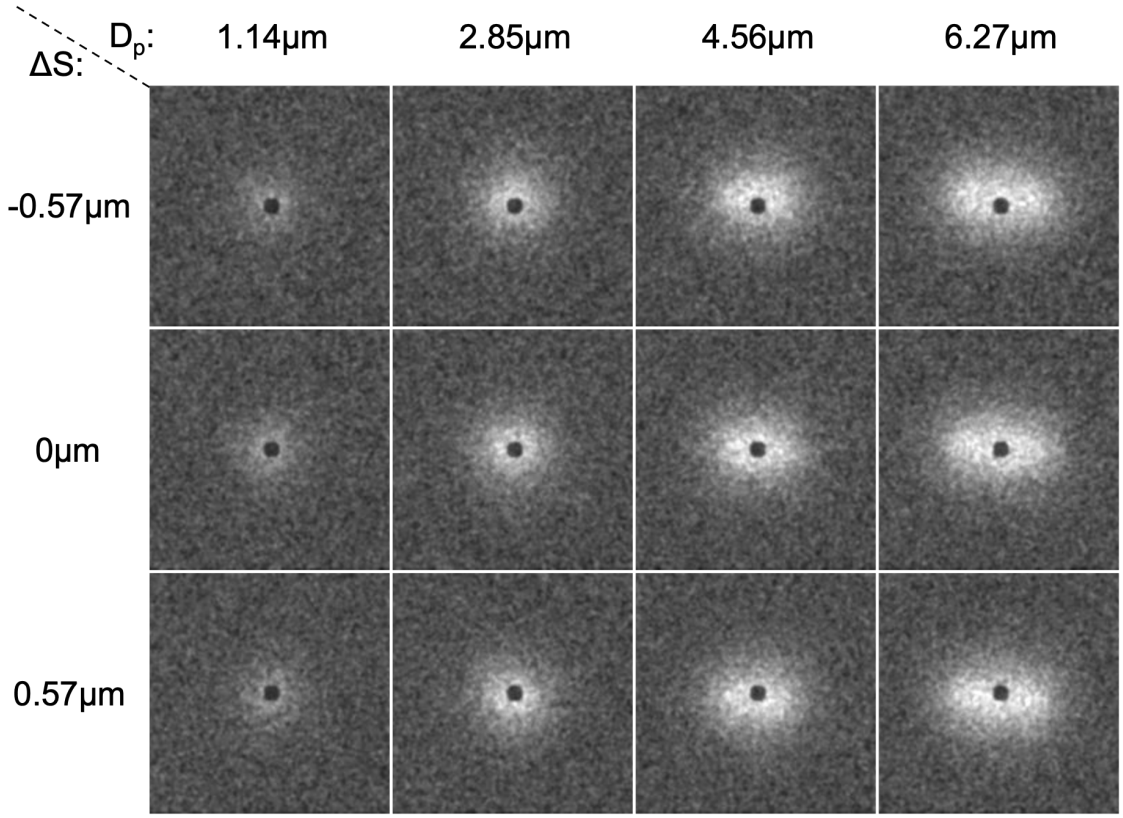

Figure 6.7: *At*IS images at t=20 minutes. Each unique combination of delivery diameter and stream offset was run and analysed once, for a total sample size of 12. The distributions of PEN3 around the penetration peg (represented by the dark region, 1.17 μm diameter) are influenced by the size of the delivery zone D_p and the position of the delivery stream. The offset of the stream from the centre of the peg ΔS shows the whole response region being shifted up when the stream is also shifted up (*e.g.* $\Delta S < 0$) and down when the stream is shifted down ($\Delta S > 0$). Larger delivery diameters result in increased eccentricity of the response region as well as brighter responses. The proteins which are in the stream are not fluorescing in this image as this can affect downstream analysis. The long axis of the cell is parallel to the horizontal axis.

The output images from *At*IS, which were analysed to give the results in Fig. 6.5, are shown in Fig. 6.7. The issues with using a percentile of the intensity distribution for thresholding the response region should be more apparent comparing between the smallest and largest delivery zones. Any choice of value will result in either overestimating the small distributions or underestimating the larger ones, therefore the same analysis method between experimental data and *At*IS could not be used. In order to make a prediction of the delivery zone size, the analysis method had to be adjusted. To minimise any bias of reanalysis, the new threshold was chosen based upon experimental observations and *At*IS design, and a quick visual inspection afterwards showed that it was appropriate. Due to

the issues the delivery stream can cause on this analysis method experimentally, shown in Fig. 3.7C, any proteins in the simulation which were in the stream were not included in the image. A quick test with the stream included showed that it impacted measurements for the smallest delivery zones, as expected.

6.5 Conclusion

A combination of FRAP experiments and diffusion model fitting enabled both the diffusion constant and the diffusive regime to be determined in *A. thaliana* hypocotyl epidermal cells. A simple, 2D simulation of the immune response to an artificial stimulus was developed, such that the distribution of PEN3 in the membrane could be explored and compared to the experimental findings in 3.3. Many of the parameters were explicitly fit to experimental data, while others were biologically appropriate estimates or determined relative to each other. The effect of various sizes of delivery zones was measured, and the outcome on both size and shape of distribution was quantified, alongside the effect of the position of the delivery stream. I found that a delivery zone smaller than the observed PEN3 enrichment size would be likely to reproduce our experimental results. This zone is still expected to be around 5.4 µm in diameter; however, which is approximately 80% of the observed PEN3 size and 64% of its area.

Chapter 7

General Discussion

Crops are a significant food and fuel source for most people, yet a changing climate and growing population requires an increase in the volume of crop produced all while using the same or even a reduced area of land. As large numbers of crops are lost to disease every year, much research has been done to produce crop genotypes with specific, host resistance, as well as the development of fungicides, pesticides and the like, but these solutions tend to be short-lived in the arms race between crop and pathogen. Plants have a basal immune response, which is non-specific and therefore is able to respond to a variety of pathogens, yet many of its mechanisms and pathways are not well understood. This research has begun to probe some of these mechanisms, particularly around the cytoskeleton and PEN3, in order to learn more about how plants defend themselves against the unknown.

7.1 Summary of Research

I have developed a novel method for stimulating the immune response of plant cells. By partially embedding microdiamonds into a thin layer of PMMA on the surface of a cover slip, small protrusions which exert localised pressure on the cell wall when the system was mounted on a microscope stimulated the initial stages of an immune response. This mimicked the physical aspect of a potential pathogen attack, and a common molecular pattern which included chitin, chitinase and drislase was added for the chemical compo-

nent. These aspects were combined to observe the initial 20 minutes of the plant immune response, and images were taken of *A. thaliana* PEN3-GFP fusion plant cells, such that the local PEN3 enrichment could be quantified. I developed an analysis pipeline for the PEN3-GFP images which would determine whether an immune response had occurred, as well as quantified the shape, size and orientation of this response. Similar response frequencies were found in the wildtype (Colombia-0) and an Arp2 loss-of-function mutant, whereas an increased number of responses was found in a Formin4/7/8 triple loss-of-function mutant. No differences were found across the wildtype or mutants in relation to the size of the PEN3 enrichment zone, its shape or its orientation relative to the cell long axis. To test the critical role the actin cytoskeleton plays in the immune response, the experiment was repeated with the addition of Latrunculin B 30 minutes before imaging, to depolymerise the network, and not a single immune response was observed.

With the knowledge that the cytoskeleton is vital for the initial stages of the plant immune response, I began to develop methods for extracting and quantifying this network. I imaged *A. thaliana* hypocotyl epidermal cells with GFP-Lifeact to develop the methods of segmenting the network from the rest of the cell. From here, I developed a method of labelling the different filaments and bundles, through the use of branch points and end points, such that each component of the network could be measured and quantified. I designed 17 different metrics for the network, spanning from filament lengths and branch angles to bundle widths and various curvatures. I designed various test cases to validate these different measures, with an aim to cover edge cases as well. I also designed a way to artificially generate simple data sets, with image properties akin to those from the microscope I use, including resolution and pixel size. These data sets had their filament density changed, as well as the noise levels, the threshold for network extraction and the numerical aperture of the lens used for imaging. Comparing to the ground truth, I quantified the sensitivity and precision of the algorithm at segmenting the network and highlighted the working range available without a single tweak to the code, in order to demonstrate how flexible the algorithm was.

Next, with the analysis algorithm—DRAGoN—developed and tested, I moved onto extracting and quantifying the network in various *A. thaliana* hypocotyl and leaf cells with

GFP-Lifeact. These cells had the same loss-of-function mutants as the previous PEN3 experiments, as these were designed to alter or impair the cytoskeleton. For the hypocotyl cells, four cytoskeleton metrics were significantly different between the wildtype and the *formin4/7/8* triple mutant, whereas only one was different for the *arp2-1* mutant. This is consistent with the findings in the PEN3 artificial immune stimulation experiments, where the formin triple mutant showed a slightly impaired immune response, whereas the *arp2-1* did not. It appears as if the combination of *formin4/7/8* loss-of-function has a more crippling impact on the cytoskeleton and therefore on the immune response (at least, in terms of PEN3 enrichment). Next, I compared between hypocotyl and leaf cells in *A. thaliana* to find a further four statistically different metrics, including network and branch point densities, which are perhaps a little more noticeable visually compared to the previous application. The ability of DRAGoN to discern both the obvious and more subtle differences is promising for future applications. Finally, it was applied to leaf cells which had been infected with *Bgh*; cells were chosen that were still alive and had clearly had a penetration attempt, so that the cytoskeleton would have had to locally remodel. Whole cell averages of the various metrics had to be taken, because artificially sampling smaller regions can introduce bias and place restrictions on certain properties of the network. Differences couldn't be detected using the specific metrics, but by applying principle component analysis a difference could be seen between infected and healthy cells, suggesting that using a subset of measures or a much larger data set is needed to see the changes. The remodelling due to infection is highly localised, so averaging over the whole cell means the shift is subtle, therefore a large amount of data is needed.

After correlation between the significant changes in the actin network and the PEN3 distribution of *A. thaliana* hypocotyl epidermal, I built a simulation to explore the shape and size of the PEN3 distribution further. Doing this required fitting several parameters associated with transport and delivery, and the key component was diffusion. Without knowledge of the diffusion regime (*e.g.* normal or anomalous), using conventional FRAP experiments wasn't possible and single particle tracking wasn't feasible. Instead, I built a circularly symmetric 2D distribution-based diffusion model in order to test the diffusion parameter and the regime. *A. thaliana* cells with PEN3-GFP had small, circular spots bleached and imaged every 20 seconds, while the model was given the starting bleach

distribution and simulated with over 10,000 different parameter pairs. The model was compared against the experimental images at every time point to determine the parameter pair with the closest fit. To ensure the bleaching laser had not damaged the cell wall and caused an immune response, wildtype cells were compared against those treated with Latrunculin B (an actin depolymerising drug) and pentabromopseudilin (a myosin inhibitor) to arrest PEN3 transport outside of membrane diffusion. No differences were found between treatments, and the regime was deemed to be normal, so the mean value of D_0 was calculated. With this, and measurements of the ratio between background and PEN3 response intensities, the basic model of PEN3 accumulation in the membrane was could be run. I used a single delivery stream of PEN3, with delivery probability decreasing as membrane concentration increased, to show that the size of the immune response increases with a larger delivery radius, using the same analysis pipeline as the previous PEN3 immune response research. Diffusion had contributed to the response size, as all responses were larger than the delivery zone size. The larger delivery zones; however, had eccentricity and response orientations which matched better to the experimental data, with PEN3 enrichment zones that were less than one standard deviation above the mean size. While this model was very simple and was based upon many assumptions, it suggests that the cells have a defined delivery zone, which may come from an upstream signalling molecule. An improved analysis pipeline, better suited to *At*IS data, was used to reanalyse the data such that a prediction of the delivery zone size could be made.

A combination of previous knowledge, findings and predictions from my research have been assembled into a simplified diagram of the immune response, shown in Fig. 7.1. Based upon analysis of PEN3 distributions and the rapid remodelling of the cytoskeleton under the infection site, I hypothesise at least one upstream signalling molecule designating the zone of remodelling and PEN3 delivery. This may be multiple molecules, or multiple pulses for the different phases, but the first would likely occur near instantaneously after peg pressure. It is also unknown whether the signalling molecule would occupy the cytosol or the apoplastic space. The shortest time of experimental assembly (*i.e.* initial peg contact) to imaging of the artificial peg assay that I was able to achieve was 26 seconds, and the cytoskeleton had already undergone significant remodelling below the site of infection. Although it remains dynamic after this, the largest changes had

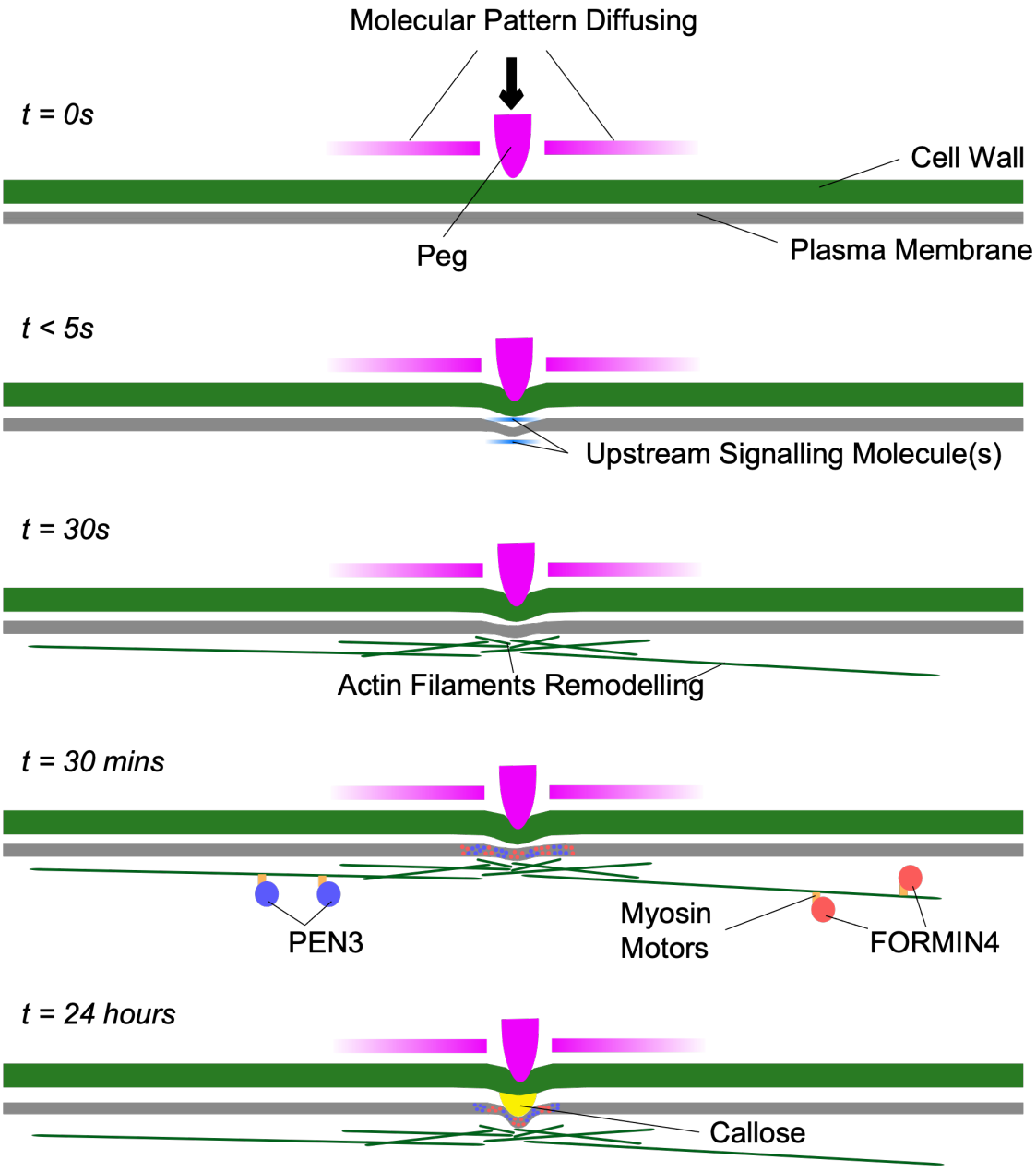

Figure 7.1: Immune Response Summary. This simplified overview is made from combining previous knowledge and results across my research. Observation of actin filaments reacting to a physical stimulus visually revealed that actin remodelling can occur within 30 seconds or less. Various analyses of PEN3 have resulted in an at least one upstream signalling delivery molecule being hypothesised to designate delivery of PEN3 and perhaps other immune proteins.

already occurred, therefore upstream signalling is likely to occur within a few seconds. After approximately 30 minutes, we know that PEN3 has been enriched at the infection site, and FORMIN4 also gets delivered, the two proteins occupying separate domains. A full, successful response often sees a callose deposit forming in the apoplast.

7.2 Spanning Disciplines and Techniques

I have explored various aspects of the immune response in *A. thaliana* using novel experimental techniques as well as in depth image analysis and modelling. It is clear that the initial stages of the response to suspected pathogens are heavily reliant on the dynamics and remodelling of the actin cytoskeleton in order to achieve timely delivery of key defence proteins. My network extraction tool has provided greater insight into properties of the cytoskeleton than was previously available. The interaction between the cytoskeleton and PEN3 vesicles has been shown to give rise to some of the properties of the PEN3 enrichment zone, but additional signalling molecules are possibly responsible for the shape and size of this response.

Combining mathematics, physics, biology, experiments and modelling has proven fruitful for exploring the early stages of a plant immune response. Several aspects of my work would have been prohibitively difficult or even near-impossible without being able to model the system, whereas the models would've been useless without relying on experimental data and observations. The feedback between modelling and experiments, shown in Fig. 7.2, is mutually beneficial and often results in knowledge greater than the sum of its parts. By doing both components myself, the model building forces me to formulate hypotheses and design experiments more carefully, such that outcomes can be properly quantified and tested. Interacting with the biological system and trying to image it enables a better understanding of the underlying science, which aids in framing any models in a more biological context, often resulting in a more useful model. Using a mathematical background and perspective on the system enables me to quantify the data and any outcomes in a more robust and repeatable manner, a critical facet of any research. Controlling every aspect of my work also gives me assurance in the models I build and the direction it takes me.

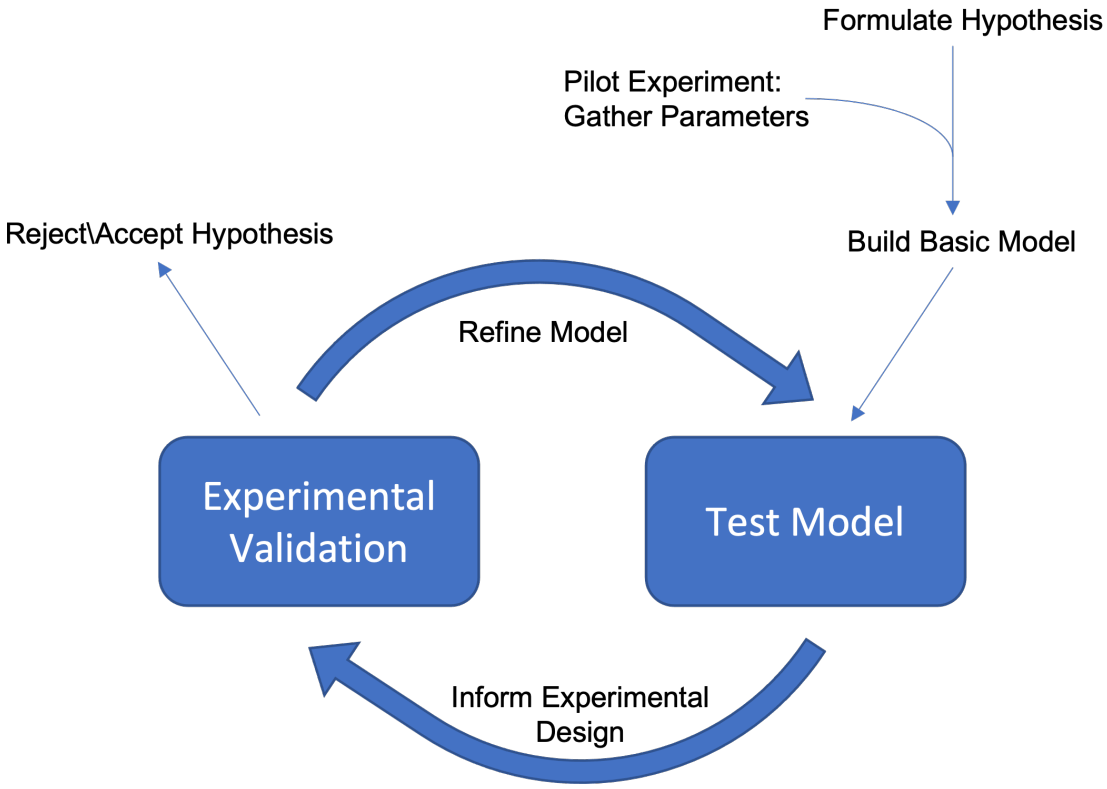

Figure 7.2: Experiment-Modelling Cycle. With a pilot experiment (or previous knowledge) and a hypothesis, a model can be built and used to explore the hypothesis. Knowledge gained from this can be used to improve experiment design as well as hone in on the aspects of the system that need to be tested. The results gathered from experimentation can be used to improve the model, in terms of parameters, design, and mechanics, which can again give direction to further experimental design. The feedback can be used to explore and test multiple hypotheses, while the model can be used to determine which new hypotheses to test in a much shorter time scale than could be done experimentally.

7.3 Next Steps

Our understanding of the basal immune response in plants is severely lacking, and while my work has begun to probe deeper into certain aspects of it, much still remains unknown. With the ability to analyse the shape of the PEN3 response, one possible aspect to observe is the way this region grows, looking at how its size, shape and intensity changes over time. If the delivery zone is designated through an upstream signalling molecule, then perhaps the shape and size of the zone will change over time as these molecules diffuse, or as additional signalling pulses are received. High temporal resolution data could elucidate aspects of this, and this is likely to provide better insight into the PEN3 enrichment process, which would be useful to improve the delivery mechanisms in *At*IS, especially Eq. 6.14. We had observed that multiple, simultaneous focal responses could occur, therefore it would be interesting to explore if there is a minimum separation required between

responses, or if the responses are different when the cell is dealing with more than one compared to dealing with a single one. Extending beyond 20 minutes may see this region grow larger, remain in a state of equilibrium, or perhaps even reduce as the physical pressure from the microdiamond has decreased (after the initial 'punch'). For significantly longer observations, the differences between the artificial and natural immune responses are likely to increase significantly, as a pathogen will fight back using an arsenal of effector proteins, as opposed to a static, inert peg. For cells with a clearly visible delivery stream, using a kymograph or any other method to analyse the stream direction and orientation compared to the cell axis could provide insight into the orientation of the immune response, as the *At*IS response aligned with stream direction. As PEN3 undergoes endocytotic recycling, it is possible that equilibrium is established and there is a constant turnover of PEN3 at the infection site. A photoswitching fluorescent protein could be used to observe this, by switching fluorescence and observing if PEN3 diffuses away or is recycled. The *At*IS model already has the ability for FRAP or photoswitching experiments, so this could emulated or order to be able to accurately quantify any endocytotic recycling.

Several other proteins are localised to the infection site, including FORMIN4, so the same experimental setup and analysis pipeline could be used for FORMIN4-GFP cells. It has been shown that FORMIN4 and PEN3 occupy distinct nanodomains (Sassmann et al. 2018), so any differences in the shape or size could prove insightful, and a dual labelled line would be able to achieve that. Any differences could be attributed to a different signalling molecule used to designate the delivery zone, which may be expected considering the segregation of the proteins on the membrane. A different signalling molecule may be required for temporally separated signals or unique signalling pathways. Unpublished data shows that FORMIN4 is transported with a similar mechanism to PEN3, supporting (Sassmann et al. 2018), and while it doesn't arrive before PEN3, it is still not known whether its delivery is on a similar time scale to PEN3. The increase in membrane intensity is proportionally similar to PEN3, albeit just a much dimmer signal in general. As FORMIN4 is also a membrane-bound protein, the methods used to quantify the diffusion constant of PEN3 and simulate its accumulation in the membrane should be reusable, albeit with a different set of parameters.

A whole host of additional experiments that use the DRAGoN algorithm were discussed in 5.3, as well as potential algorithm development to extract more data relating to the cytoskeleton. Perhaps the most pertinent of those, in the context of the rest of the work discussed here, is using more high-throughput methods of stimulating the immune response to generate significant amounts of data where the network has been locally disrupted. Artificially stimulating the immune response with the microdiamond cover slip assay from 3.2.1 with GFP-Lifeact *A. thaliana* cells would remove some of the complexity and variability of using multiple organisms, and would also likely eliminate the issue of the cell hypersensitive response which plagued the *Bgh* experiments. The increased throughput and potentially improved consistency would likely yield a significant increase in statistical power. While it would not enable the quantification of the network in more mature responses, knowledge of the changes 1-20 minutes after contact may provide additional insight into PEN3 and FORMIN4 transport, as well as any other immune response proteins. Quantifying the changes across multiple time points would likely benefit from data with a high temporal resolution and a very large data set, where filament tracking could be implemented, such that changes to both the whole network and individual filaments or structures could be quantified.

One of the major limitations of *At*IS was the simplified delivery stream, with its fixed position and fairly uniform protein density. One improvement in this area would be to have a more complex network for transport, where the delivery stream has directional choices to make at branched regions. Even with a static network, this would add a degree of variability and randomness to the protein delivery that would be a more realistic experience, as long as the network had realistic properties. Using DRAGoN in the context discussed above, a distribution of network parameters could be determined, and *At*IS could be extended to generate a transport network which fits those parameter distributions. It could also be simplified to only include bundles with sufficient capacity for endosome transport. While it would not be representative at $t = 0$, the network remodels in response to a physical stimulus within seconds, therefore it should be fairly representative for most of the simulation. Using DRAGoN with high temporal resolution data could provide insight into the changes which the network undergoes, but as discussed previously, a large volume of data would be needed and it would add additional

complexity to *At*IS while likely not providing significant additional insight. Moving *At*IS beyond hypocotyl cells should be feasible, as the cell is currently just given boundaries of a rectangle, although it was designed with hypocotyl cells in mind and therefore some assumptions may have been made.

7.4 Long-Term Research

While scientific innovation has driven advancements in technology, the reverse is also true; improvements to spatial and temporal resolutions, gene editing techniques, and computational power, amongst a plethora of other technologies, has pushed the boundaries of knowledge in science forwards. As PEN3 is membrane bound, it is transported in the membrane of endosomes, and is meant to be deposited into the membrane through exocytosis. The limited axial resolution in confocal microscopy makes it almost impossible to discern between a cluster of PEN3 in the membrane, a cluster of PEN3 endosomes partially fused to the membrane, and a cluster of PEN3 endosomes bouncing between the membrane and the cortical actin in the cytoskeleton. It may be possible to see more detail of these membrane structures using a series of light sheet fluorescent microscopy (LSCM) images with the angle of the light sheet rotated, then using computational methods to achieve a single, higher resolution reconstructed image (Huisken and Stainier 2007). TIRF microscopy can enable high resolution images of membrane structures, but the additional thickness of our microdiamond cover slips, or the presence of a pathogen on the cell wall will likely result in a minuscule field of view, or a system too far from the cover slip surface to be imaged effectively. Many of the super resolution techniques require either fixation, and therefore the dynamics cannot be observed, or can use high enough laser power to induce phototoxicity or cell wall damage, interrupting the dynamics.

While PEN3 and FORMIN4 have similar transport mechanisms, and perhaps delivery timing, they do not share vesicles and are localised in a distinct manner (Sassmann et al. 2018). The differences do not end there: PEN3 is distributed in the membrane always and is localised mainly through endocytotic recycling, whereas FORMIN4 is under tight transcription control. Several organelles are transported closer to the site of infection to reduce trafficking time, and it is possible that FORMIN4 is translated either on site or

in close proximity, and the vesicles of FORMIN4 are just those that have not localised to the membrane. Tracking of vesicles or the use of a photoswitching fluorescent dye may enable further insight into the mechanisms of FORMIN4.

I explored PEN3 diffusion while using Latrunculin B and Pentabromopseudilin at a fixed concentration based upon previous research, and the Latrunculin was also used to show that the cytoskeleton was vital in PEN3 transport to the site of infection. Using an additional suite of drug treatments, such as those which inhibit certain signalling pathways, cytoskeletal activity or transport mechanisms may provide additional insight into the initial stages of the immune response. A microfluidics assay would enable imaging of the system before, during and after a washout drug treatment, which could be used to temporarily interrupt signalling pathways or transport mechanisms in order to probe for critical pathways in the immune response. It can be seen that high concentrations of latrunculin B can freeze the cytoskeleton in place almost immediately, before causing it to snap due to network tension, therefore altering the concentration over time may enable allow better control of various mechanisms and cellular functions without wasting time on trial-and-error.

Some pathogen effectors have been shown to target vesicle trafficking pathways (Personnic et al. 2016) in order to influence or break the recycling or early and late endosomes which are shuttled between the *trans*-Golgi network and endoplasmic reticulum. The loss of key defence proteins (*e.g.* PEN3) can make a plant cell much more susceptible to pathogen entry, and therefore a better understanding of the pathogenic manipulation of critical signalling and trafficking pathways could aid in improving plant defence systems. Including these effectors, at various concentrations, in the microdiamond assay could be used to see which transport pathways are effected and by how much.

The diamond assay has shown that the plant is able to respond, at least initially, to multiple potential sites of infection simultaneously. These responses visually appear to have no discernible difference from a typical, single-site response, for the 20 minute time frame observed. It would be interesting and insightful to pursue this further, to determine the number of simultaneous responses a cell could handle before having to give priority to some. Exploring how close to adjacent sites of infection have to be before they are treated

as one may also be interesting, or if that would ever happen. By tagging key organelles, such as mitochondria or the Golgi, and observing which sites these organelles travel to, would perhaps show the cell prioritising certain responses, and determining how it does this would be important in gaining further insight into the signalling systems the plant deploys in an immune response.

The PEN1-3 genes have been hypothesised to rely on a defence pathway that functionally overlaps with the MLO-based (Mildew Resistance locus o) powdery mildew resistance (Humphry et al. 2006). Loss-of-function mutants in MLO have broad-spectrum resistance to nearly every known *Bgh* isolate (Acevedo-Garcia et al. 2014). These mutant alleles have been bred and used for more than 40 years, significantly longer than any specific induced R gene resistance. MLO appears to calm the immune response of plant cells, and powdery mildew has been found to exploit this; without this pathway, the pathogen is unable to colonise the cell, and a lack of MLO results in upregulation of myosin, a key protein in the trafficking of defence proteins during an immune response. Exploring the role of MLO further, including how it determines when and how to modulate aspects of the immune response and how pathogens are able to manipulate that, could result in conferring resistance to other pathogens.

Many of the aspects of the immune response both explored and discussed so far are downstream of some of the initial signalling molecules. One perplexing aspect of signalling pathways in plant cells is the ability for calcium (Ca^{2+}) to enable and control a vast array of downstream effects. It would be insightful to explore the activation, transport and diffusive nature of Ca^{2+} in response to the diamond assay, if it is involved at all; other signalling candidates are most likely reactive oxygen species (ROS) such as H_2O_2, or amino acids such as glutamate. Combining measurements of the timing, size, and shape of the signalling molecule, through the use of an appropriate biosensor, alongside the same measurements of PEN3 transport and distribution could provide knowledge of the required upstream signalling molecule. It would also inform us of the delivery site size, a key component of *At*IS.

7.5 Wider Impact of This Research

We are currently living in a time of significant population growth, which reached over 8 billion worldwide in recent weeks, as well as a global climate emergency. Together, these phenomena are a threat to food security, not just with increased weather extremes such as floods and droughts, but through the movement of pathogens. Even with many high throughput genetic technologies and vast amounts of plant pathology knowledge, many of the techniques which protect our crops are regularly and repeatedly beaten by evolving pests. Exploring the plant basal response to pathogens, learning how they deal with new and unknown threats, gives us a chance to discover how to better adapt to these accelerating changes.

Not only has my research explored some of these defence pathways in more detail, but I have developed assays, software and algorithms which are able to probe and quantify different systems. This ability to quantify changes and analyse specific behaviour in response to pathogens enables a better understanding of the basal response, and will hopefully continue to provide insight in the future.

Chapter 8

Conclusions

8.1 Summary

As populations grow and temperatures rise, the demand for food across the world continues to increase. Plant pathogens continue to wreck havoc on crops, resulting in billions of pounds of lost crop every year. Global food security will not be possible without finding ways to better protect the worlds crops from disease, and the use of specific genetic resistance only provides short-lived relief from a single pathogen. The basal, generic resistance pathways in plants is not well understood, but may provide a long-term, robust method of reducing disease incidence in crops.

I have helped to develop a novel assay to probe the immune response of plant cells, without the use of pathogens, in such a way that the physical and chemical aspects of the immune response could be studied. This was used to look at the accumulation of PEN3, a key immune defence protein, in the membrane surrounding a physical stimulus. I have quantified several aspects of this response, 20 minutes after contact was made, to show that this method works, and that the response is consistent in a couple different loss-of-function mutants responsible for cytoskeletal development.

The cytoskeleton has been shown to be key in transporting immune defence proteins to the site of infection, and we showed this was the case. I developed a new algorithm which segments images of the cytoskeletal network and measures a range of its properties.

I used this algorithm to highlight the exact differences in the loss-of-function mutants from the PEN3 experiments. It was also able to detect a subtle difference in the network after infection with a powdery mildew, albeit with less precision.

With the knowledge of the cytoskeleton and the PEN3 response, I built a simulation of the first 20 minutes of this response; microscopy-like images were taken at 20 minutes after infection such that a comparison could be made to my initial experiments. This was achieved by measuring several key biological parameters of the system, such as the diffusion constant, through the combination of experiments and modelling. The size of the region for which PEN3 could be added to the membrane was varied, in order to estimate the presence and distribution of an upstream signalling molecule.

8.2 Future Steps

Almost every aspect of my work could be extended; the simulations of PEN3 in the membrane would benefit from a much better description of the cytoskeleton, which can be achieved with my network extraction algorithm. Many of the methods and simulations used could be extended to other immune proteins, especially membrane bound proteins such as FORMIN4. It would be interesting to move away from the model organism *A. thaliana* and test these findings in some key crops as it is likely these systems will be more complex. While much of the interest was focused on the initial stages of the immune response, the upstream signalling mechanisms, which trigger the cytoskeleton remodelling and transport of PEN3, are still unknown, and therefore exploring this might prove insightful.

8.3 Concluding Remarks

I am hopeful that not only will my research and findings on PEN3 and the cytoskeleton prove useful, but the methodologies and algorithms will be beneficial to others too. My network extraction algorithm is open source, and measures the network to a much greater detail than was previously available, therefore it will likely be beneficial as a tool or even inspiration to others in the field. Experiments and analyses were designed with quantifi-

cation in mind; I hope that this will aid reproducibility and clarity in my results, as well as provide tools to better test, compare and quantify immune responses in future.

Appendix A

Arabidopsis Thaliana Immune Simulation - *At*IS

Here I present every file from the *A. thaliana* Immune Simulation (*At*IS). During development, at least two to three years prior to thesis submission, unit tests were performed with Google's gtest system. Recompiling now required adjusting how this works, due to updates as well as changes to MacOS, and therefore the unit testing code has been commented out. No functional differences were added in this time, just the alteration of parameters that required recompiling the program.

A.1 *At*IS Parameters, Main and Enumerators

EnumFlags.hpp:

```
1 //
2 // Created by Jordan Hembrow on 2019-03-18.
3 //
4
5 #ifndef ATIMMUNESIMULATION_ENUMFLAGS_H
6 #define ATIMMUNESIMULATION_ENUMFLAGS_H
7
8
```

```
typedef enum coords{X, Y, N_COORDS} Coords;
typedef enum bleachstate{BLEACHED, RED, GREEN} BleachState;
typedef enum mobility{FIXED, FREE} Mobility;

#endif //ATIMMUNESIMULATION_ENUMFLAGS_H
```

Parameters.hpp:

```
//
// Created by Jordan Hembrow on 2019-03-18.
//

#ifndef ATIMMUNESIMULATION_PARAMETERS_HPP
#define ATIMMUNESIMULATION_PARAMETERS_HPP

#include <cmath>
#include <tiffio.hxx>
#include <array>
#include <EnumFlags.hpp>

const double diffusion_const = 0.0025;   //measured experimentally
const int time_to_run = (20*60); // (10*60) + (20*60);
const double DT = 0.2;

const int px_width = 696;
const int px_height = 1040/6;
const double img_width = 66.12;
const double img_height = 98.79/6.0;
const std::array<double, N_COORDS> micron_to_px = {px_width/img_width, ↩
    px_height/img_height};
const double px_to_micron = 2.0/(micron_to_px[X] + micron_to_px[Y]);

const double movement_per_step = sqrt(N_COORDS*2.0*diffusion_const*DT);
//const unsigned int bleach_r_px = 17;
const unsigned int bleach_r_px = 50;
const unsigned int FRAP_time = (20*60);
//const unsigned int steps_per_img = 5/DT;
```

```
29 const unsigned int steps_per_img = 30/DT;
30 const std::array<unsigned int, N_COORDS> peg_pos = {px_width/2, px_height↩
       /2};
31
32 const std::array<unsigned int, N_COORDS> stream_start = {0, 60};
33 const int global_stream_shift = 0;    // px shift of stream from ↩
       appressorium centre
34 const double stream_vel = 5.0;          //um per second
35 const unsigned int stream_width = 5;
36 const unsigned int stream_delivery_rate = 100;    //proteins per second
37 //const std::array<double, N_COORDS> stream_delivery_stddev = {2*6*↩
       px_to_micron, 2*6*px_to_micron};
38 const std::array<double, N_COORDS> stream_delivery_stddev = {9*px_to_micron,↩
        3*px_to_micron};
39 //const std::array<double, N_COORDS> stream_delivery_centre = {img_width/2.0↩
        + 0.5, img_height/2.0};
40 const std::array<double, N_COORDS> stream_delivery_centre = {img_width/2.0, ↩
       img_height/2.0};
41 const double reduction_per_proteins = 1.2;        //If there are this many ↩
       proteins in a pixel, reduce the chance of delivery by 50%
42 const double stream_delivery_radius = 1.0; // size of delivery radius, ↩
       scaled by peg size
43
44 /* Protein Concentrations (pc) in number per sq_microns */
45 const double pc_cytoplasm = 3.5*153.1;
46 //const double pc_stream    = 0.1;
47 const double pc_stream    = 1.29*pc_cytoplasm;
48
49 /* Image Settings */
50 const uint16 bits_per_sample = 16;
51 const uint16 samples_per_pixel = 1;
52 const uint16 photometric = 1;
53 const uint16 intensity_gain = 1;
54
55 const bool show_peg = true;
56 const unsigned int peg_rad_px = 6;
57 const int peg_light_attenuation = 3;   // only 1/3rd of light gets through ↩
       the artificial peg
```

```
58
59 const std::array<unsigned int, N_COORDS> upstream_bleach = {peg_pos[X]/2 - ↩
       25, peg_pos[Y]-15};
60 const std::array<unsigned int, N_COORDS> downstream_bleach = {3*peg_pos[X]/2↩
        + 25, peg_pos[Y]+15};
61 const unsigned int radial_dist_size = 50;
62
63 #endif //ATIMMUNESIMULATION_PARAMETERS_H
```

main.cpp:

```
1 // TODO: Separate Stream proteins completely such that I can easily add a ↩
      second stream
2 //  -> Sort of done but also lots of functions require a single stream (and ↩
      one stream angle?)
3 // TODO: Add FRIEND_TEST() to the header files of classes to allow testing ↩
      of private functions
4 //  -> Avoid as much as possible, but sometimes this is required
5
6
7 #define DEBUG_ON false
8 #if !DEBUG_ON
9 #define unitTests(...);
10 #endif
11
12
13 #include <iostream>
14 #include <Proteins/Proteins.hpp>
15 #include <Imaging/Img.hpp>
16 #include <Transport/Transport.hpp>
17 #include <RadialDistribution/Radial.hpp>
18 #include <vector>
19 //#include <UnitTest.hpp>
20
21
22 int main(int argv, char *argc[]) {
23     //if(unitTests(argv, argc)) std::cout << "Unit test(s) failed." << std::↩
```

```
        endl;
24    std::vector<Proteins> membrane, stream;
25    const double stream_ang = Transport::setupSystem(membrane, stream);
26    Radial::getDists(Img::TakeImage(membrane, stream, 0), 0);
27
28    const auto t_max = (unsigned int)(time_to_run/DT);
29    for(unsigned int t = 1; t <= t_max; t++) {
30        Transport::ProgressBar(t, t_max);
31        Transport::CytoStream(membrane, stream, stream_start, stream_ang);
32        Transport::Diffusion(membrane);
33        if(t == FRAP_time/DT) {
34            Transport::Photoswitch(peg_pos[X], peg_pos[Y], bleach_r_px, ↩
                membrane);
35            Transport::Photoswitch(upstream_bleach[X], upstream_bleach[Y], ↩
                bleach_r_px, membrane);
36            Transport::Photoswitch(downstream_bleach[X], downstream_bleach[Y↩
                ], bleach_r_px, membrane);
37            Transport::Photoswitch(peg_pos[X], peg_pos[Y], bleach_r_px, ↩
                stream);
38            Transport::Photoswitch(upstream_bleach[X], upstream_bleach[Y], ↩
                bleach_r_px, stream);
39            Transport::Photoswitch(downstream_bleach[X], downstream_bleach[Y↩
                ], bleach_r_px, stream);
40        }
41        if((t % steps_per_img) == 0) {
42            Radial::getDists(Img::TakeImage(membrane, stream, t/↩
                steps_per_img), (int)(t/steps_per_img));
43        }
44    }
45    return 0;
46 }
```

A.2 *At*IS Classes

A.2.1 Imaging

Img.hpp:

```
1  //
2  // Created by Jordan Hembrow on 2019-04-04.
3  //
4
5  #ifndef ATIMMUNESIMULATION_IMG_HPP
6  #define ATIMMUNESIMULATION_IMG_HPP
7
8  #include <tiffio.hxx>
9  #include <Parameters.hpp>
10 #include <Proteins/Proteins.hpp>
11 #include <Matrix/Mat.hpp>
12 #include <EnumFlags.hpp>
13 #include <vector>
14
15 class Img {
16 private:
17     static TIFF* TIFFOpenSafe(const std::string &filename, const std::string&
           &permissions);
18     static void SaveImage(const std::string &filename, const Mat<uint16> &
           px_data);
19     static std::string GetFilename(int time_step, int fluorescence);
20     static bool inDetectorRange(const std::array<int, N_COORDS> &pos);
21     static void fluorescencePSF(Mat<uint16> &ccd, const std::array<int, 
           N_COORDS> &pos);
22     static void proteinComponent(const std::vector<Proteins> &p, Mat<uint16>&
           &px_grn, Mat<uint16> &px_red);
23     static unsigned int absDistance(const std::array<unsigned int, N_COORDS>&
           &pos, const std::array<unsigned int, N_COORDS> &centre);
24     static void displayPeg(bool peg_displayed, Mat<uint16> &px_grn, Mat<
           uint16> &px_red);
25 public:
26     static Mat<uint16> TakeImage(const std::vector<Proteins> &membrane, 
           const std::vector<Proteins> &stream, int time_step);
27 };
28
29
30 #endif //ATIMMUNESIMULATION_IMG_HPP
```

Img.cpp:

```
//
// Created by Jordan Hembrow on 2019-04-04.
//



#include "Img.hpp"
#include <Matrix/Mat.cpp>
//#include <UnitTest.hpp>

TIFF* Img::TIFFOpenSafe(const std::string &filename, const std::string &permissions) {
    TIFF* tif = TIFFOpen(filename.c_str(), permissions.c_str());
    if(!tif) {
        std::cerr << "File not found!" << std::endl;
        exit(2);
    }
    return tif;
}

void Img::SaveImage(const std::string &filename, const Mat<uint16> &px_data) {
    TIFF* img_out = TIFFOpenSafe(filename, "w");
    TIFFSetField(img_out, TIFFTAG_IMAGEWIDTH, (uint16)px_width);
    TIFFSetField(img_out, TIFFTAG_IMAGELENGTH, (uint16)px_height);
    TIFFSetField(img_out, TIFFTAG_BITSPERSAMPLE, bits_per_sample);
    TIFFSetField(img_out, TIFFTAG_SAMPLESPERPIXEL, samples_per_pixel);
    TIFFSetField(img_out, TIFFTAG_PHOTOMETRIC, photometric);
    auto *buf = (uint16*)_TIFFmalloc(px_width*sizeof(uint16));
    for(uint32 row = 0; row < px_height; row++) {
        for(uint32 col = 0; col < px_width; col++) {
            buf[col] = intensity_gain*px_data[row][col];
        }
        TIFFWriteScanline(img_out, buf, row);
    }
```

```
34
35      _TIFFfree(buf);
36      TIFFClose(img_out);
37  }
38
39  bool Img::inDetectorRange(const std::array<int, N_COORDS> &pos) {
40      if(pos[X] < 0 or pos[X] > px_width) return false;
41      return !(pos[Y] < 0 or pos[Y] > px_height);
42  }
43
44  /*
45   * Takes into account the Point Spread Function of a single fluorescent protein
46   *   The pixels closest to the centre (left, right, up, down) get half the central brightness
47   *   The pixels on the diagonal get a quarter of the central brightness
48   *
49   * The if statements here could be made more efficient but it would look less elegant
50   */
51  void Img::fluorescencePSF(Mat<uint16> &ccd, const std::array<int, N_COORDS> &pos) {
52      for(int i = pos[Y] - 1; i < pos[Y] + 1; i++) {
53          for(int j = pos[X] - 1; j < pos[X] + 1; j++) {
54              if(inDetectorRange({j, i})) {
55                  if(i - pos[Y] == 0 and j - pos[X] == 0)      ccd[i][j] += 4; // Central pixel
56                  else if(i - pos[Y] == 0 or j - pos[X] == 0) ccd[i][j] += 2; // Adjacent
57                  else                                        ccd[i][j] += 1; // Diagonal
58              }
59          }
60      }
61  }
62
63  /*
64   * Determines the pixel data of a single protein collection (i.e. membrane,
```

```
     cytoplasmic stream etc.)
 */
void Img::proteinComponent(const std::vector<Proteins> &p, Mat<uint16> &px_grn, Mat<uint16> &px_red) {
    std::array<double, N_COORDS> curr_pos_microns = {0};
    std::array<int, N_COORDS> curr_pos_px = {0};
    for(const auto &ele : p) {
        curr_pos_microns = ele.GetPos();
        for(int i = 0; i < N_COORDS; i++) {
            curr_pos_px[i] = (int)(curr_pos_microns[i] * micron_to_px[i]);
        }
        switch(ele.GetBleach()) {
            case BLEACHED:  break;
            case RED:       fluorescencePSF(px_red, curr_pos_px); break;
            case GREEN:     fluorescencePSF(px_grn, curr_pos_px); break;
            default:        std::cerr << "Unable to determine state of bleaching" << std::endl; break;
        }
    }
}

/* Cast to long to avoid any issues with unsigned integers and negative numbers */
unsigned int Img::absDistance(const std::array<unsigned int, N_COORDS> &pos, const std::array<unsigned int, N_COORDS> &centre) {
    int diff = 0;
    for(int i = X; i < N_COORDS; i++) {
        diff += (int)std::pow((long)pos[i] - (long)centre[i], 2.0);
    }
    return (unsigned int)std::sqrt(diff);
}

void Img::displayPeg(const bool peg_displayed, Mat<uint16> &px_grn, Mat<uint16> &px_red) {
    if(peg_displayed) {
        for(unsigned int i = peg_pos[Y] - peg_rad_px; i < peg_pos[Y] + peg_rad_px; i++) {
            for(unsigned int j = peg_pos[X] - peg_rad_px; j < peg_pos[X] +
```

```
                peg_rad_px; j++) {
96              if(absDistance({j,i}, peg_pos) < peg_rad_px) {
97                  px_grn[i][j] /= peg_light_attenuation;
98                  px_red[i][j] /= peg_light_attenuation;
99              }
100         }
101     }
102 }
103
104 /*
105  * We only care about the green (main) channel for radial distributions
106  * The red channel is just basic diffusion so is trivial
107  */
108 Mat<uint16> Img::TakeImage(const std::vector<Proteins> &membrane, const std::vector<Proteins> &stream, const int time_step) {
109     Mat<uint16> px_grn(0, px_height, px_width);
110     Mat<uint16> px_red(0, px_height, px_width);
111     proteinComponent(membrane, px_grn, px_red);
112     //proteinComponent(stream, px_grn, px_red);
113
114     /* Peg blocks most light fluorescence from being detected */
115     displayPeg(show_peg, px_grn, px_red);
116
117     SaveImage(GetFilename(time_step, RED), px_red);
118     SaveImage(GetFilename(time_step, GREEN), px_grn);
119     return px_grn;
120 }
121
122 std::string Img::GetFilename(const int time_step, const int fluorescence) {
123     std::string name = "ATIS_Frap_", extension = ".tif";
124     std::string folder, colour, number;
125     switch(fluorescence) {
126         case GREEN: folder = "Output/Green/"; colour = "g_t"; break;
127         case RED:   folder = "Output/Red/"; colour = "r_t"; break;
128         default: std::cerr << "No fluorescence" << std::endl; break;
129     }
130
131
```

```
132     if      (time_step < 10)   number = "000" + std::to_string(time_step);
133     else if(time_step < 100)  number = "00"  + std::to_string(time_step);
134     else if(time_step < 1000) number = "0"   + std::to_string(time_step);
135     else                      number =         std::to_string(time_step);
136 
137     return folder + name + colour + number + extension;
138 }
139 
140 
141 
142 /* === Unit Testing === */
143 /*TEST_F(Img, DetectorRangeCheck) {
144     std::array<double, 2> x_too_high = {img_width + 1, img_height/2};
145     EXPECT_FALSE(Img::inDetectorRange(x_too_high));
146 }*/
```

A.2.2 Matrix

Mat.hpp:

```
1  //
2  // Created by Jordan Hembrow on 2019-03-18.
3  //
4  
5  #ifndef ATIMMUNESIMULATION_MATRIX_H
6  #define ATIMMUNESIMULATION_MATRIX_H
7  
8  template <class T>
9  class Mat {
10 private:
11     unsigned int nn;
12     unsigned int mm;
13     T **data;
14 public:
15     Mat();
16     Mat(unsigned int n, unsigned int m);
17     Mat(const T& val, unsigned int n, unsigned int m);
```

```
18      Mat & operator=(const Mat &rhs);
19      inline T* operator[](unsigned int i);
20      inline const T* operator[](unsigned int i) const;
21      inline unsigned int nrows() const;
22      inline unsigned int ncols() const;
23      ~Mat();
24  };
25
26
27  #endif //ATIMMUNESIMULATION_MATRIX_H
```

Mat.cpp:

```
1   //
2   // Created by Jordan Hembrow on 2019-03-18.
3   //
4
5   #include "Mat.hpp"
6
7   template <class T>
8   Mat<T>::Mat() : nn(0), mm(0), data(0) {}
9
10  template <class T>
11  Mat<T>::Mat(unsigned int n, unsigned int m) : nn(n), mm(m), data(new T*[n]) ↩
        {
12      data[0] = new T[m*n];
13      for(unsigned int i = 1; i < n; i++) {
14          data[i] = data[i-1] + m;
15      }
16  }
17
18  template <class T>
19  Mat<T>::Mat(const T& val, unsigned int n, unsigned int m) : nn(n), mm(m), ↩
        data(new T*[n]){
20      data[0] = new T[m*n];
21      for(unsigned int i = 1; i < n; i++) {
22          data[i] = data[i-1] + m;
```

```
23      }
24      for(unsigned int i = 0; i < n; i++) {
25          for(unsigned int j = 0; j < m; j++) {
26              data[i][j] = val;
27          }
28      }
29  }
30
31  template <class T>
32  Mat<T> & Mat<T>::operator=(const Mat<T> &rhs) {
33      if(this != &rhs) {
34          if(nn != rhs.nn or mm != rhs.mm) {
35              if(data != nullptr) {
36                  delete[] (data[0]);
37                  delete[] (data);
38              }
39              nn = rhs.nn, mm = rhs.mm;
40              data = new T*[nn];
41              data[0] = new T*[nn*mm];
42          }
43          for(unsigned int i = 1; i < nn; i++) {
44              data[i] = data[i-1] + mm;
45          }
46          for(unsigned int i = 0; i < nn; i++) {
47              for(unsigned int j = 0; j < mm; j++) {
48                  data[i][j] = rhs[i][j];
49              }
50          }
51      }
52      return *this;
53  }
54
55
56  template <class T>
57  T* Mat<T>::operator[](const unsigned int i) {
58      return data[i];
59  }
60
```

```
template <class T>
const T* Mat<T>::operator[](const unsigned int i) const {
    return data[i];
}

template <class T>
unsigned int Mat<T>::nrows() const {
    return nn;
}

template <class T>
unsigned int Mat<T>::ncols() const {
    return mm;
}

template <class T>
Mat<T>::~Mat() {
    if(data != nullptr) {
        delete[] (data[0]);
        delete[] (data);
    }
}
```

A.2.3 Proteins

Proteins.hpp:

```
//
// Created by Jordan Hembrow on 2019-03-18.
//

#ifndef ATIMMUNESIMULATION_PROTEINS_H
#define ATIMMUNESIMULATION_PROTEINS_H

#include <array>
#include <EnumFlags.hpp>

```

```
11
12 class Proteins {
13 private:
14     std::array<double, N_COORDS> pos;
15     int fluorescence;
16     int mobility;
17 public:
18     Proteins();
19     Proteins(double x, double y);
20     Proteins(double x, double y, int mob);
21     void SetPos(double x, double y);
22     std::array<double, N_COORDS> GetPos() const;
23     void SetBleach(int bleach_status);
24     void SetMobility(int mob);
25     int GetBleach() const;
26     bool isDiffusable() const;
27     ~Proteins();
28 };
29
30
31 #endif //ATIMMUNESIMULATION_PROTEINS_H
```

Proteins.cpp:

```
1 //
2 // Created by Jordan Hembrow on 2019-03-18.
3 //
4
5 #include "Proteins.hpp"
6 #include <cmath>
7 #include <Parameters.hpp>
8 #include <iostream>
9
10 Proteins::Proteins() : pos{0}, fluorescence(GREEN), mobility(FREE) {}
11
12
13 Proteins::Proteins(const double x, const double y) : pos{x,y}, fluorescence(↩
```

```
    GREEN), mobility(FREE) {}

14
15
16 Proteins::Proteins(const double x, const double y, const int mob) : pos{x,y↩
    }, fluorescence(GREEN), mobility(mob) {}
17
18 void Proteins::SetPos(const double x, const double y) {
19     this->pos[X] = x;
20     this->pos[Y] = y;
21 }
22
23 std::array<double, N_COORDS> Proteins::GetPos() const {
24     return this->pos;
25 }
26
27 void Proteins::SetBleach(const int bleach_status) {
28     if(bleach_status <= GREEN) {
29         this->fluorescence = bleach_status;
30     } else {
31         std::cerr << "Unknown Fluorescence Setting when calling SetBleach()"↩
             << std::endl;
32     }
33 }
34
35 void Proteins::SetMobility(const int mob) {
36     this->mobility = mob;
37 }
38
39 int Proteins::GetBleach() const {
40     return this->fluorescence;
41 }
42
43 bool Proteins::isDiffusable() const{
44     return (this->mobility == FREE);
45 }
46
47
48 Proteins::~Proteins() = default;
```

A.2.4 Radial Distribution

Radial.hpp:

```
1  //
2  // Created by Jordan Hembrow on 2019-03-29.
3  //
4
5  #ifndef ATIMMUNESIMULATION_RADIAL_H
6  #define ATIMMUNESIMULATION_RADIAL_H
7
8  #include <Matrix/Mat.hpp>
9  #include <EnumFlags.hpp>
10 #include <vector>
11 #include <string>
12 #include <tiffio.hxx>
13 #include <array>
14
15
16 typedef struct {
17     unsigned int intensity_sum = 0;
18     unsigned int px_counted = 0;
19 }RadialDist;
20
21 class Radial {
22 private:
23     static unsigned int DistFromCentrePx(const std::array<int, N_COORDS> &↩
        pos, const std::array<unsigned int, N_COORDS> &centre);
24     static const std::string createFilename(const int num, const std::string↩
         &folder);
25     static std::vector<RadialDist> calcDist(const Mat<uint16> &px_intensity,↩
          const std::array<unsigned int, N_COORDS> &pos);
26     static void outputDist(const std::vector<RadialDist> &rd, const int ↩
        current_step, const std::string &folder);
27
28 public:
29     static void getDists(const Mat<uint16> &px_intensity, const int num);
30 };
```

```
31
32
33 #endif //ATIMMUNESIMULATION_RADIAL_H
```

Radial.cpp:

```
1  //
2  // Created by Jordan Hembrow on 2019-03-29.
3  //
4
5  #include <fstream>
6  #include "Radial.hpp"
7  #include "Parameters.hpp"
8  #include "Matrix/Mat.hpp"
9  #include "Matrix/Mat.cpp"
10
11
12 unsigned int Radial::DistFromCentrePx(const std::array<int, N_COORDS> &pos, ↩
       const std::array<unsigned int, N_COORDS> &centre) {
13     double temp_sum = 0;
14     for(int i = 0; i < N_COORDS; i++) {
15         temp_sum += std::pow(pos[i] - centre[i], 2.0);
16     }
17     return (unsigned int)std::round(std::sqrt(temp_sum));
18 }
19
20 std::vector<RadialDist> Radial::calcDist(const Mat<uint16> &px_intensity, ↩
       const std::array<unsigned int, N_COORDS> &centre) {
21     std::vector<RadialDist> rd;
22     rd.resize(radial_dist_size);
23     for(int row = centre[Y] - radial_dist_size; row < centre[Y] + ↩
           radial_dist_size; row++) {
24         for(int col = centre[X] - radial_dist_size; col < centre[X] + ↩
               radial_dist_size; col++) {
25             unsigned int radial_dist = DistFromCentrePx({col, row}, centre);
26             if(radial_dist < radial_dist_size) {
27                 unsigned int arr_idx = radial_dist;
```

```
28                  rd[arr_idx].intensity_sum += px_intensity[row][col];
29                  rd[arr_idx].px_counted++;
30              }
31          }
32      }
33      return rd;
34  }
35
36  /* I might be able to use cases here with things falling through and ↩
        appending an extra zero? */
37  const std::string Radial::createFilename(const int num, const std::string &↩
        folder) {
38      std::string prefix = "Output/Radial/" + folder + "/RadialDistGrn_t";
39      std::string extension = ".csv";
40      std::string number;
41      if(num < 10) {
42          number = "000" + std::to_string(num);
43      }
44      else if(num < 100) {
45          number = "00" + std::to_string(num);
46      }
47      else if(num < 1000) {
48          number = "0" + std::to_string(num);
49      }
50      else {
51          number = std::to_string(num);
52      }
53      return prefix + number + extension;
54  }
55
56  void Radial::outputDist(const std::vector<RadialDist> &rd, const int ↩
        current_step, const std::string &folder) {
57      std::string output_filename = createFilename(current_step, folder);
58      std::ofstream file;
59      file.open(output_filename);
60      file << "r,Intensity" << std::endl;
61      unsigned int mean_intensity;
62      for(int i = 0; i < rd.size(); i++) {
```

```
63          mean_intensity = (unsigned int)std::round((double)rd[i].↩
                intensity_sum/(double)rd[i].px_counted);
64          file << i*px_to_micron << "," << mean_intensity << std::endl;
65      }
66      file.close();
67  }
68
69  void Radial::getDists(const Mat<uint16> &px_intensity, const int num) {
70      std::vector<RadialDist> rd = calcDist(px_intensity, peg_pos);
71      outputDist(rd, num, "Peg");
72
73      rd = calcDist(px_intensity, upstream_bleach);
74      outputDist(rd, num, "Upstream");
75
76      rd = calcDist(px_intensity, downstream_bleach);
77      outputDist(rd, num, "Downstream");
78  }
```

A.2.5 Transport

Transport.hpp:

```
1  //
2  // Created by Jordan Hembrow on 2019-03-29.
3  //
4
5  #ifndef ATIMMUNESIMULATION_TRANSPORT_HPP
6  #define ATIMMUNESIMULATION_TRANSPORT_HPP
7
8  #include <Proteins/Proteins.hpp>
9  #include <Matrix/Mat.hpp>
10 #include <Matrix/Mat.cpp>
11 #include <RadialDistribution/Radial.hpp>
12 #include <Imaging/Img.hpp>
13 #include <array>
14 #include <random>
15 #include <tiffio.hxx>
```

```
16 #include <Parameters.hpp>
17 #include <EnumFlags.hpp>
18
19
20 class Transport {
21 private:
22     static unsigned int proteinsToAdd(double len, double width, double conc)↩
        ;
23     static bool insideBoundaries(const std::array<double, N_COORDS> &pos);
24     static std::array<double, N_COORDS> streamStartPoint(const std::array<↩
        unsigned int, N_COORDS> &start_point, double width_offset);
25     static double SetupStream(std::vector<Proteins> &p, const std::array<↩
        unsigned int, N_COORDS> &start_point);
26     static void BounceOffWalls(std::array<double, N_COORDS> &pos);
27     static double gaussian(const std::array<double, N_COORDS> &pos, const ↩
        std::array<double, N_COORDS> &mean, const std::array<double, N_COORDS↩
        > &stddev);
28     static Mat<uint16> getFrequency(const std::vector<Proteins> &membrane);
29     static const bool streamDelivers(const std::array<double, N_COORDS> &pos↩
        , double rng, const Mat<uint16> &curr_freq);
30     static void streamUpdatePos(std::vector<Proteins> &stream, double theta)↩
        ;
31     static void streamAddNew(std::vector<Proteins> &stream, double theta, ↩
        const std::array<unsigned int, N_COORDS> &start_point);
32     static void streamDepositMembrane(std::vector<Proteins> &membrane, std::↩
        vector<Proteins> &stream);
33 public:
34     static double absDistance(const std::array<double, N_COORDS> &pos, const↩
         std::array<double, N_COORDS> &centre);
35     static void Diffusion(std::vector<Proteins> &p);
36     static void CytoStream(std::vector<Proteins> &membrane, std::vector<↩
        Proteins> &stream, const std::array<unsigned int, N_COORDS> &↩
        start_point, double theta);
37     static void Photoswitch(unsigned int x, unsigned int y, unsigned int r, ↩
        std::vector<Proteins> &p);
38     static void ProgressBar(unsigned int current_step, unsigned int max_step↩
        );
39     static const double setupSystem(std::vector<Proteins> &membrane, std::↩
```

```
        vector<Proteins> &stream);
};


#endif //ATIMMUNESIMULATION_TRANSPORT_H
```

Transport.cpp:

```
//
// Created by Jordan Hembrow on 2019-03-29.
//

#include "Transport.hpp"
#include <algorithm>
#include <Parallel.hpp>
#include <Utility/Util.hpp>
//#include <UnitTest.hpp>

static std::random_device rd;
static std::mt19937 mt(rd());

unsigned int Transport::proteinsToAdd(const double len, const double width, const double conc) {
    return (unsigned int)(conc*len*width);
}

bool Transport::insideBoundaries(const std::array<double, N_COORDS> &pos) {
    if(pos[X] < 0 or pos[X] > img_width) return false;
    return !(pos[Y] < 0 or pos[Y] > img_height);
}

std::array<double, N_COORDS> Transport::streamStartPoint(const std::array<unsigned int, N_COORDS> &start_point, const double width_offset) {
    std::array<double, N_COORDS> pos = {0};
    double shift = (start_point[Y] + global_stream_shift)*px_to_micron + width_offset;

```

```
27      if(start_point[X] == 0) pos[Y] += shift;
28      else                    pos[X] += shift;
29      return pos;
30  }
31
32  /*
33   * We assume that the appressorium is always in the centre
34   * This means the stream always travels all the way from x/y = 0 to x/y = x_max/y_max
35   *
36   * peg_pos and start_point are in px, whereas p.pos is in microns
37   */
38  double Transport::SetupStream(std::vector<Proteins> &p, const std::array<unsigned int, N_COORDS> &start_point) {
39      double theta = std::atan2(peg_pos[Y] - start_point[Y], peg_pos[X] - start_point[X]);
40      double stream_len = 0.0;
41      double dx, dy;
42      if(start_point[X] == 0) {
43          dx = peg_pos[X];
44          dy = std::fabs(peg_pos[Y] - start_point[Y]);
45      } else {
46          dx = std::fabs(peg_pos[X] - start_point[X]);
47          dy = peg_pos[Y];
48      }
49      stream_len = 2*px_to_micron*sqrt(pow(dx,2.0) + pow(dy,2.0));
50      double micron_stream_width = px_to_micron*stream_width;
51      double to_x = cos(theta), to_y = sin(theta);    //cos() and sin() are slow -> precalculate
52
53      std::normal_distribution<> RNG_width{0, micron_stream_width};
54
55      p.resize(proteinsToAdd(stream_len, micron_stream_width, pc_stream));
56      for(auto &ele : p) {
57          ele.SetMobility(FIXED);
58
59          double width_offset = RNG_width(mt);
60          std::array<double, N_COORDS> pos = streamStartPoint(start_point,
```

```
            width_offset);
61
62          double length_offset = Util::rng(0, stream_len);
63          pos[X] += length_offset*to_x, pos[Y] += length_offset*to_y;
64          if(!insideBoundaries(pos)) BounceOffWalls(pos);
65          ele.SetPos(pos[X], pos[Y]);
66      }
67      return theta;
68  }
69
70  /*
71   * Generates the start point (t=0) for the plant cell
72   * Includes setting up the random distribution of diffusive protein and the ↩
        cytoplasmic stream
73   * Returns the angle between the stream and the horizontal axis
74   */
75  const double Transport::setupSystem(std::vector<Proteins> &membrane, std::↩
        vector<Proteins> &stream) {
76
77      /* Pick the largest dimension as the limit for RNG */
78      double rng_max = (img_height > img_width) ? img_height : img_width;
79
80      /* Randomly Distribute PEN3 throughout the cytoplasm/membrane */
81      std::array<double, N_COORDS> test_pos = {0};
82      membrane.resize(proteinsToAdd(img_height, img_width, pc_cytoplasm));
83      for(auto &ele : membrane) {
84          do {
85              test_pos[X] = Util::rng(0, rng_max), test_pos[Y] = Util::rng(0, ↩
                    rng_max);
86          } while(!insideBoundaries(test_pos));
87          ele.SetPos(test_pos[X], test_pos[Y]);
88      }
89
90      return SetupStream(stream, stream_start);
91  }
92
93  /*
94   * Cell wall causes reflection at the upper and lower edges.
```

```
95  * Simulation assumes infinitely long cell length, such that no reflection ↩
        occurs at left or right edge
96  *  -> Requires checking elsewhere for proteins that are outside of the left↩
        or right boundary
97  */
98  void Transport::BounceOffWalls(std::array<double, N_COORDS> &pos) {
99      if(pos[Y] < 0.0) {
100         pos[Y] *= -1;
101     }
102     else if(pos[Y] > img_height) {
103         pos[Y] = (2.0*img_height) - pos[Y];
104     }
105 }
106
107 double Transport::gaussian(const std::array<double, N_COORDS> &pos, const ↩
        std::array<double, N_COORDS> &mean, const std::array<double, N_COORDS> &↩
        stddev) {
108     double normalisation = 1.0/(2.0*M_PI*stddev[X]*stddev[Y]);
109     double x_component = pow(pos[X] - mean[X], 2.0)/(2.0*pow(stddev[X], 2.0)↩
            );
110     double y_component = pow(pos[Y] - mean[Y], 2.0)/(2.0*pow(stddev[Y], 2.0)↩
            );
111     return normalisation * exp(-(x_component + y_component));
112 }
113
114 /*
115  * Determines the number of proteins per pixel
116  * Does not care about bleach status
117  */
118 Mat<uint16> Transport::getFrequency(const std::vector<Proteins> &membrane) {
119     Mat<uint16> membrane_density(0, px_height, px_width);
120     std::array<unsigned int, N_COORDS> px_pos = {0};
121     for(const auto &ele : membrane) {
122         std::array<double, N_COORDS> micron_pos = ele.GetPos();
123         if(insideBoundaries(micron_pos)) {
124             for(unsigned int i = 0; i < N_COORDS; i++) {
125                 px_pos[i] = (unsigned int)(micron_pos[i]*micron_to_px[i]);
126             }
```

```
127             membrane_density[px_pos[Y]][px_pos[X]]++;
128         }
129     }
130     return membrane_density;
131 }
132 /*
133 const bool Transport::streamDelivers(const std::array<double, N_COORDS> &pos↩
    , const double rng, const Mat<uint16> &curr_freq) {
134     std::array<unsigned int, N_COORDS> idx = {(unsigned int)(pos[X]*↩
        micron_to_px[X]), (unsigned int)(pos[Y]*micron_to_px[Y])};
135     int reduction_power = curr_freq[idx[Y]][idx[X]]/reduction_per_proteins;
136     double reduced_chance = std::pow(0.5, reduction_power);
137     //double delivery_prob = gaussian(pos, stream_delivery_centre, ↩
        stream_delivery_stddev);
138     //double delivery_prob = (absDistance(pos, stream_delivery_centre) < ↩
        1.0*peg_rad_px*px_to_micron) ? 1.0 : 0.0;    //I could just use the ↩
        bool and cast to a double on the next line?
139     //return (delivery_prob*reduced_chance > rng);
140     bool delivery_prob = absDistance(pos, stream_delivery_centre) < ↩
        stream_delivery_radius*peg_rad_px*px_to_micron;
141     return ((double)delivery_prob*reduced_chance > rng);
142 }
143 */
144 const bool Transport::streamDelivers(const std::array<double, N_COORDS> &pos↩
    , const double rng, const Mat<uint16> &curr_freq) {
145     std::array<unsigned int, N_COORDS> idx = {(unsigned int)(pos[X]*↩
        micron_to_px[X]), (unsigned int)(pos[Y]*micron_to_px[Y])};
146     double reduction_power = (double)curr_freq[idx[Y]][idx[X]]/↩
        reduction_per_proteins;
147     double reduced_chance = std::exp(-reduction_power);
148     bool delivery_prob = absDistance(pos, stream_delivery_centre) < ↩
        stream_delivery_radius*peg_rad_px*px_to_micron;
149     return ((double)delivery_prob*reduced_chance > rng);
150 }
151 
152 double Transport::absDistance(const std::array<double, N_COORDS> &pos, const↩
     std::array<double, N_COORDS> &centre) {
153     double diff = 0;
```

```
154     for(int i = X; i < N_COORDS; i++) {
155         diff += std::pow(pos[i] - centre[i], 2.0);
156     }
157     return std::sqrt(diff);
158 }
159 
160 /*
161  * Basic diffusion:
162  *      - The distance to move is determined by the relationship from Fick's Law
163  *      - <r^2> = 2Dt for each degree of freedom, thus: dr = sqrt(4D*dt)
164  *      - A random angle is generated in the range [0, 2pi) to make the movement random.
165  */
166 void Transport::Diffusion(std::vector<Proteins> &p) {
167     std::uniform_real_distribution<> RNG(0, 2*M_PI);
168     std::array<double, N_COORDS> pos = {0};
169     double theta;
170     for(auto &ele : p) {
171         if(ele.isDiffusable()) {
172             theta = Util::rng(0.0, 2.0*M_PI);
173             pos = ele.GetPos();
174             pos[X] += movement_per_step*cos(theta), pos[Y] += movement_per_step*sin(theta);
175             BounceOffWalls(pos);
176             ele.SetPos(pos[X], pos[Y]);
177         }
178     }
179 /*
180     parallel_for(p.size(), [&](int start, int end) {
181        for(int i = start; i < end; i++) {
182            auto &ele = p[i];
183            if(ele.isDiffusable()) {
184                //theta = RNG(mt);
185                theta = Util::rng(0, 2*M_PI);
186                pos = ele.GetPos();
187                pos[X] += movement_per_step*cos(theta), pos[Y] += movement_per_step*sin(theta);
```

```
188                 BounceOffWalls(pos);
189                 ele.SetPos(pos[X], pos[Y]);
190             }
191         }
192     });*/
193 }
194
195 /* Delete those proteins that go outside of the simulation boundary */
196 /* Loop backwards to avoid going off the end of the array after deletion */
197 void Transport::streamUpdatePos(std::vector<Proteins> &stream, double theta)↩
     {
198     double to_x = cos(theta), to_y = sin(theta);    //cos() and sin() are ↩
        slow -> precalculate
199     const double dist_to_move = stream_vel * DT;
200
201     auto ele = stream.begin();
202     while(ele != stream.end()) {
203         if(!ele->isDiffusable()) {
204             std::array<double, N_COORDS> pos = ele->GetPos();
205             pos[X] += dist_to_move*to_x, pos[Y] += dist_to_move*to_y;
206             if(!insideBoundaries(pos)) {
207                 ele = stream.erase(ele);
208             } else {
209                 ele->SetPos(pos[X], pos[Y]);
210                 ele++;
211             }
212         }
213     }
214 }
215
216 /* Add new proteins to the start of the stream */
217 void Transport::streamAddNew(std::vector<Proteins> &stream, const double ↩
    theta, const std::array<unsigned int, N_COORDS> &start_point) {
218     const double micron_stream_width = px_to_micron*stream_width;
219     const double dist_to_move = stream_vel * DT;
220     double to_x = cos(theta), to_y = sin(theta);    //cos() and sin() are ↩
        slow -> precalculate
221     std::normal_distribution<> RNG_width{0, micron_stream_width};
```

```
222
223     /* calculation of how many to add based on vol of stream moved (width*↩
            dist_to_move) and conc of stream */
224     unsigned int number_added = proteinsToAdd(dist_to_move, ↩
            micron_stream_width, pc_stream);
225     for(unsigned int i = 0; i < number_added; i++) {
226         double width_offset = RNG_width(mt);
227         std::array<double, N_COORDS> pos = streamStartPoint(start_point, ↩
                width_offset);
228         double len_shift = Util::rng(0, dist_to_move);
229         pos[X] += len_shift*to_x, pos[Y] += len_shift*to_y;
230         BounceOffWalls(pos);
231         Proteins new_p(pos[X], pos[Y], FIXED);
232         stream.push_back(new_p);
233     }
234 }
235
236 /* Delivery from the stream to the infection site -> stream protein now in ↩
    membrane */
237 void Transport::streamDepositMembrane(std::vector<Proteins> &membrane, std::↩
    vector<Proteins> &stream) {
238     const double gaussian_amp = 1.0/(2.0*M_PI*stream_delivery_stddev[X]*↩
            stream_delivery_stddev[Y]);
239     Mat<uint16> protein_freq = getFrequency(membrane);
240     unsigned int delivery_counter = 0;
241
242     auto ele = stream.begin();
243     while(ele != stream.end()) {
244         if(streamDelivers(ele->GetPos(), Util::rng(0, gaussian_amp), ↩
                protein_freq)) {
245             ele->SetMobility(FREE);
246             membrane.push_back(*ele);
247             ele = stream.erase(ele);
248             delivery_counter++;
249             if(delivery_counter >= stream_delivery_rate*DT) return;
250         } else { ele++; }
251     }
252 }
```

```
253
254 void Transport::CytoStream(std::vector<Proteins> &membrane, std::vector<↩
    Proteins> &stream, const std::array<unsigned int, N_COORDS> &start_point,↩
     double theta) {
255     /* 1. Move stream along and delete proteins that go outside of the ↩
        simulation boundary */
256     streamUpdatePos(stream, theta);
257
258     /* 2. Add new proteins to the start of the stream */
259     streamAddNew(stream, theta, start_point);
260
261     /* 3. Delivery from the stream to the infection site -> stream protein ↩
        now in membrane */
262     streamDepositMembrane(membrane, stream);
263
264 }
265
266 /* Note that the area is square, so a block of (x-r)->(x+r) and (y-r)->(y+r)↩
     */
267 void Transport::Photoswitch(const unsigned int x, const unsigned int y, ↩
    const unsigned int r, std::vector<Proteins> &p) {
268     std::array<double, N_COORDS> centre = {x/micron_to_px[X], y/micron_to_px↩
        [Y]};
269     const double bleach_range = (2.0*r)/(micron_to_px[X] + micron_to_px[Y]);
270     for(auto &ele : p) {
271         std::array<double, N_COORDS> pos = ele.GetPos();
272         if(fabs(centre[X] - pos[X]) < bleach_range and fabs(centre[Y] - pos[↩
            Y]) < bleach_range) {
273             ele.SetBleach(RED);
274         }
275     }
276 }
277
278 void Transport::ProgressBar(const unsigned int current_step, const unsigned ↩
    int max_step) {
279     int bar_width = 70;
280     double progress = (double)current_step/(double)max_step;
281
```

```
282     std::cout << "[";
283     int pos = (int)(bar_width * progress);
284     for (int i = 0; i < bar_width; ++i) {
285         if (i < pos) std::cout << "=";
286         else if (i == pos) std::cout << ">";
287         else std::cout << " ";
288     }
289     std::cout << "] " << int(progress * 100.0) << " %\r";
290     std::cout.flush();
291 }
292
293
294
295 /*  === Unit Testing === */
296 /*
297 TEST(testTransport, absDistTest) {
298 std::array<double, N_COORDS> pos1 = {0.0, 0.0};
299 std::array<double, N_COORDS> pos2 = {3.0, 4.0};
300 EXPECT_DOUBLE_EQ(Transport::absDistance(pos1, pos2), 5.0);
301 } */
```

A.2.6 Utility

Util.hpp:

```
1  //
2  // Created by Jordan Hembrow on 2019-05-09.
3  //
4
5  #ifndef ATIMMUNESIMULATION_UTIL_HPP
6  #define ATIMMUNESIMULATION_UTIL_HPP
7
8  #include <array>
9
10 class Util {
11 private:
12     static double randGen(int &idum);
```

```
13 public:
14     static double rng(double min, double max);
15     static double rngMT(double min, double max);
16 };
17 
18 
19 #endif //ATIMMUNESIMULATION_UTIL_HPP
```

Util.cpp:

```
1  //
2  // Created by Jordan Hembrow on 2019-05-09.
3  //
4  
5  #include "Util.hpp"
6  //#include <UnitTest.hpp>
7  #include <random>
8  
9  static int rand_gen_seed = -1;  // Don't change this! Ensures seed is ↩
       correctly picked.
10 
11 /*
12  * This should be called with seed < 0 to initialise the seed and shuffle ↩
        table
13  * After that, make no further changes to the seed
14  * Modified from 'Numerical Recipes in C++ - Second Edition'
15  * This is a combination of two generators and a shuffle to ensure ↩
        negligible linear correlations
16  * Gives output in the range [0.0,1.0)
17  */
18 double Util::randGen(int &idum) {
19     const int IM1 = 2147483563, IM2 = 2147483399;
20     const int IA1 = 40014, IA2 = 40692, IQ1 = 53688, IQ2 = 52774;
21     const int IR1 = 12211, IR2 = 3791, NTAB=32, IMM1 = IM1 - 1;
22     const int NDIV = 1 + (IMM1/NTAB);
23     const double EPS = 3.0e-16, RNMX = 1.0 - EPS, AM = 1.0/(double)IM1;
24     static int idum2 = 123456789, iy = 0;
```

```
25      static std::array<int, NTAB> iv;
26      int j,k;
27      double temp;
28
29      if(idum <= 0) {
30          idum = (idum == 0) ? 1 : -idum;      // Ensure positive idum
31          idum2 = idum;
32          for(j = NTAB + 7; j >= 0; j--) {     // Load shuffle table (after 8 warmups)
33              k = idum/IQ1;
34              idum = IA1 * (idum - k*IQ1) - k*IR1;
35              if(idum < 0) idum += IM1;
36              if(j < NTAB) iv[j] = idum;
37          }
38          iy = iv[0];
39      }
40
41      k = idum/IQ1;                            // Start here if not initialising
42      idum = IA1 * (idum - k*IQ1) - k*IR1;     // Compute idum = (IA1*idum) % IM1 without overflows using Schrage's method
43      if(idum < 0) idum += IM1;
44      k = idum2/IQ2;
45      idum2 = IA2 * (idum2 - k*IQ1) - k*IR2;   // Compute idum2 = (IA2*idum2) % IM2 likewise
46      if(idum2 < 0) idum2 += IM2;
47      j = iy/NDIV;                             // Will be in range 0 . . NTAB - 1
48      iy = iv[j] - idum2;                      // Here idum is shuffled; idum and idum2 are combined
49      iv[j] = idum;
50      if(iy < 1) iy += IMM1;
51      if((temp = AM*iy) > RNMX) return RNMX;   // Don't expect endpoint values
52      return temp;
53  }
54
55  /*
56   * Using randGen() gives a repeat length of >2x10^18 - perfect for monte
```

```
    carlo
 */
double Util::rng(const double min, const double max) {
    double range = max - min;
    double ret_val = (randGen(rand_gen_seed) * range) + min;
    return ret_val;
}

double Util::rngMT(const double min, const double max) {
    static std::mt19937_64 gen(std::random_device{}());
    std::uniform_real_distribution<> dis(min, max);
    return dis(gen);
}
/*
TEST(TestUtil, rngSeeding) {
    rand_gen_seed = -1;
    Util::rng(0.0, 1.0);
    EXPECT_GT(rand_gen_seed, 0);            // seed should be initialised to a positive (non-zero) value
}

TEST(TestUtil, rngRange) {
    const double min = -0.5;
    const double max = 0.5;
    for(int i = 0; i < 3; i++) {
        double random_no = Util::rng(min, max);
        EXPECT_GE(random_no, min);          // Note: range is always [min, max)
        EXPECT_LT(random_no, max);
    }
}
 */
```

Bibliography

Acevedo-Garcia, Johanna, Stefan Kusch, and Ralph Panstruga. 2014. 'Magical mystery tour : MLO proteins in plant immunity and beyond.' *New Phytologist* 204, no. 2 (October): 273–281.

Aggarwal, Neeraj K., Naveen Kumar, and Mahak Mittal. 2022. 'Opportunities and Challenges for Use of Bioethanol as Transport Fuel: A Global Perspective.' Chap. 15 in *Bioethanol Production*, 191–199.

Alcamo, J. 1994. *IMAGE 2.0: Integrated Modeling of Global Climate Change.*

Alcor, Damien, Géraldine Gouzer, and Antoine Triller. 2009. 'Single-particle tracking methods for the study of membrane receptors dynamics.' *European Journal of Neuroscience* 30, no. 6 (September): 987–997.

Alcott, Lewis J., Benjamin J. W. Mills, and Simon W. Poulton. 2019. 'Stepwise Earth oxygenation is an inherent property of global biogeochemical cycling.' *Science* 366, no. 6471 (December): 1333–1337.

Allan, Claudia, Richard J Morris, and Claudia-Nicole Meisrimler. 2022. 'Encoding, transmission, decoding, and specificity of calcium signals in plants.' Edited by Karl-Josef Dietz. *Journal of Experimental Botany* 73, no. 11 (June): 3372–3385.

Anderson, Robyn, Philipp E. Bayer, and David Edwards. 2020. 'Climate change and the need for agricultural adaptation.' *Current Opinion in Plant Biology* 56:197–202.

Andrews, Nicholas L., Keith A. Lidke, Janet R. Pfeiffer, et al. 2008. 'Actin restricts FcRI diffusion and facilitates antigen-induced receptor immobilization.' *Nature Cell Biology* 10, no. 8 (August): 955–963.

Asai, Shuta, and Ken Shirasu. 2015. 'Plant cells under siege: plant immune system versus pathogen effectors.' *Current Opinion in Plant Biology* 28 (December): 1–8.

Ashofteh, Parisa-Sadat, Omid Bozorg Haddad, and Miguel A. Mariño. 2015. 'Risk Analysis of Water Demand for Agricultural Crops under Climate Change.' *Journal of Hydrologic Engineering* 20 (4).

Asseng, S., F. Ewert, P. Martre, et al. 2015. 'Rising temperatures reduce global wheat production.' *Nature Climate Change* 5 (2): 143–147.

Autran, Daphné, George W. Bassel, Eunyoung Chae, et al. 2021. 'What is quantitative plant biology?' *Quantitative Plant Biology* 2 (May): e10.

Bebber, Daniel P., and Sarah J. Gurr. 2015. 'Crop-destroying fungal and oomycete pathogens challenge food security.' *Fungal Genetics and Biology* 74:62–64.

Bebber, Daniel P., Mark A.T. Ramotowski, and Sarah J. Gurr. 2013. 'Crop pests and pathogens move polewards in a warming world.' *Nature Climate Change.*

Bellandi, Annalisa, Diana Papp, Andrew Breakspear, et al. 2022. 'Diffusion and bulk flow of amino acids mediate calcium waves in plants.' *Science Advances* 8, no. 42 (October).

Bellincampi, Daniela, Felice Cervone, and Vincenzo Lionetti. 2014. 'Plant cell wall dynamics and wall-related susceptibility in plant-pathogen interactions.' *Frontiers in Plant Science* 5 (May).

Benfey, Philip N, and Thomas Mitchell-Olds. 2008. 'From genotype to phenotype: systems biology meets natural variation.' *Science (New York, N.Y.)* 320, no. 5875 (April): 495–7.

Benikhlef, Lehcen, Floriane L'Haridon, Eliane Abou-Mansour, et al. 2013. 'Perception of soft mechanical stress in Arabidopsis leaves activates disease resistance.' *BMC Plant Biology* 13 (1).

Bent, Andrew F., and David Mackey. 2007. 'Elicitors, Effectors, and R Genes: The New Paradigm and a Lifetime Supply of Questions.' *Annual Review of Phytopathology* 45, no. 1 (September): 399–436.

Bernardes, Mariana Furio Franco, Murilo Pazin, Lilian Cristina Pereira, and Daniel Junqueira Dorta. 2015. 'Impact of Pesticides on Environmental and Human Health.' In *Toxicology Studies - Cells, Drugs and Environment*. InTech, July.

Beulke, Sabine, and Colin Brown. 2001. 'Evaluation of methods to derive pesticide degradation parameters for regulatory modelling.' *Biology and Fertility of Soils* 33, no. 6 (June): 558–564.

Bhola, V., F. Swalaha, R. Ranjith Kumar, M. Singh, and F. Bux. 2014. 'Overview of the potential of microalgae for CO2 sequestration.' *International Journal of Environmental Science and Technology* 11 (7): 2103–2118.

Bläßle, Alexander, Gary Soh, Theresa Braun, et al. 2018. 'Quantitative diffusion measurements using the open-source software PyFRAP.' *Nature Communications* 9, no. 1 (April): 1582.

Blumenthal, Daniel, Leo Goldstien, Michael Edidin, and Levi A. Gheber. 2015. 'Universal Approach to FRAP Analysis of Arbitrary Bleaching Patterns.' *Scientific Reports* 5, no. 1 (June): 11655.

Boddiger, David. 2007. 'Boosting biofuel crops could threaten food security.' *The Lancet* 370:923–924.

Boote, Kenneth J., Leon H. ALLEN, Pagadala V. V. PRASAD, et al. 2005. 'Elevated Temperature and CO2 Impacts on Pollination, Reproductive Growth, and Yield of Several Globally Important Crops.' *Journal of Agricultural Meteorology* 60 (5): 469–474.

Borji, Ali. 2022. 'Generated Faces in the Wild: Quantitative Comparison of Stable Diffusion, Midjourney and DALL-E 2' (October).

Boudsocq, Marie, Matthew R. Willmann, Matthew McCormack, et al. 2010. 'Differential innate immune signalling via Ca2+ sensor protein kinases.' *Nature* 464, no. 7287 (March): 418–422.

Bourdais, Gildas, Deirdre H. McLachlan, Lydia M. Rickett, et al. 2019. 'The use of quantitative imaging to investigate regulators of membrane trafficking in Arabidopsis stomatal closure.' *Traffic* 20, no. 2 (February): 168–180.

Branco, Rémi, Eliza Jane Pearsall, Chelsea A. Rundle, et al. 2017. 'Quantifying the plant actin cytoskeleton response to applied pressure using nanoindentation.' *Protoplasma* 254, no. 2 (March): 1127–1137.

Brawley, Crista M., and Ronald S. Rock. 2009. 'Unconventional myosin traffic in cells reveals a selective actin cytoskeleton.' *Proceedings of the National Academy of Sciences of the United States of America* 106 (24): 9685–9690.

Bressloff, Paul C., and Jay M. Newby. 2013. 'Stochastic models of intracellular transport.' *Reviews of Modern Physics* 85, no. 1 (January): 135–196.

Breuer, David, and Zoran Nikoloski. 2015. 'DeFiNe: An optimisation-based method for robust disentangling of filamentous networks.' *Scientific Reports* 5 (October): 1–14.

Breuer, David, Jacqueline Nowak, Alexander Ivakov, et al. 2017. 'System-wide organization of actin cytoskeleton determines organelle transport in hypocotyl plant cells.' *Proceedings of the National Academy of Sciences* 114, no. 28 (June): E5741–E5749.

Bryers, James D., and F. Drummond. 1998. 'Local macromolecule diffusion coefficients in structurally non-uniform bacterial biofilms using fluorescence recovery after photobleaching (FRAP).' *Biotechnology and Bioengineering* 60 (4): 462–473.

Burnett, Mark M., and Anders E. Carlsson. 2012. 'Quantitative analysis of approaches to measure cooperative phosphate release in polymerized actin.' *Biophysical Journal* 103 (11): 2369–2378.

Burrows, Michael T., David S. Schoeman, Lauren B. Buckley, et al. 2011. 'The Pace of Shifting Climate in Marine and Terrestrial Ecosystems.' *Science* 334, no. 6056 (November): 652–655.

Cannistraci, Carlo Vittorio, and Massimo Alessio. 2016. 'Image Pretreatment Tools I: Algorithms for Map Denoising and Background Subtraction Methods.' In *Methods in Molecular Biology*, 79–89.

Cao, Lingyan, Wenyi Wang, Weiwei Zhang, and Christopher J. Staiger. 2022. 'Lipid Signaling Requires ROS Production to Elicit Actin Cytoskeleton Remodeling during Plant Innate Immunity.' *International Journal of Molecular Sciences* 23, no. 5 (February): 2447.

Chechkin, Aleksei V., Flavio Seno, Ralf Metzler, and Igor M. Sokolov. 2017. 'Brownian yet Non-Gaussian Diffusion: From Superstatistics to Subordination of Diffusing Diffusivities.' *Physical Review X* 7, no. 2 (April): 021002.

Chen, Hao, and Yongjun Lin. 2013. 'Promise and issues of genetically modified crops.' *Current Opinion in Plant Biology* 16 (2): 255–260.

Chen, I. Ching, Jane K. Hill, Ralf Ohlemüller, David B. Roy, and Chris D. Thomas. 2011. 'Rapid range shifts of species associated with high levels of climate warming.' *Science* 333 (6045): 1024–1026.

Cheng, Chia-Yi, Vivek Krishnakumar, Agnes P. Chan, et al. 2017. 'Araport11: a complete reannotation of the Arabidopsis thaliana reference genome.' *The Plant Journal* 89, no. 4 (February): 789–804.

Chia, Shaphan Y., Chrysantus M. Tanga, Joop JA van Loon, and Marcel Dicke. 2019. 'Insects for sustainable animal feed: inclusive business models involving smallholder farmers.' *Current Opinion in Environmental Sustainability* 41:23–30.

Cochran, William G. 1954. 'Some Methods for Strengthening the Common χ 2 Tests.' *Biometrics* 10, no. 4 (December): 417.

Collinge, David B. 2009. *Cell wall appositions: The first line of defence.*

Collins, Nicholas C., Hans Thordal-Christensen, Volker Lipka, et al. 2003. 'SNARE-protein-mediated disease resistance at the plant cell wall.' *Nature* 425, no. 6961 (October): 973–977.

Conway, Gordon. 2012. *One Billion Hungry: Can We Feed The World?* Cornell University Press.

Cvrčková, Fatima. 2013. 'Formins and membranes: anchoring cortical actin to the cell wall and beyond.' *Frontiers in Plant Science* 4.

Dangl, Jeffery L., and Jonathan D G. Jones. 2001. 'Plant Pathogens and Integrated Defence Responses To Infection.' *Nature* 411 (June).

Daudi, Arsalan, Zhenyu Cheng, Jose A. O'Brien, et al. 2012. 'The Apoplastic Oxidative Burst Peroxidase in Arabidopsis Is a Major Component of Pattern-Triggered Immunity.' *The Plant Cell* 24, no. 1 (February): 275–287.

Day, Brad, Jessica L. Henty, Katie J. Porter, and Christopher J. Staiger. 2011. 'The pathogen-actin connection: A platform for defense signaling in plants.' *Annual Review of Phytopathology* 49:483–506.

Dean, Ralph, JAN A. L. VAN KAN, ZACHARIAS A. PRETORIUS, et al. 2012. 'The Top 10 fungal pathogens in molecular plant pathology.' *Molecular Plant Pathology* 13, no. 4 (May): 414–430.

Deeks, Michael J., Matyáš Fendrych, Andrei Smertenko, et al. 2010. 'The plant formin AtFH4 interacts with both actin and microtubules, and contains a newly identified microtubule-binding domain.' *Journal of Cell Science* 123 (8): 1209–1215.

Deeks, Michael J., and Patrick J. Hussey. 2005. 'Arp2/3 and SCAR: Plants move to the fore.' *Nature Reviews Molecular Cell Biology* 6 (12): 954–964.

Deeks, Michael J., Patrick J. Hussey, and Brendan Davies. 2002. 'Formins: Intermediates in signal-transduction cascades that affect cytoskeletal reorganization.' *Trends in Plant Science* 7 (11): 492–498.

Dethier, Jean-Jacques, and Alexandra Effenberger. 2012. 'Agriculture and development: A brief review of the literature.' *Economic Systems* 36, no. 2 (June): 175–205.

Dhankher, Om Parkash, and Christine H. Foyer. 2018. 'Climate resilient crops for improving global food security and safety.' *Plant Cell and Environment* 41 (5): 877–884.

Al-Diri, Bashir, Andrew Hunter, David Steel, and Maged Habib. 2010. 'Automated analysis of retinal vascular network connectivity.' *Computerized Medical Imaging and Graphics* 34, no. 6 (September): 462–470.

Dodds, Peter N., and John P. Rathjen. 2010. *Plant immunity: Towards an integrated view of plant-pathogen interactions.*

Ekebjærg, Lars, and Peter Justesenu. 1991. 'An explicit scheme for advection-diffusion modelling in two dimensions.' *Computer Methods in Applied Mechanics and Engineering* 88, no. 3 (July): 287–297.

Evangelista, Paul, Nicholas Young, and Jonathan Burnett. 2013. 'How will climate change spatially affect agriculture production in Ethiopia? Case studies of important cereal crops.' *Climatic Change* 119 (3-4): 855–873.

Fan, Jun, and Peter Doerner. 2012. 'Genetic and molecular basis of nonhost disease resistance: complex, yes; silver bullet, no.' *Current Opinion in Plant Biology* 15, no. 4 (August): 400–406.

FAO. 2004. *The State of Food and Agriculture: Meeting the needs of the poor?* 58–76.

Faulkner, Christine, Ji Zhou, Alexandre Evrard, et al. 2017. 'An automated quantitative image analysis tool for the identification of microtubule patterns in plants.' *Traffic* 18 (10): 683–693.

Fenik, Jolanta, Maciej Tankiewicz, and Marek Biziuk. 2011. 'Properties and determination of pesticides in fruits and vegetables.' *TrAC Trends in Analytical Chemistry* 30, no. 6 (June): 814–826.

Fick, Adolph. 1855. ' V. On liquid diffusion.' *The London, Edinburgh, and Dublin Philosophical Magazine and Journal of Science.*

Fisher, Matthew C., Daniel A. Henk, Cheryl J. Briggs, et al. 2012. *Emerging fungal threats to animal, plant and ecosystem health.*

Fletcher, Daniel A., and R. Dyche Mullins. 2010. 'Cell mechanics and the cytoskeleton.' *Nature* 463 (7280): 485–492.

Frangi, Alejandro F, Wiro J Niessen, Koen L Vincken, and Max A Viergever. 1998. 'Multiscale vessel enhancement filtering.' *Medical Image Computing and Computer-Assisted Intervention — MICCAI'98. MICCAI 1998. Lecture Notes in Computer Science* 1496:130–137.

Fuchs, Elaine, and Klaus Weber. 1994. 'INTERMEDIATE FILAMENTS: Structure, Dynamics, Function, and Disease.' *Annual Reviews Biochemistry* 63:345–82.

Fuchs, Rene, Michaela Kopischke, Christine Klapprodt, et al. 2016. 'Immobilized Subpopulations of Leaf Epidermal Mitochondria Mediate PENETRATION2-Dependent Pathogen Entry Control in Arabidopsis.' *The Plant Cell* 28, no. 1 (January): 130–145.

Geiger, Andreas C., Casey J. Smith, Nita Takanti, et al. 2020. 'Anomalous Diffusion Characterization by Fourier Transform-FRAP with Patterned Illumination.' *Biophysical Journal* 119, no. 4 (August): 737–748.

Geitmann, Anja, and A. M.C. Emons. 2000. 'The cytoskeleton in plant and fungal cell tip growth.' *Journal of Microscopy* 198 (3): 218–245.

Geitmann, Anja, and Andreas Nebenfãhr. 2015. 'Navigating the plant cell: Intracellular transport logistics in the green kingdom.' *Molecular Biology of the Cell* 26 (19): 3373–3378.

Gillespie, Stuart, and Mara van den Bold. 2017. 'Agriculture, Food Systems, and Nutrition: Meeting the Challenge.' *Global Challenges* 1 (3): 1600002.

Glazebrook, Jane. 2005. 'Contrasting Mechanisms of Defense Against Biotrophic and Necrotrophic Pathogens.' *Annual Review of Phytopathology* 43, no. 1 (September): 205–227.

Goldstein, Raymond E., and Jan Willem van de Meent. 2015. 'A physical perspective on cytoplasmic streaming.' *Interface Focus* 5, no. 4 (May).

Hadjidemetriou, Stathis, Derek Toomre, and James Duncan. 2008. 'Motion tracking of the outer tips of microtubules.' *Medical Image Analysis* 12, no. 6 (December): 689–702.

Hardham, Adrienne R., Daigo Takemoto, and Rosemary G. White. 2008. 'Rapid and dynamic subcellular reorganization following mechanical stimulation of Arabidopsis epidermal cells mimics responses to fungal and oomycete attack.' *BMC Plant Biology.*

Hay, F. R., and R. J. Probert. 2013. 'Advances in seed conservation of wild plant species: a review of recent research.' *Conservation Physiology* 1, no. 1 (November): cot030–cot030.

He, Yunxia, Juan Xu, Xiaoyang Wang, et al. 2019. 'The arabidopsis pleiotropic drug resistance transporters PEN3 and PDR12 mediate camalexin secretion for resistance to botrytis cinerea.' *Plant Cell* 31 (9): 2206–2222.

He, Zhouqing, Tingting Huang, Kevin Ao, Xiaofang Yan, and Yan Huang. 2017. 'Sumoylation, Phosphorylation, and Acetylation Fine-Tune the Turnover of Plant Immunity Components Mediated by Ubiquitination.' *Frontiers in Plant Science* 8 (October).

Hématy, Kian, Melisa Lim, Candice Cherk, et al. 2020. 'Moonlighting Function of Phytochelatin Synthase1 in Extracellular Defense against Fungal Pathogens.' *Plant Physiology* 182, no. 4 (April): 1920–1932.

Henchion, Maeve, Mary McCarthy, Virginia C. Resconi, and Declan Troy. 2014. 'Meat consumption: Trends and quality matters.' *Meat Science* 98, no. 3 (November): 561–568.

Henty-Ridilla, Jessica L., Jiejie Li, Brad Day, and Christopher J. Staiger. 2014. ' ACTIN DEPOLYMERIZING FACTOR4 Regulates Actin Dynamics during Innate Immune Signaling in Arabidopsis.' *The Plant Cell* 26, no. 1 (January): 340–352.

Henty-Ridilla, Jessica L., Masaki Shimono, Jiejie Li, et al. 2013. 'The Plant Actin Cytoskeleton Responds to Signals from Microbe-Associated Molecular Patterns.' *PLoS Pathogens* 9 (4).

Howard, R. J., M. A. Ferrari, D. H. Roach, and N. P. Money. 1991. 'Penetration of hard substrates by a fungus employing enormous turgor pressures.' *Proceedings of the National Academy of Sciences of the United States of America* 88 (24): 11281–11284.

Huang, Bo. 2010. 'Super-resolution optical microscopy: multiple choices.' *Current Opinion in Chemical Biology* 14, no. 1 (February): 10–14.

Hückelhoven, Ralph. 2014. 'The effective papilla hypothesis.' *New Phytologist* 204 (3): 438–440.

Hughes, Aoife, Christine Faulkner, Richard J. Morris, and Melissa Tomkins. 2021. 'Intercellular Communication as a Series of Narrow Escape Problems.' *IEEE Transactions on Molecular, Biological and Multi-Scale Communications* 7, no. 2 (June): 89–93.

Huisken, Jan, and Didier Y. R. Stainier. 2007. 'Even fluorescence excitation by multidirectional selective plane illumination microscopy (mSPIM).' *Optics Letters* 32, no. 17 (September): 2608.

Humphry, Matt, Chiara Consonni, and Ralph Panstruga. 2006. 'mlo-based powdery mildew immunity: silver bullet or simply non-host resistance?' *Molecular Plant Pathology* 7, no. 6 (November): 605–610.

Hussey, Patrick J., Tijs Ketelaar, and Michael J. Deeks. 2006. 'Control of the actin cytoskeleton in plant cell growth.' *Annual Review of Plant Biology* 57:109–125.

Iglina, Tatyana, Pavel Iglin, and Dmitry Pashchenko. 2022. 'Industrial CO2 Capture by Algae: A Review and Recent Advances.' *Sustainability (Switzerland)* 14 (7).

Jelenska, Joanna, Sandra M. Davern, Robert F. Standaert, Saed Mirzadeh, and Jean T. Greenberg. 2017. 'Flagellin peptide flg22 gains access to long-distance trafficking in Arabidopsis via its receptor, FLS2.' *Journal of Experimental Botany* 68, no. 7 (March): 1769–1783.

Johansson, Oskar N., Elena Fantozzi, Per Fahlberg, et al. 2014. 'Role of the penetration-resistance genes PEN1, PEN2 and PEN3 in the hypersensitive response and race-specific resistance in Arabidopsis thaliana.' *Plant Journal.*

Jones, Jonathan D G., and Jeffery L. Dangl. 2006. *The plant immune system.*

Jülicher, F., K. Kruse, J. Prost, and J. F. Joanny. 2007. 'Active behavior of the Cytoskeleton.' *Physics Reports* 449 (1-3): 3–28.

Kachroo, Pradeep, Tessa M. Burch-Smith, and Murray Grant. 2021. 'An Emerging Role for Chloroplasts in Disease and Defense.' *Annual Review of Phytopathology* 59, no. 1 (August): 423–445.

Kadota, Yasuhiro, Ken Shirasu, and Cyril Zipfel. 2015. 'Regulation of the NADPH Oxidase RBOHD During Plant Immunity.' *Plant and Cell Physiology* 56, no. 8 (August): 1472–1480.

Kaksonen, Marko, and Aurélien Roux. 2018. 'Mechanisms of clathrin-mediated endocytosis.' *Nature Reviews Molecular Cell Biology* 19, no. 5 (May): 313–326.

Kalachova, Tetiana, Martin Janda, Vladimír Šašek, et al. 2020. 'Identification of salicylic acid-independent responses in an Arabidopsis phosphatidylinositol 4-kinase beta double mutant.' *Annals of Botany* 125, no. 5 (April): 775–784.

Kang, Minchul. 2022. 'Regression Analysis of Confocal FRAP and its Application to Diffusion in Membranes.' *Journal of Fluorescence* 32, no. 3 (May): 1031–1038.

Kang, Minchul, Charles A. Day, Anne K. Kenworthy, and Emmanuele DiBenedetto. 2012. 'Simplified equation to extract diffusion coefficients from confocal FRAP data.' *Traffic* 13, no. 12 (December): 1589–1600.

Kang, Yongsung, Joanna Jelenska, Nicolas M. Cecchini, et al. 2014. 'HopW1 from Pseudomonas syringae Disrupts the Actin Cytoskeleton to Promote Virulence in Arabidopsis.' Edited by Shengyang He. *PLoS Pathogens* 10, no. 6 (June): e1004232.

Kapoor, Varun, William G. Hirst, Christoph Hentschel, Stephan Preibisch, and Simone Reber. 2019. 'MTrack: Automated Detection, Tracking, and Analysis of Dynamic Microtubules.' *Scientific Reports* 9 (1): 1–12.

Kim, Tae Kyun. 2017. 'Understanding one-way ANOVA using conceptual figures.' *Korean Journal of Anesthesiology* 70 (1): 22.

Kobayashi, Yuhko, Issei Kobayashi, Yasuro Funaki, et al. 1997. 'Dynamic reorganization of microfilaments and microtubules is necessary for the expression of non-host resistance in barley coleoptile cells.' *The Plant Journal* 11, no. 3 (March): 525–537.

Koçar, Günnur, and Nilgün Civaş. 2013. 'An overview of biofuels from energy crops: Current status and future prospects.' *Renewable and Sustainable Energy Reviews* 28:900–916.

Komis, George, Olga Šamajová, Miroslav Ovečka, and Jozef Šamaj. 2015. 'Super-resolution Microscopy in Plant Cell Imaging.' *Trends in Plant Science* 20, no. 12 (December): 834–843.

Kopsell, Dean A., Carl E. Sams, and Robert C. Morrow. 2015. 'Blue Wavelengths from LED Lighting Increase Nutritionally Important Metabolites in Specialty Crops.' *HortScience* 50, no. 9 (September): 1285–1288.

Krapf, Diego. 2015. 'Mechanisms Underlying Anomalous Diffusion in the Plasma Membrane.' In *Current Topics In Membranes*, 167–207.

Kundzewicz, Z. W., L. J. Mata, N. W. Arnell, et al. 2008. 'The implications of projected climate change for freshwater resources and their management.' *Hydrological Sciences Journal* 53, no. 1 (February): 3–10.

Lavoie-Cardinal, Flavie, Anthony Bilodeau, Mado Lemieux, et al. 2020. 'Neuronal activity remodels the F-actin based submembrane lattice in dendrites but not axons of hippocampal neurons.' *Scientific Reports* 10, no. 1 (December): 11960.

Le Cam, L. 1986. 'The central limit theorem around 1935.' *Statistical Science* 1 (1): 78–91.

Leddy, Holly A., and Farshid Guilak. 2003. 'Site-specific molecular diffusion in articular cartilage measured using fluorescence recovery after photobleaching.' *Annals of Biomedical Engineering* 31 (7): 753–760.

Lee, Amy Huei-Yi, Brenden Hurley, Corinna Felsensteiner, et al. 2012. 'A Bacterial Acetyltransferase Destroys Plant Microtubule Networks and Blocks Secretion.' Edited by Shengyang He. *PLoS Pathogens* 8, no. 2 (February): e1002523.

Lee, T.C., R.L. Kashyap, and C.N. Chu. 1994. 'Building Skeleton Models via 3-D Medial Surface Axis Thinning Algorithms.' *CVGIP: Graphical Models and Image Processing* 56, no. 6 (November): 462–478.

Léger, J. C. 1999. 'Menger curvature and rectifiability.' *Annals of Mathematics* 149 (3): 831–869.

Leontovyčová, Hana, Tetiana Kalachova, and Martin Janda. 2020. 'Disrupted actin: a novel player in pathogen attack sensing?' *New Phytologist* 227, no. 6 (September): 1605–1609.

Leontovyčová, Hana, Tetiana Kalachova, Lucie Trdá, et al. 2019. 'Actin depolymerization is able to increase plant resistance against pathogens via activation of salicylic acid signalling pathway.' *Scientific Reports* 9, no. 1 (December): 10397.

Li, Hongsheng, Tian Shen, Matthew B. Smith, et al. 2009a. 'Automated actin filament segmentation, tracking and tip elongation measurements based on open active contour models.' *Proceedings - 2009 IEEE International Symposium on Biomedical Imaging: From Nano to Macro, ISBI 2009,* 1302–1305.

Li, Hongsheng, Tian Shen, Dimitrios Vavylonis, and Xiaolei Huang. 2009b. 'Actin Filament Tracking Based on Particle Filters and Stretching Open Active Contour Models.' In *Medical Image Computing and Computer-Assisted Intervention – MICCAI 2009,* 673–681.

Li, Jian-Feng, Julie E Norville, John Aach, et al. 2013. 'Multiplex and homologous recombination–mediated genome editing in Arabidopsis and Nicotiana benthamiana using guide RNA and Cas9.' *Nature Biotechnology* 31, no. 8 (August): 688–691.

Li, Jiejie, Lingyan Cao, and Christopher J. Staiger. 2017. 'Capping Protein Modulates Actin Remodeling in Response to Reactive Oxygen Species during Plant Innate Immunity.' *Plant Physiology* 173, no. 2 (February): 1125–1136.

Li, Jiejie, Jessica L. Henty-Ridilla, Benjamin H. Staiger, Brad Day, and Christopher J. Staiger. 2015. 'Capping protein integrates multiple MAMP signalling pathways to modulate actin dynamics during plant innate immunity.' *Nature Communications* 6, no. 1 (November): 7206.

Li, Pai, and Brad Day. 2019. 'Battlefield cytoskeleton: Turning the tide on plant immunity.' *Molecular Plant-Microbe Interactions* 32 (1): 25–34.

Li, Shundai, Laurent Blanchoin, Zhenbiao Yang, and Elizabeth M. Lord. 2003. 'The Putative Arabidopsis Arp2/3 Complex Controls Leaf Cell Morphogenesis.' *Plant Physiology* 132, no. 4 (August): 2034–2044.

Liang, P., and T. H. MacRae. 1997. 'Molecular chaperones and the cytoskeleton.' *Journal of Cell Science* 110 (13): 1431–1440.

Lieber, Elinor. 1982. *Introduction to the history of plant pathology,* 26:221–221. 2. Cambridge University Press, April.

Lin, Congping, Peter Ashwin, and Gero Steinberg. 2021. 'Modelling the motion of organelles in an elongated cell via the coordination of heterogeneous drift–diffusion and long-range transport.' *The European Physical Journal E* 44, no. 2 (February): 10.

Lin, Congping, Martin Schuster, Sofia Cunha Guimaraes, et al. 2016. 'Active diffusion and microtubule-based transport oppose myosin forces to position organelles in cells.' *Nature Communications* 7, no. 1 (September): 11814.

Lin, Congping, Rhiannon R. White, Imogen Sparkes, and Peter Ashwin. 2017. 'Modeling Endoplasmic Reticulum Network Maintenance in a Plant Cell.' *Biophysical Journal* 113, no. 1 (July): 214–222.

Lipka, Volker, Jan Dittgen, Pawel Bednarek, et al. 2005. 'Pre- and Postinvasion Defenses Both Contribute to Nonhost Resistance in Arabidopsis.' *Science* 310, no. 5751 (November): 1180–1183.

Littlejohn, George R., Susan Breen, Nicholas Smirnoff, and Murray Grant. 2021. 'Chloroplast immunity illuminated.' *New Phytologist* 229, no. 6 (March): 3088–3107.

Llave, Cesar, Kristin D. Kasschau, Maggie A. Rector, and James C. Carrington. 2002. 'Endogenous and Silencing-Associated Small RNAs in Plants[W].' *The Plant Cell* 14, no. 7 (July): 1605–1619.

Long, Stephen P., Amy Marshall-Colon, and Xin-Guang Zhu. 2015. 'Meeting the Global Food Demand of the Future by Engineering Crop Photosynthesis and Yield Potential.' *Cell* 161, no. 1 (March): 56–66.

Lu, Yanhui, Kongming Wu, Yuying Jiang, et al. 2010. 'Mirid Bug Outbreaks in Multiple Crops Correlated with Wide-Scale Adoption of Bt Cotton in China.' *Science* 328, no. 5982 (May): 1151–1154.

Lucas, John A., Nichola J. Hawkins, and Bart A. Fraaije. 2015. 'The Evolution of Fungicide Resistance,' 29–92.

Ludbrook, John. 1998. 'MULTIPLE COMPARISON PROCEDURES UPDATED.' *Clinical and Experimental Pharmacology and Physiology* 25, no. 12 (December): 1032–1037.

Ma, Zhiming, Yanbiao Sun, Xinlu Zhu, et al. 2022. 'Membrane nanodomains modulate formin condensation for actin remodeling in Arabidopsis innate immune responses.' *Plant Cell* 34 (1): 374–394.

Malhotra, S. K. 2017. 'Horticultural crops and climate change: A review.' *Indian Journal of Agricultural Sciences* 87 (1): 12–22.

Martin, William, Tamas Rujan, Erik Richly, et al. 2002. 'Evolutionary analysis of Arabidopsis, cyanobacterial, and chloroplast genomes reveals plastid phylogeny and thousands of cyanobacterial genes in the nucleus.' *Proceedings of the National Academy of Sciences of the United States of America* 99 (19): 12246–12251.

Martins, Teresa, Matthew Evans, Hugh Woolfenden, and Richard Morris. 2013. 'Towards the Physics of Calcium Signalling in Plants.' *Plants* 2, no. 4 (September): 541–588.

Masuda, Tadayoshi, and Peter D. Goldsmith. 2009. 'World soybean production: Area harvested, yield, and long-term projections.' *International Food and Agribusiness Management Review* 12 (4): 143–162.

Matern, Andreas, Christoph Böttcher, Lennart Eschen-Lippold, et al. 2019. 'A substrate of the ABC transporter PEN3 stimulates bacterial flagellin (flg22)-induced callose deposition in Arabidopsis thaliana.' *Journal of Biological Chemistry* 294 (17): 6857–6870.

Mathur, Jaideep. 2005. 'The ARP2/3 complex: Giving plant cells a leading edge.' *BioEssays* 27 (4): 377–387.

Mathur, Jaideep, Neeta Mathur, Birgit Kernebeck, and Martin Hülskamp. 2003. 'Mutations in Actin-Related Proteins 2 and 3 Affect Cell Shape Development in Arabidopsis.' *The Plant Cell* 15, no. 7 (July): 1632–1645.

Matoušková, Jindřiška, Martin Janda, Radovan Fišer, et al. 2014. 'Changes in actin dynamics are involved in salicylic acid signaling pathway.' *Plant Science* 223 (June): 36–44.

McCurdy, David W., David R. Kovar, and Christopher J. Staiger. 2001. 'Actin and actin-binding proteins in higher plants.' *Protoplasma* 215 (1-4): 89–104.

Meisrimler, Claudia-Nicole, Claudia Allan, Sophie Eccersall, and Richard J Morris. 2021. 'Interior design: how plant pathogens optimize their living conditions.' *New Phytologist* 229, no. 5 (March): 2514–2524.

Mendenhall, William, Robert J. Beaver, and Barbara M. Beaver. 2003. *Introduction to Probability and Statistics.* Brooks/Cole, a division of Thomson Learning, Inc.

Méndez, Kelly Ávila, and Hernán Mauricio Romero. 2017. 'Plant responses to pathogen attack: Molecular basis of qualitative resistance.' *Revista Facultad Nacional de Agronomia Medellin* 70 (2): 8225–8235.

Meyer, Dorit, Simone Pajonk, Cristina Micali, Richard O'Connell, and Paul Schulze-Lefert. 2009. 'Extracellular transport and integration of plant secretory proteins into pathogen-induced cell wall compartments.' *The Plant Journal* 57, no. 6 (March): 986–999.

Meza, Francisco J., Daniel Silva, and Hernán Vigil. 2008. 'Climate change impacts on irrigated maize in Mediterranean climates: Evaluation of double cropping as an emerging adaptation alternative.' *Agricultural Systems* 98, no. 1 (July): 21–30.

Miklis, Marco, Chiara Consonni, Riyaz A. Bhat, et al. 2007. 'Barley MLO Modulates Actin-Dependent and Actin-Independent Antifungal Defense Pathways at the Cell Periphery.' *Plant Physiology* 144, no. 2 (June): 1132–1143.

Mimura, Masayasu, Hideo Sakaguchi, and Mitsugu Matsushita. 2000. 'Reaction–diffusion modelling of bacterial colony patterns.' *Physica A: Statistical Mechanics and its Applications* 282, nos. 1-2 (July): 283–303.

Morris, Richard J. 2018. *Mathematical Modelling in Plant Biology*. Springer.

Morris, Richard J., and Kirsten H. ten Tusscher. 2021. 'Quantitative plant biology—Old and new.' *Quantitative Plant Biology* 2 (May): e8.

Mostafalou, Sara, and Mohammad Abdollahi. 2013. 'Pesticides and human chronic diseases: Evidences, mechanisms, and perspectives.' *Toxicology and Applied Pharmacology* 268, no. 2 (April): 157–177.

Muhammad, S, and N a Amusa. 2005. 'The Important Food Crops and Medicinal Plants of North-western Nigeria.' *Research Journal of Agriculture and Biological Sciences* 1 (3): 254–260.

Nagawa, Shingo, Tongda Xu, Deshu Lin, et al. 2012. 'ROP GTPase-Dependent Actin Microfilaments Promote PIN1 Polarization by Localized Inhibition of Clathrin-Dependent Endocytosis.' Edited by Mark Estelle. *PLoS Biology* 10, no. 4 (April): e1001299.

Nanguneri, Siddharth, R. T. Pramod, Nadia Efimova, et al. 2019. 'Characterization of Nanoscale Organization of F-Actin in Morphologically Distinct Dendritic Spines In Vitro Using Supervised Learning.' *eneuro* 6, no. 4 (July): 0425–18.

Narita, Akihiro, Jan Mueller, Edit Urban, et al. 2012. 'Direct determination of actin polarity in the cell.' *Journal of Molecular Biology* 419 (5): 359–368.

Nédélec, F. J., T. Surrey, A. C. Maggs, and S. Leibler. 1997. 'Self-organization of microtubules and motors.' *Nature* 389 (6648): 305–308.

Neuhaus, Jean Marc, Michael Wanger, Thomas Keiser, and Albrecht Wegner. 1983. 'Treadmilling of actin.' *Journal of Muscle Research and Cell Motility* 4 (5): 507–527.

Ng, Marie, Tom Fleming, Margaret Robinson, et al. 2014. 'Global, regional, and national prevalence of overweight and obesity in children and adults during 1980–2013: a systematic analysis for the Global Burden of Disease Study 2013.' *The Lancet* 384, no. 9945 (August): 766–781.

Ngou, Bruno Pok Man, Hee Kyung Ahn, Pingtao Ding, and Jonathan D.G. Jones. 2021. 'Mutual potentiation of plant immunity by cell-surface and intracellular receptors.' *Nature* 592 (7852): 110–115.

Nick, Peter. 2020. 'The stable brother hiding in the shadow—news on intermediate filaments.' *Protoplasma* 257 (5): 1257–1258.

Nicolau, Dan V., John F. Hancock, and Kevin Burrage. 2007. 'Sources of Anomalous Diffusion on Cell Membranes: A Monte Carlo Study.' *Biophysical Journal* 92, no. 6 (March): 1975–1987.

Nishimura, Marc T., and Jeffery L. Dangl. 2010. 'Arabidopsis and the plant immune system.' *Plant Journal.*

Nowak, Jacqueline, Kristin Gennermann, Staffan Persson, and Zoran Nikoloski. 2020. 'CytoSeg 2.0: Automated extraction of actin filaments.' *Bioinformatics* 36 (9): 2950–2951.

Ostle, N.J., P.E. Levy, C.D. Evans, and P. Smith. 2009. 'UK land use and soil carbon sequestration.' *Land Use Policy* 26 (December): S274–S283.

Ouyang, Wei, Andrey Aristov, Mickaël Lelek, Xian Hao, and Christophe Zimmer. 2018. 'Deep learning massively accelerates super-resolution localization microscopy.' *Nature Biotechnology* 36, no. 5 (May): 460–468.

Özdemir, Bugra, Pouyan Asgharzadeh, Annette I. Birkhold, et al. 2018. 'Cytological analysis and structural quantification of FtsZ1-2 and FtsZ2-1 network characteristics in Physcomitrella patens.' *Scientific Reports* 8, no. 1 (December): 11165.

Özdemir, Bugra, and Ralf Reski. 2021. 'Automated and semi-automated enhancement, segmentation and tracing of cytoskeletal networks in microscopic images: A review.' *Computational and Structural Biotechnology Journal* 19:2106–2120.

Paez-Garcia, Ana, J. Alan Sparks, Louise de Bang, and Elison B. Blancaflor. 2018. 'Plant Actin Cytoskeleton: New Functions from Old Scaffold.' In *Concepts in Cell Biology - History and Evolution*, 103–137.

Pain, Charlotte, Verena Kriechbaumer, Maike Kittelmann, Chris Hawes, and Mark Fricker. 2019. 'Quantitative analysis of plant ER architecture and dynamics.' *Nature Communications* 10 (1): 1–15.

Paredez, Alexander R., Christopher R. Somerville, and David W. Ehrhardt. 2006. 'Visualization of Cellulose Synthase Demonstrates Functional Association with Microtubules.' *Science* 312, no. 5779 (June): 1491–1495.

Park, Doyoung. 2020. 'Quantification of Fibers through Automatic Fiber Reconstruction from 3D Fluorescence Confocal Images.' *Journal of Advanced Information Technology and Convergence* 10, no. 1 (July): 25–36.

Park, Wonkeun, Junjie Li, Rentao Song, Joachim Messing, and Xuemei Chen. 2002. 'CARPEL FACTORY, a Dicer Homolog, and HEN1, a Novel Protein, Act in microRNA Metabolism in Arabidopsis thaliana.' *Current Biology* 12, no. 17 (September): 1484–1495.

Parmesan, Camille, and G Yohe. 2003. 'A globally coherent fingerprint of climate change.' *Nature* 421:37–42.

Personnic, Nicolas, Kevin Bärlocher, Ivo Finsel, and Hubert Hilbi. 2016. 'Subversion of Retrograde Trafficking by Translocated Pathogen Effectors.' *Trends in Microbiology* 24, no. 6 (June): 450–462.

Pingali, Prabhu L, and Sumiter S Broca. 2014. 'Global Agricultural Performance : Past Trends and Future Prospects.' *World Bank, Washington DC.*

Pingali, Prabhu L. 2012. 'Green revolution: Impacts, limits, andthe path ahead.' *Proceedings of the National Academy of Sciences of the United States of America* 109 (31): 12302–12308.

Poletta, G.L., A. Larriera, E. Kleinsorge, and M.D. Mudry. 2009. 'Genotoxicity of the herbicide formulation Roundup® (glyphosate) in broad-snouted caiman (Caiman latirostris) evidenced by the Comet assay and the Micronucleus test.' *Mutation Research/Genetic Toxicology and Environmental Mutagenesis* 672, no. 2 (January): 95–102.

Pollard, Thomas D., and Gary G. Borisy. 2003. 'Cellular Motility Driven by Assembly and Disassembly of Actin Filaments.' *Cell* 112, no. 4 (February): 453–465.

Prahl, Louis S., Brian T. Castle, Melissa K. Gardner, and David J. Odde. 2014. 'Quantitative Analysis of Microtubule Self-assembly Kinetics and Tip Structure.' In *Methods in Enzymology*, 35–52.

Provart, Nicholas J., Jose Alonso, Sarah M. Assmann, et al. 2016. '50 years of Arabidopsis research: highlights and future directions.' *New Phytologist* 209, no. 3 (February): 921–944.

Pullen, Nick, and Richard J. Morris. 2014. 'Bayesian Model Comparison and Parameter Inference in Systems Biology Using Nested Sampling.' Edited by Simon Rogers. *PLoS ONE* 9, no. 2 (February): e88419.

Puwal, S., and B. J. Roth. 2007. 'Forward Euler stability of the bidomain model of cardiac tissue.' *IEEE Transactions on Biomedical Engineering.*

Qi, Junsheng, Jinlong Wang, Zhizhong Gong, and Jian Min Zhou. 2017. 'Apoplastic ROS signaling in plant immunity.' *Current Opinion in Plant Biology* 38:92–100.

Qin, Li, Lijiang Liu, Jiangying Tu, et al. 2021. 'The ARP2/3 complex, acting cooperatively with Class I formins, modulates penetration resistance in Arabidopsis against powdery mildew invasion.' *Plant Cell* 33 (9): 3151–3175.

Racine, Victor, MARTIN SACHSE, JEAN SALAMERO, et al. 2007. 'Visualization and quantification of vesicle trafficking on a three-dimensional cytoskeleton network in living cells.' *Journal of Microscopy* 225, no. 3 (March): 214–228.

Ramírez, C. A., M. Patel, and K. Blok. 2006. 'How much energy to process one pound of meat? A comparison of energy use and specific energy consumption in the meat industry of four European countries.' *Energy* 31 (12): 2047–2063.

Rapsomaniki, Maria Anna, Panagiotis Kotsantis, Ioanna-Eleni Symeonidou, et al. 2012. 'easyFRAP: an interactive, easy-to-use tool for qualitative and quantitative analysis of FRAP data.' *Bioinformatics* 28, no. 13 (July): 1800–1801.

Rasheed, Maria, Awais Muhammad, Khalid Mokaram, and Sohail Asad. 2022. 'The Role of Genetically-Modified (GM) Crops in Food Security.' *Life Science Journal.*

Ray, Deepak K., Nathaniel D. Mueller, Paul C. West, and Jonathan A. Foley. 2013. 'Yield Trends Are Insufficient to Double Global Crop Production by 2050.' *PLoS ONE* 8 (6).

Rayner, J. C.W., O. Thas, and D. J. Best. 2011. 'Smooth tests of goodness of fit.' *Wiley Interdisciplinary Reviews: Computational Statistics* 3 (5): 397–406.

Reinhart, Brenda J., Earl G. Weinstein, Matthew W. Rhoades, Bonnie Bartel, and David P. Bartel. 2002. 'MicroRNAs in plants.' *Genes & Development* 16, no. 13 (July): 1616–1626.

Research Institute (IFPRI), International Food Policy. 2016. *Global Nutrition Report 2016 From Promise to Impact Ending Malnutrition by 2030.* Technical report.

Reverey, Julia F., Jae-Hyung Jeon, Han Bao, et al. 2015. 'Superdiffusion dominates intracellular particle motion in the supercrowded cytoplasm of pathogenic Acanthamoeba castellanii.' *Scientific Reports* 5, no. 1 (December): 11690.

Rigort, Alexander, David Günther, Reiner Hegerl, et al. 2012. 'Automated segmentation of electron tomograms for a quantitative description of actin filament networks.' *Journal of Structural Biology* 177 (1): 135–144.

Robinson, G. H.J., J. Balk, and C. Domoney. 2019. 'Improving pulse crops as a source of protein, starch and micronutrients.' *Nutrition Bulletin* 44 (3): 202–215.

Rommens, Caius M. 2010. 'Barriers and paths to market for genetically engineered crops.' *Plant Biotechnology Journal* 8, no. 2 (February): 101–111.

Rosero, Amparo, Viktor Žárský, and Fatima Cvrčková. 2014. 'Visualizing and Quantifying the In Vivo Structure and Dynamics of the Arabidopsis Cortical Cytoskeleton Using CLSM and VAEM.' In *Plant Cell Morphogenesis*, 87–97.

Rottner, Klemens, Jan Faix, Sven Bogdan, Stefan Linder, and Eugen Kerkhoff. 2017. 'Actin assembly mechanisms at a glance.' *Journal of Cell Science* 130 (20): 3427–3435.

Rubiato, Hector M, Mengqi Liu, Richard J O'Connell, and Mads E Nielsen. 2022. 'Plant SYP12 syntaxins mediate an evolutionarily conserved general immunity to filamentous pathogens.' *eLife* 11 (February).

Ruhnow, Felix, David Zwicker, and Stefan Diez. 2011. 'Tracking single particles and elongated filaments with nanometer precision.' *Biophysical Journal* 100 (11): 2820–2828.

Sabelleck, Björn, and Ralph Panstruga. 2018. 'Novel jack-in-the-box effector of the barley powdery mildew pathogen?' *Journal of Experimental Botany* 69, no. 15 (June): 3511–3514.

Sambade, Adrian, Amitesh Pratap, Henrik Buschmann, Richard J. Morris, and Clive Lloyd. 2012. 'The Influence of Light on Microtubule Dynamics and Alignment in the Arabidopsis Hypocotyl.' *The Plant Cell* 24, no. 1 (February): 192–201.

Sampathkumar, Arun, Jelmer J. Lindeboom, Seth Debolt, et al. 2011. 'Live cell imaging reveals structural associations between the actin and microtubule cytoskeleton in arabidopsis.' *Plant Cell* 23 (6): 2302–2313.

Sancibrian, R., F. Viadero, P. Garcı a, and A. Fernández. 2004. 'Gradient-based optimization of path synthesis problems in planar mechanisms.' *Mechanism and Machine Theory* 39, no. 8 (August): 839–856.

Sandberg, Maria. 2021. 'Sufficiency transitions: A review of consumption changes for environmental sustainability.' *Journal of Cleaner Production* 293:126097.

Sang, Yuying, and Alberto P. Macho. 2017. 'Analysis of PAMP-Triggered ROS Burst in Plant Immunity.' In *Methods in Molecular Biology*, 143–153.

Sassmann, Stefan, Cecilia Rodrigues, Stephen W. Milne, et al. 2018. 'An Immune-Responsive Cytoskeletal-Plasma Membrane Feedback Loop in Plants.' *Current Biology*.

Saxton, M.J. 1997. 'Single-particle tracking: the distribution of diffusion coefficients.' *Biophysical Journal* 72, no. 4 (April): 1744–1753.

Saxton, Michael J., and Ken Jacobson. 1997. 'SINGLE-PARTICLE TRACKING:Applications to Membrane Dynamics.' *Annual Review of Biophysics and Biomolecular Structure* 26, no. 1 (June): 373–399.

Sazzed, Salim, Junha Song, Julio A. Kovacs, et al. 2018. 'Tracing actin filament bundles in three-dimensional electron tomography density maps of hair cell stereocilia.' *Molecules* 23 (4).

Schaff, James C., Ann E. Cowan, Leslie M. Loew, and Ion I. Moraru. 2009. 'Virtual FRAP - an Experiment-Oriented Simulation Tool.' *Biophysical Journal* 96, no. 3 (February): 30a.

Schaub, Sébastien, Jean Jacques Meister, and Alexander B. Verkhovsky. 2007. 'Analysis of actin filament network organization in lamellipodia by comparing experimental and simulated images.' *Journal of Cell Science* 120 (8): 1491–1500.

Schmidt, Anja, and Michael N. Hall. 1998. 'Signaling to the actin cytoskeleton.' *Annual Review of Cell and Developmental Biology* 14:305–338.

Schmidt, Sarah Maria, and Ralph Panstruga. 2007. 'Cytoskeleton functions in plant-microbe interactions.' *Physiological and Molecular Plant Pathology* 71 (4-6): 135–148.

Schütz, G.J., H. Schindler, and T. Schmidt. 1997. 'Single-molecule microscopy on model membranes reveals anomalous diffusion.' *Biophysical Journal* 73, no. 2 (August): 1073–1080.

Shen, Hao, Lawrence J. Tauzin, Rashad Baiyasi, et al. 2017. 'Single Particle Tracking: From Theory to Biophysical Applications.' *Chemical Reviews* 117, no. 11 (June): 7331–7376.

Shimada, Chiyumi, Volker Lipka, Richard O'Connell, et al. 2006. 'Nonhost resistance in Arabidospis-Colletotrichum interactions acts at the cell periphery and requires actin filament function.' *Molecular Plant-Microbe Interactions* 19 (3): 270–279.

Shimono, Masaki, Takumi Higaki, Hanae Kaku, et al. 2016. 'Quantitative Evaluation of Stomatal Cytoskeletal Patterns during the Activation of Immune Signaling in Arabidopsis thaliana.' Edited by Hua Lu. *PLoS ONE* 11, no. 7 (July): e0159291.

Singh, Rachana, Samiksha Singh, Parul Parihar, Vijay Pratap Singh, and Sheo Mohan Prasad. 2015. 'Retrograde signaling between plastid and nucleus: A review.' *Journal of Plant Physiology* 181 (June): 55–66.

Smertenko, Andrei P., Michael J. Deeks, and Patrick J. Hussey. 2010. 'Strategies of actin reorganisation in plant cells.' *Journal of Cell Science* 123, no. 17 (September): 3019–3028.

Smith, Matthew B., Hongsheng Li, Tian Shen, et al. 2010. 'Segmentation and tracking of cytoskeletal filaments using open active contours.' *Cytoskeleton* 67 (11): 693–705.

Somerville, Chris R. 2001. 'An Early Arabidopsis Demonstration. Resolving a Few Issues Concerning Photorespiration.' *Plant Physiology* 125, no. 1 (January): 20–24.

Soumpasis, D. M. 1983. 'Theoretical analysis of fluorescence photobleaching recovery experiments.' *Biophysical Journal* 41 (1): 95–97.

Spielman, David J., and Rajul Pandya-Lorch. 2010. *Proven successes in agricultural development:A technical compendium to Millions Fed.* International Food Policy Research Institute.

Springmann, Marco, Keith Wiebe, Daniel Mason-D'Croz, et al. 2018. 'Health and nutritional aspects of sustainable diet strategies and their association with environmental impacts: a global modelling analysis with country-level detail.' *The Lancet Planetary Health* 2 (10): e451–e461.

Stahle, Lars, and Svante Wold. 1989. 'Analysis of variance (ANOVA).' *Chemometrics and Intelligent Laboratory Systems* 6, no. 4 (November): 259–272.

Stein, M. 2006. 'Arabidopsis PEN3/PDR8, an ATP Binding Cassette Transporter, Contributes to Nonhost Resistance to Inappropriate Pathogens That Enter by Direct Penetration.' *The Plant Cell Online.*

Strack, Rita. 2018. 'Deep learning advances super-resolution imaging.' *Nature Methods* 15, no. 6 (June): 403–403.

Sumner, T., E. Shephard, and I. D. L. Bogle. 2012. 'A methodology for global-sensitivity analysis of time-dependent outputs in systems biology modelling.' *Journal of The Royal Society Interface* 9, no. 74 (September): 2156–2166.

Sun, He, Zhu Qiao, Khi Pin Chua, et al. 2018. 'Profilin Negatively Regulates Formin-Mediated Actin Assembly to Modulate PAMP-Triggered Plant Immunity.' *Current Biology* 28, no. 12 (June): 1882–1895.

Svitkina, Tatyana. 2018. 'The actin cytoskeleton and actin-based motility.' *Cold Spring Harbor Perspectives in Biology* 10 (1).

Tacon, Albert G.J., and Marc Metian. 2008. 'Global overview on the use of fish meal and fish oil in industrially compounded aquafeeds: Trends and future prospects.' *Aquaculture* 285 (1-4): 146–158.

Takemoto, Daigo, David A. Jones, and Adrienne R. Hardham. 2006. 'Re-organization of the cytoskeleton and endoplasmic reticulum in the Arabidopsis pen1-1 mutant inoculated with the non-adapted powdery mildew pathogen, Blumeria graminis f. sp. hordei.' *Molecular Plant Pathology* 7 (6): 553–563.

Tang, Jay X., and Paul A. Janmey. 1996. 'The polyelectrolyte nature of F-actin and the mechanism of actin bundle formation.' *Journal of Biological Chemistry* 271 (15): 8556–8563.

Tauger, Mark B. 2010. *Agriculture in World History.* Routledge, November.

Thomas, Clément. 2012. 'Bundling actin filaments from membranes: some novel players.' *Frontiers in Plant Science* 3 (August).

Tomkins, Melissa, Aoife Hughes, and Richard J Morris. 2021. 'An update on passive transport in and out of plant cells.' *Plant Physiology* 187, no. 4 (December): 1973–1984.

Tsugawa, Satoru, Nathan Hervieux, Oliver Hamant, et al. 2016. 'Extracting Subcellular Fibrillar Alignment with Error Estimation: Application to Microtubules.' *Biophysical Journal* 110, no. 8 (April): 1836–1844.

Tucker, Sara L, and Nicholas J Talbot. 2001. 'Surface Attachment and Pre-penetration Stage Development by Plant Pathogenic Fungi.' *Annual Reviews Phytopathology* 39:385–417.

Ulhaq, Anwaar, Naveed Akhtar, and Ganna Pogrebna. 2022. 'Efficient Diffusion Models for Vision: A Survey' (October).

Underwood, William, Andrew Ryan, and Shauna C. Somerville. 2017. 'An Arabidopsis Lipid Flippase Is Required for Timely Recruitment of Defenses to the Host–Pathogen Interface at the Plant Cell Surface.' *Molecular Plant.*

Van Norman, Jaimie M., and Philip N. Benfey. 2009. 'Arabidopsis thaliana as a model organism in systems biology.' *Wiley Interdisciplinary Reviews: Systems Biology and Medicine* 1 (3): 372–379.

Van Regenmortel, Marc H V. 2004. 'Reductionism and complexity in molecular biology. Scientists now have the tools to unravel biological and overcome the limitations of reductionism.' *EMBO reports* 5, no. 11 (November): 1016–20.

Vidali, Luis, Peter A.C. Van Gisbergen, Christophe Guérin, et al. 2009. 'Rapid formin-mediated actin-filament elongation is essential for polarized plant cell growth.' *Proceedings of the National Academy of Sciences of the United States of America* 106 (32): 13341–13346.

Vladar, Eszter K., Roy D. Bayly, Ashvin M. Sangoram, Matthew P. Scott, and Jeffrey D. Axelrod. 2012. 'Microtubules enable the planar cell polarity of airway cilia.' *Current Biology* 22 (23): 2203–2212.

Voigt, Christian A. 2014. 'Callose-mediated resistance to pathogenic intruders in plant defense-related papillae.' *Frontiers in Plant Science* 5 (APR): 1–6.

Vorosmarty, C. J., and D. Sahagian. 2000. 'Anthropogenic disturbance of the terrestrial water cycle.' *BioScience* 50 (9): 753–765.

Wade, Richard H. 2009. 'On and around microtubules: An overview.' *Molecular Biotechnology* 43 (2): 177–191.

Wang, Caixia, Mohamed El-Shetehy, M.B. Shine, et al. 2014. 'Free Radicals Mediate Systemic Acquired Resistance.' *Cell Reports* 7, no. 2 (April): 348–355.

Wang, Xuemin. 2004. 'Lipid signaling.' *Current Opinion in Plant Biology* 7, no. 3 (June): 329–336.

Weckwerth, Wolfram. 2003. 'Metabolomics in Systems Biology.' *Annual Review of Plant Biology* 54, no. 1 (June): 669–689.

Weichsel, Julian, Nikolas Herold, Maik J. Lehmann, Hans-Georg Kräusslich, and Ulrich S. Schwarz. 2010. 'A quantitative measure for alterations in the actin cytoskeleton investigated with automated high-throughput microscopy.' *Cytometry Part A* 77A, no. 1 (January): 52–63.

Wickstead, Bill, and Keith Gull. 2011. 'The evolution of the cytoskeleton.' *Journal of Cell Biology* 194 (4): 513–525.

Wijk, Klaas J. van, and Felix Kessler. 2017. 'Plastoglobuli: Plastid Microcompartments with Integrated Functions in Metabolism, Plastid Developmental Transitions, and Environmental Adaptation.' *Annual Review of Plant Biology* 68, no. 1 (April): 253–289.

Willett, Walter, Johan Rockström, Brent Loken, et al. 2019. 'Food in the Anthropocene: the EAT–Lancet Commission on healthy diets from sustainable food systems.' *The Lancet* 393, no. 10170 (February): 447–492.

Woodward, Andrew W., and Bonnie Bartel. 2018. 'Biology in bloom: A primer on the arabidopsis thaliana model system.' *Genetics* 208 (4): 1337–1349.

Woolfenden, Hugh C., Gildas Bourdais, Michaela Kopischke, et al. 2017. 'A computational approach for inferring the cell wall properties that govern guard cell dynamics.' *The Plant Journal* 92, no. 1 (October): 5–18.

Wu, En Shinn, Kenneth Jacobson, and Demetrios Papahadjopoulos. 1977. 'Lateral diffusion in phospholipid multibilayers measured by fluorescence recovery after photobleaching.' *Biochemistry* 16 (17): 3936–3941.

Xia, Shumin, Ying Bena Lim, Zhen Zhang, et al. 2019. 'Nanoscale Architecture of the Cortical Actin Cytoskeleton in Embryonic Stem Cells.' *Cell Reports* 28, no. 5 (July): 1251–1267.

Xu, Ting, Christos Langouras, Maral Adeli Koudehi, et al. 2019. 'Automated Tracking of Biopolymer Growth and Network Deformation with TSOAX.' *Scientific Reports* 9 (1): 1–13.

Xu, Ting, Hongsheng Li, Tian Shen, et al. 2011. 'Extraction and analysis of actin networks based on Open Active Contour models.' *Proceedings - International Symposium on Biomedical Imaging*, 1334–1340.

Xu, Ting, Dimitrios Vavylonis, Feng Ching Tsai, et al. 2015. 'SOAX: A software for quantification of 3D biopolymer networks.' *Scientific Reports* 5.

Yamaoka, Naoto, Isao Matsumoto, and Masamichi Nishiguchi. 2006. 'The role of primary germ tubes (PGT) in the life cycle of Blumeria graminis: The stopping of PGT elongation is necessary for the triggering of appressorial germ tube (AGT) emergence.' *Physiological and Molecular Plant Pathology* 69, nos. 4-6 (October): 153–159.

Yin, Xinyou, and Paul C. Struik. 2010. 'Modelling the crop: from system dynamics to systems biology.' *Journal of Experimental Botany* 61, no. 8 (May): 2171–2183.

Yun, Byung-Wook, Helen A. Atkinson, Charlotte Gaborit, et al. 2003. 'Loss of actin cytoskeletal function and EDS1 activity, in combination, severely compromises non-host resistance in Arabidopsis against wheat powdery mildew.' *The Plant Journal* 34, no. 6 (June): 768–777.

Yun, Hye Sup, Woo Jun Sul, Hoo Sun Chung, Jae Hoon Lee, and Chian Kwon. 2022. 'Secretory membrane traffic in plant–microbe interactions.' *New Phytologist.*

Zandalinas, Sara I., Ron Mittler, Damián Balfagón, Vicent Arbona, and Aurelio Gómez-Cadenas. 2018. 'Plant adaptations to the combination of drought and high temperatures.' *Physiologia Plantarum* 162 (1): 2–12.

Zhang, Buyue, and Jan P. Allebach. 2007. 'Adaptive bilateral filter for sharpness enhancement and noise removal.' *Proceedings - International Conference on Image Processing, ICIP* 4 (5): 664–678.

Zhang, Meixiang, Yi Hsuan Chiang, Tania Y Toruño, et al. 2018. 'The MAP4 Kinase SIK1 Ensures Robust Extracellular ROS Burst and Antibacterial Immunity in Plants.' *Cell Host and Microbe* 24, no. 3 (September): 379–391.

Zhang, Zhen, Yukako Nishimura, and Pakorn Kanchanawong. 2017. 'Extracting microtubule networks from superresolution single-molecule localization microscopy data.' *Molecular Biology of the Cell* 28 (2): 333–345.